

University of Dayton

eCommons

Graduate Theses and Dissertations

Theses and Dissertations

2009

A non catalytic process for the production of nested bulk carbon nanotubes and nanotube arrays and their electrochemical behavior

Bill L. Riehl

University of Dayton

Follow this and additional works at: https://ecommons.udayton.edu/graduate_theses

Recommended Citation

Riehl, Bill L., "A non catalytic process for the production of nested bulk carbon nanotubes and nanotube arrays and their electrochemical behavior" (2009). *Graduate Theses and Dissertations*. 5175.

https://ecommons.udayton.edu/graduate_theses/5175

This Dissertation is brought to you for free and open access by the Theses and Dissertations at eCommons. It has been accepted for inclusion in Graduate Theses and Dissertations by an authorized administrator of eCommons. For more information, please contact mschlange1@udayton.edu, ecommons@udayton.edu.

A NON CATALYTIC PROCESS FOR THE PRODUCTION OF NESTED
BULK CARBON NANOTUBES AND NANOTUBE ARRAYS AND THEIR
ELECTROCHEMICAL BEHAVIOR

Dissertation

Submitted to

The School of Engineering

UNIVERSITY OF DAYTON

In Partial Fulfillment of the Requirements for

The Degree

Doctor of Philosophy in Materials Engineering

By

Bill L. Riehl, P.E.

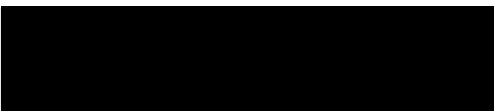
UNIVERSITY OF DAYTON

Dayton, Ohio


December 2009

A NON CATALYTIC PROCESS FOR THE PRODUCTION OF NESTED
BULK CARBON NANOTUBES AND NANOTUBE ARRAYS AND THEIR
ELECTROCHEMICAL BEHAVIOR

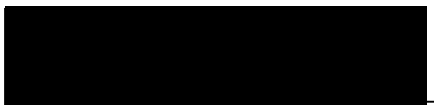
APPROVED BY:



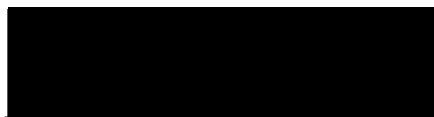
Jay M. Johnson, Ph.D.
Committee Chairman
Associate Professor,
Chemical & Materials Engineering




Elmo A. Blubaugh, Ph.D.
Committee Member
Technical Advisor



Douglas C. Hansen, Ph.D.
Committee Member
Associate Professor,
Materials Engineering




Muhammad Islam, Ph.D.
Committee Member
Professor, Mathematics




Daniel Eylon, D.Sc.
Professor and Director,
Materials Engineering

*Please ^{HFG-} Do not
Remove this note!*

Original



Malcolm W. Daniels, Ph.D.
Associate Dean
School of Engineering



Tony E. Saliba, Ph.D.
Dean, School of Engineering

ABSTRACT

A NON CATALYTIC PROCESS FOR THE PRODUCTION OF NESTED BULK CARBON NANOTUBES AND NANOTUBE ARRAYS AND THEIR ELECTROCHEMICAL BEHAVIOR

Name: Riehl, Bill Logan
University of Dayton

Advisor: Dr. Jay M. Johnson

To date, no one has devised a scalable process for the production of electrochemically clean carbon nanotubes. The application of carbon nanotubes has been limited by three factors: cost, consistency, and purity. Nearly all carbon nanotube processes fall under the chemical vapor deposition method. This results in inconsistencies in diameter and length, as well as residual metal contamination. Residual metal contamination is perhaps the greatest impediment of carbon nanotube use for electrochemical applications. The goal of this effort is to develop and demonstrate a process for the production of electrochemically clean carbon nanotube materials suitable for applications such as chemical/biological sensors, batteries/fuel cells, and electrochemical double layer capacitors. To ensure no metal contamination is present in the "as produced" material, a process was developed that uses the carbo-thermal decomposition of the transition metal and metalloid carbides that is applicable to CNT arrays and production of bulk CNT materials. A substrate attached carbon nanotube modified electrode is demonstrated.

ACKNOWLEDGEMENTS

I would like to thank Dr. Bonnie Riehl for her support for without her, this work and my education would not have been possible. Dr. Jay Johnson, you have been a friend as well as a mentor. A student could not have asked for a better environment to learn in. I would also like to acknowledge Dennis Helmig for his guidance and influence professionally, as well as Dr. Elmo Blubaugh for his many insightful discussions on this topic as well as many others. The many discussions with Dr. Craig Banks were also instrumental in developing my understanding of carbon electrochemistry in general. Dr. John Boeckl provided valuable and timely insight into the microscopy of the material, and to him I am thankful.

I must acknowledge my committee members for their patience and flexibility in the many turns this work has taken.

Finally, all research described within this work was solely supported by Riehl Engineering, Ltd. Riehl Engineering solely owns the technology and intellectual property developed and described herein.

TABLE OF CONTENTS

ABSTRACT.....	iii
ACKNOWLEDGMENTS.....	iv
LIST OF ILLUSTRATIONS.....	viii
LIST OF TABLES.....	xv
INTRODUCTION.....	1
CHAPTER	
1. CARBO-THERMAL CARBIDE CONVERSION.....	7
1.1 Introduction.....	7
1.2 Process Introduction.....	9
1.2.1 Alumina Tube Reactor.....	9
1.2.2 Graphite Hot Zone Reactor.....	10
1.2.3 Process Overview.....	12
1.2.4 Reactive Gases.....	15
1.2.5 Examples.....	18
1.2.5.1 Example 1. SCNR Whiskers.....	19
1.2.5.2 Example 2. Planar Aligned Array.....	25
1.2.5.3 Example 3. Non-Planar SCNR Array, Open Cell Foam.....	28

1.2.5.4 Example 4. SiC Coated Carbon Fibers..	31
1.2.5.5 Example 5. Large Production SCNR	
Nanoclusters	32
1.2.6 Alternate Carbide Examples.....	36
1.2.6.1 Example 6. Al ₄ C ₃ Starting Material.....	37
1.2.6.2 Example 7. B ₄ C Starting Material.....	38
1.2.6.3 Example 8. TiC Starting Material.....	38
1.2.6.4 Example 9. ZrC Starting Material.....	39
1.3 Verification of Silicon Carbide Chemistry.....	40
1.4 Conclusions.....	46
2. CHARACTERIZATION OF CATALYST FREE CARBON	
NANOMATERIALS.....	47
2.1 Introduction.....	47
2.2 Purity Characterization.....	48
2.3 Raman Spectroscopy.....	51
2.4 Electron Microscopy.....	66
2.5 Conclusions.....	73
3. ELECTROCHEMICAL BEHAVIOR.....	74
3.1 Introduction.....	74
3.2 Experimental Setup.....	77
3.2.1 Instrumentation.....	77
3.2.1.1 Carbon Paste and Open Cell Foam.....	77
3.2.1.2 Immobilized Nanomaterial.....	77

3.2.2 Chemicals Used.....	78
3.3 Electrode Overview.....	79
3.3.1 Carbon Paste Electrodes.....	79
3.3.2 Immobilized Nanomaterial Electrodes.....	81
3.3.3 Open Cell Foam Electrodes.....	81
3.4 Electrochemical Behavior.....	85
3.4.1 Paste Electrode Behavior.....	85
3.4.2 Immobilized Nanomaterial Behavior.....	95
3.4.3 SCNR Modified Open Cell Foam Electrode Behavior.....	99
3.5 Conclusions.....	111
4. SUMMARY AND CONCLUSIONS.....	112
4.1 Summary.....	112
4.2 Conclusions.....	113
APPENDIX.....	117
BIBLIOGRAPHY.....	149

LIST OF ILLUSTRATIONS

1. Figure 1.1. Graphite Hot Zone Reactor for Batch Processing.....	11
2. Figure 1.2. Time-Temperature-Pressure Profile of SCNR Whisker Production.....	21
3. Figure 1.3. Low Magnification HRTEM Image of SCNR Whiskers.....	23
4. Figure 1.4. High Magnification HRTEM of SCNR Whiskers.....	24
5. Figure 1.5. HRTEM Image of Aligned Array.....	27
6. Figure 1.6. SEM of ERG Aerospace Duo Cell SiC Foam.....	29
7. Figure 1.7. SEM of Non Planar SCNR Array.....	30
8. Figure 1.8. HRTEM of SCNR Coated Filament.....	32
9. Figure 1.9. High Temperature Reactor with Retort.....	34
10. Figure 1.10. HRTEM of SCNR Nanoclusters at 25K Magnification	35
11. Figure 1.11. HRTEM of SCNR Nanoclusters at 50K Magnification.....	36
12. Figure 1.12. Post Production Picture of Reactor Showing SiO/SiO ₂ Deposits.....	41

13. Figure 1.13. Picture Showing SiO/SiO ₂ Deposits.....	42
14. Figure 1.14. Cold Finger Design for Collection of SiO/SiO ₂	43
15. Figure 2.1. EDS of SCNR Nanoclusters.....	50
16. Figure 2.2. Raman Spectrum of Alfa Aesar MWCNTs using a 514nm Excitation Laser.....	54
17. Figure 2.3. Raman Spectrum of NanoLab MWCNTs using a 514nm Excitation Laser.....	55
18. Figure 2.4. Raman Spectrum of Alfa Aesar MWCNTs using a 785nm Excitation Laser.....	56
19. Figure 2.5. Raman Spectrum of NanoLab MWCNTs using a 785nm Excitation Laser.....	57
20. Figure 2.6. Raman Spectrum of SCNR Nanoclusters using a 514nm Excitation Laser.....	58
21. Figure 2.7. Raman Spectrum of SCNR Whiskers using a 514nm Excitation Laser.....	59
22. Figure 2.8. Raman Spectrum of SCNR Nanoclusters using a 785nm Excitation Laser.....	60
23. Figure 2.9. Raman Spectrum of SCNR Whiskers using a 785nm Excitation Laser.....	61
24. Figure 2.10. RBM Vibrations of SCNR Whiskers.....	63
25. Figure 2.11. RBM Vibrations of SCNR Nanoclusters.....	64
26. Figure 2.12. SEM Image of Bulk SCNR Nanoclusters.....	68

27. Figure 2.13. Medium Magnification HRTEM Image of Bulk SCNR Nanoclusters.....	69
28. Figure 2.14. High Magnification HRTEM Image of Single SCNR Nanocluster.....	70
29. Figure 2.15. High Magnification HRTEM Image of Single SCNR Nanocluster.....	71
30. Figure 3.1. SCNR Modified Open Cell Foam Electrode.....	84
31. Figure 3.2. Background CV Scans on Various Carbon Paste Electrode Materials.....	86
32. Figure 3.3. Background Current Comparison of Paste Electrodes Using Expanded Scale.....	87
33. Figure 3.4. Background CVs of BAS Carbon Paste Electrode.....	88
34. Figure 3.5. Background CVs of MWCNT Paste Electrode.....	89
35. Figure 3.6. Background CVs of SCNR Paste Electrode.....	90
36. Figure 3.7. Cyclic Voltamograms of 1mM Ferricyanide at Carbon Paste Electrode.....	91
37. Figure 3.8. Cyclic Voltamograms of 1mM Ferricyanide at MWCNT Paste Electrode.....	92
38. Figure 3.9. Cyclic Voltamograms of 1mM Ferricyanide at SCNR Paste Electrode.....	93

39. Figure 3.10. Peak Separation of Nanostructured Paste	
Electrodes.....	94
40. Figure 3.11. Cyclic Voltamogram of MWCNTs (A) and SCNR	
Nanoclusters (B) in the Presence of 1mM Hydrazine, Second	
Scan Shown.....	95
41. Figure 3.12. Cyclic Voltamograms of Ferricyanide on an	
Electrode Fabricated with Increasing SCNR Loading at 10mV/s	
Scan Rate.....	97
42. Figure 3.13. Cyclic Voltamograms of Ferricyanide on Electrodes	
Fabricated with Different Lots of SCNR Clusters at 10mV/s Scan	
Rate	98
43. Figure 3.14. Background CV of SCNR Modified Open Cell Foam	
Electrode.....	100
44. Figure 3.15. CVs of Ferricyanide on SCNR Modified Open Cell	
Foam Electrode with Varying Scan Rates.....	101
45. Figure 3.16. Plot of Peak Current vs. \log_{10} of Scan Rate.....	102
46. Figure 3.17. Cyclic Voltamogram of Ferricyanide on SCNR	
Modified Open Cell Foam Electrode, 5mV/s Scan Rate.....	103
47. Figure 3.18. Plot Peak Separation vs. \log_{10} of Scan	
Rate.....	104
48. Figure 3.19. Model Electrical Circuit of Open Cell Foam	
Electrode.....	105
49. Figure 3.20. IR Compensated CVs of Open Cell Foam	

Electrode.....	106
50. Figure 3.21. Comparison of IR Compensated and Uncompensated CVs of Open Cell Foam Electrode.....	107
51. Figure 3.22. Plot of Peak Separation vs. \log_{10} of Scan Rate of IR Corrected Electrode.....	108
52. Figure 3.23. Charge – Time Plots of Open Cell Foam Electrode..	109
53. Figure 3.24. Anson Plot for 30s Step Time for Open Cell Foam Electrode.....	110
54. Figure A.1. Plan View of Vertically Aligned CNT Array from Single Crystal SiC.....	117
55. Figure A.2. Low Magnification HRTEM Image of SCNR Layer Grown From ERG Aerospace Open Cell Foam.....	118
56. Figure A.3. SEM Image of SCS-6 SiC Coated Carbon Fiber Pre Processing.....	119
57. Figure A.4. SEM Images of Foam Pre and Post CTCC Processing.....	120
58. Figure A.5. Increasing Magnification HRTEM Images of SCNR Modified Open Cell Foam.....	121
59. Figure A.6. HRTEM Image of Nanoclusters.....	122
60. Figure A.7. Chronoamperometry of SCNR Modified Open Cell Foam Electrode, 30s Step.....	123
61. Figure A.8. Charge – Time Plots of SCNR Modified Open Cell Foam Electrode.....	124

62. Figure A.9. Anson Plot of 5s Step from Figure A.8.....	125
63. Figure A.10. Anson Plot of 10s Step from Figure A.8.....	126
64. Figure A.11. Cyclic Voltamograms of 4mM Ferricyanide in 1M KNO ₃ at SCNR Paste Electrode.....	127
65. Figure A.12. Cyclic Voltamograms of 4mM Ferricyanide in 1M KNO ₃ at SCNR Paste Electrode.....	128
66. Figure A.13. Cyclic Voltamograms of 4mM Ferricyanide in 1M KNO ₃ at SCNR Paste Electrode.....	129
67. Figure A.14. Electrochemical Performance Comparison of SCNR Paste Electrodes Fabricated from Different Lots of SCNRs Using Cyclic Voltammetry in 4mM Ferricyanide.....	130
68. Figure A.15. SCNR Modified HOPG Electrode Cyclic Voltamograms in 4mM Ferricyanide.....	131
69. Figure A.16. SCNR Modified HOPG Electrode Cyclic Voltamograms in 4mM Ferricyanide.....	132
70. Figure A.17. SCNR Modified HOPG Electrode Cyclic Voltamograms in 4mM Ferricyanide.....	133
71. Figure A.18. Plot of Peak Currents of Modified HOPG Electrodes vs. Square Root of Scan Rate.....	134
72. Figure A.19. Cyclic Voltamograms of Multiple Open Cell Foam Electrodes in 4mM Ferricyanide at 100mV/s Scan Rate.....	135
73. Figure A.20. Cyclic Voltamograms of Open Cell Foam Electrode in 4mM Ferricyanide/1M KNO ₃ at Various Scan Rates.....	136

74. Figure A.21. Cyclic Voltamograms of Open Cell Foam Electrode in 4mM Ferricyanide/1M KNO ₃ at Various Scan Rates.....	137
75. Figure A.22. Cyclic Voltamograms of Open Cell Foam Electrode in 4mM Ferricyanide/1M KNO ₃ at Various Scan Rates.....	138
76. Figure A.23. IR Corrected and Normalized CVs of Open Cell Foam Electrodes in 4mM Ferricyanide and 1M KNO ₃	139
77. Figure A.24. Raman Spectrum of SCNRs from Aluminum Carbide Powder Using a 785nm Excitation Source.....	140
78. Figure A.25. Raman Spectrum of SCNRs from Boron Carbide Powder Using a 785nm Excitation Source.....	141
79. Figure A.26. Raman Spectrum of SCNRs from Zirconium Carbide Powder Using a 785nm Excitation Source.....	142
80. Figure A.27. Raman Spectrum of SCNRs from Titanium Carbide Using a 785nm Excitation Source.....	143
81. Figure A.28. Raman Spectrum of SCNR Whiskers Using a 785nm Excitation Source	144
82. Figure A.29. RBM Spectrum of SCNR Whisker Material Using a 785nm Excitation Source.....	145
83. Figure A.30. Raman Spectrum of SCNR Whisker Material Showing G Band Splitting.....	146
84. Figure A.31. Raman Spectrum of SCNR Coated Open Cell Foam Using 514nm Excitation Source.....	147

LIST OF TABLES

1. Table 1.1. Mass Balance of CTCC Conversion of SiC Nanopowder.....	43
2. Table 2.1. Elemental Analysis of CTCC Produced Materials via ICP-MS.....	49
3. Table 2.2. Typical CNT and SCNR Raman Spectral Features.....	65
4. Table A.1. Review of Process Variations Investigated.....	148

INTRODUCTION

The major objective of this work is to design and demonstrate a scalable and economical process for the production of fullerenes from metal and metalloid carbides. A further objective of this work is to produce fullerenes that display a high degree of graphitic edge plane character and no residual metal catalyst contamination. The final objective of this work is to develop a process to completely convert carbides into bulk fullerenes.

The materials produced by the process described herein are for use in electrochemical electrode fabrication. In the family of fullerenes, carbon nanotubes represent several key properties that make them well suited for electrochemical application. These properties include high edge plane character, large potential window, and high stability (1). However, most carbon nanotubes produced for commercial sale are synthesized using nanoparticles of transition metals as catalysts. Residual catalysts are detrimental to the electrochemical use of the material due to higher background currents, transient electrode behavior, and potentially misleading activity with certain analytes (2).

Carbon nanotubes have been the focus of frenzied research and development since 1991 when Single Walled Carbon NanoTubes (SWCNTs) were arguably discovered by Sumio Iijima of the Japanese firm NEC (3). A similar discovery was reported by IBM scientists in the same year (4). Further

claim to their discovery is made by Howard Tennant of Hyperion Catalysis in his patent (5). In fact, one reference cites an example of possible bamboo structured carbon nanotubes detected *via* X-ray diffraction as early as 1958 (6). Discovery aside, carbon nanotubes belong to a large class of crystalline carbon allotropes including nano-onions, horns, tubes, rods, wires, and dots; all commonly referred to as fullerenes. Carbon nanotubes are currently thought of as long, seamlessly wrapped graphene sheets with an aspect ratio of 1000:1 or greater, giving rise to their classification as one dimensional carbon nanomaterials. From an electrochemical perspective, CNTs have two regions which exhibit separate sets of properties: the end cap, which is related to edge plane graphite; and the sidewall, which is likened to basal plane graphite (7). Of particular interest is the chemical activity of CNTs, a result of the curvature of the graphene sheet(s) (8). In his work, Niyogi explains that smaller diameter tubes have greater reactivity due to pyramidization angles and π bond separation (9).

There are multiple techniques for the synthesis of CNTs. Briefly, there are 3 main methods: arc discharge, laser ablation, and Chemical Vapor Deposition (CVD). CVD is the most prevalent technique. A more recent, though lesser employed technique, is flame synthesis (10). The actual synthesis or formation process of CNTs is still hotly debated, regardless of process. *In-situ* transmission electron microscopy studies of catalytically grown CVD produced materials have suggested a two step formation process. Initially, a meta stable carbide is formed at the catalyst surface, resulting in the formation of an amorphous carbon rod. This is followed by graphitization of the carbon rod, then finally, termination of

growth (11). Arc discharge is the process most commonly associated with Single Wall Carbon Nanotubes (SWCNTs). It has been found that control over diameter and chirality may be obtained by manipulation of catalyst geometry and composition, as well as process gas composition and pressures (12). Arc discharge has the disadvantage of being a low quantity production process with high operating costs due to large electrical energy consumption. Yields are typically low, with high degrees of non- carbon nanotube structures present, necessitating further purification beyond catalyst removal. Laser ablation is the third most commonly used technique. This technique was initially reported by Rice University in 1995 (13). Similar to arc discharge, an inert gas, typically helium or argon is used to maintain a controlled pressure. As in arc discharge, a high temperature plasma is formed in the plume containing excited carbon atoms and molecules. Upon cooling, this plume forms a distribution of various fullerenes.

All of the processes discussed are significantly limited for electrochemical application by catalyst contamination, variations in fullerene structures formed, and amorphous carbon contamination. Catalyst contamination results in poor electrochemical performance, as mentioned above. The presence of various fullerene structures can result in inconsistent and unpredictable performance and amorphous carbon can shield / passify the active electrode area. To address these shortcomings, a non-catalytic process is needed where greater control over the consistency of product is realized.

Until 1997, when Kusunoki first published the formation of CNTs from silicon carbide sublimation, all processes used some form of transition metal catalyst for CNT formation (14). In this work, Kusunoki reports the formation of CNTs predominately on the silicon face of single crystal silicon carbide wafers. This however, has significant limitations. Single crystal SiC is very expensive, hindering the potential economy of use. The growth process results in a dense forest of aligned CNTs, but there is no mention of the possibility of bulk production of CNTs. Additionally, no mention is made of the possibility of the use of alternative carbides, or the use of polycrystalline carbides, or non-planar geometries.

Therefore, a focus of this effort is to develop a process for the production of bulk CNT materials through the complete conversion of a wide range of metal and metalloid carbides and investigate their electrochemical behavior. It should also be noted that thermal decomposition of silicon carbide to produce carbon allotropes such as graphite or graphene structures has been known for some time (15).

Because the process does not rely on the use of metal catalysts, Carbon Nanotubes (CNTs), and their derivatives, Solid Carbon Nanorods (SCNRs) produced via *Carbo-Thermal Carbide Conversion* (CTCC) do not display the traditional hollow core present in catalytically grown materials. Catalyst size and shape have been linked to CNT geometry previously (16). To differentiate between CVD grown CNTs with hollow cores and CTCC grown CNTs, CTCC grown materials are referred to as Solid Carbon Nanorods (SCNRs). SCNRs are

similar in outward appearance, physical properties, and chemical properties to carbon nanotubes, but have a solid core structure. That is, rather than the hollow core, SCNRs have a solid structure with concentric spacing on the order of interplanar spacing of graphite, approximately 0.4 nm. SCNRs can be considered a subclass of multiwalled carbon nanotubes (MWCNTs). When there is just a single wall; SCNRs are the smallest diameter (about 0.4 nm) SWCNTs that have been reported (17). The relative amounts of single walled SCNRs versus multiwalled SCNRs within a given SCNR assemblage fabricated by the CTCC process can be controlled primarily by adjusting process related parameters including temperature and reactive gas partial pressures.

Particular embodiments of the process enabled higher volume production with higher yields and a more homogeneous SCNR product. This is enabled through more defined control of the reactor conditions, kinetics, and thermodynamics (through selection of the reactants) of the chemical process involved. The electrochemical behavior of the SCNRs was characterized *via* cyclic voltammetry to show novel electrochemical properties including: reduced background current, stability, high electrochemically active surface area, thin layer behavior, and good electron transfer kinetics.

This work is divided into three chapters: a description of the process with examples; characterization of the material as produced; and electrochemical behavior of the material. Examples of the process include various novel geometries, polycrystalline starting materials, and non-silicon carbides. High Resolution Transmission Electron Microscopy (HRTEM) and Raman

spectroscopy were used to verify the structure of the materials produced and novelty of the structures formed which have not been reported previously in the literature. The unique electrochemical behavior of the material was then characterized via classical electrochemical techniques.

CHAPTER 1.

CARBO-THERMAL CARBIDE CONVERSION

1.1 Introduction

The impetus of this work was to develop a process for the production of fullerenes from carbides for electrochemical use. While sublimation of silicon carbide has been reported previously in the literature, this process does not adequately explain the degradation of the carbide to form aligned carbon nanotube arrays. The degradation of silicon carbide does provide an ideal synthesis route for the production of fullerenes. Silicon carbide is low cost and readily available. Most importantly, it contains no electrochemically active components. Detailed review of the silicon carbide sublimation process led to the formation of the hypothesis that the degradation process is not a physical one, rather a chemical reaction where silicon is reduced and carbon oxidized. It was further hypothesized that the degradation process is applicable to other carbides.

The process developed in this work is unique in that no transition metal catalyst is used to form the nanostructure. Carbo-Thermal Carbide Conversion (CTCC) is a chemical process for producing carbon nanostructures on and from solid phase carbide source materials for electronic, electrochemical, chemical and

mechanical applications. This has a plurality of advantages over the more common CVD process. In CVD production of carbon nanotubes, wide variations in material size, shape, and chirality result. This is most typically seen via HRTEM and Raman spectroscopy (18). Perhaps most limiting is the irreversible incorporation of metal contaminants into the material produced (2).

The methodology used to test the general hypothesis (high temperature silicon carbide degradation is a chemical process in nature) was to determine the effects of various environments on the high temperature degradation of multiple carbides, followed by characterization *via* Raman spectroscopy and HRTEM. Fullerenes produced using silicon carbide were then characterized with classical electrochemical techniques and compared with contemporary carbon electrode materials. This work focused on the use of non-planar polycrystalline silicon carbide for the production of bulk carbon nanotube and nanotube derivatives for use in electrochemical applications. Two reactor designs were evaluated and tested: a high vacuum horizontal alumina tube furnace, and a resistively heated graphite hot-zone furnace optimized for production of nanostructures using the CTCC process. The process described below was used to produce materials with very high edge plane character evident by their Raman spectroscopy and fast electron transfer rates. This work was for the specific purpose of advancing the state of the art in carbon nanotube based electrode materials.

1.2 Process Introduction

Kusunoki *et. al*, described the influence of crystal structure and orientation on the growth mechanism under deep vacuum (19). They suggest, using growth rate comparisons, that the process favors initiation on the silicon face of SiC crystals where growth is normal to the planes of Si or C, not orthogonal. This empirically supports the conclusion that chemical reaction of silicon with a vapor phase reactant and subsequent removal *via* diffusion is the correct hypothesis.

1.2.1 Alumina Tube Reactor

During review of the work reported by Kusunoki, it was hypothesized that a reduction-oxidation chemical reaction was underway at the carbide surface, not the physical process proposed. To test this, a conventional horizontal alumina tube furnace was purchased for research into the possible chemistries. Alumina of 99.5% purity is generally considered very chemically inert and stable even at temperatures approaching 1700°C. A standard horizontal tube furnace was purchased from SentroTech (Cleveland, OH) with a 18in long hot zone capable of handling a 3in diameter refractory tube (STT-1700-3.0-18), with an appropriate 99.5% pure alumina tube (STTM-2750). The furnace was assembled with the supplied vacuum hardware as directed by the manufacturer.

It was found empirically that the alumina tubes were reactive, providing an oxidizing atmosphere which interfered with the CTCC process unless a strong reducing environment was created. This was done with the addition of a suitable gas phase such as carbon monoxide. The use of a reducing environment presented a significant process limitation due to degradation of the alumina tube. The use of carbon monoxide as a reactive gas lead to failure of the reactor tube, through conversion of the oxide to carbide. Conversion subsequently resulted in fractures in the tube, and failure to maintain a controllable environment. The use of an alumina tube furnace required one process deviation from the procedure used with the graphite hot zone reactor: ramp rates and cool down rates were altered to 3°C/min rather than the 60°C/min used with the graphite furnace. This was done to avoid internal stress which could fracture the alumina tube. The system was advertised to be capable of 10^{-6} Torr, though only 10^{-5} Torr was ultimately reached. The use of the alumina tube furnace was abandoned after learning of the hindering side reactions present with its use.

1.2.2 Graphite Hot Zone Reactor

With the experience gained from the alumina furnace experiments, a reactor with a more beneficial environment and process capability was designed. Because a reducing environment was hypothesized to be necessary for carbide conversion, an all graphite hot zone reactor was designed and built. In addition to

the better environmental conditions, the graphite hot zone enabled much faster temperature ramp times, up to 80°C/min.

The reactor consisted of a 304 stainless steel pressure vessel of 0.25in thickness, TIG welded continuously along all seams. A hinged stainless steel door was attached using a simple hinge system. The pressure vessel was designed for an operating pressure range of 10^{-6} Torr to 125psig. A 14in by 14in by 14in all graphite hot zone was constructed from carbon insulation from Carbon Composites, Inc (Leominster, MA), which acted as the reactor volume. The insulation was comprised of two components: graphite foil and rigidized carbon fiber. Meandering path graphite resistance elements were fabricated from 0.125in thick isomolded super fine graphite plates from the Graphite Store (Buffalo Grove, IL), part number BL001230. Figure 1.1 shows a simplified schematic of an all graphite hot zone reactor used in most experiments.

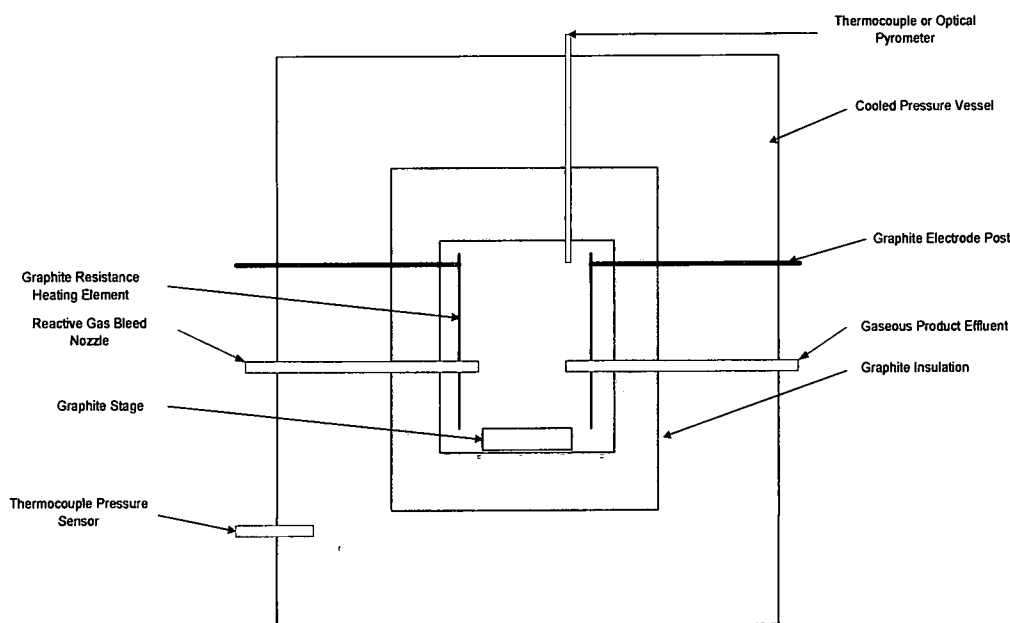


Figure 1.1. Graphite Hot Zone Reactor for Batch Processing

The reactive gas bleed nozzle and gaseous product effluent nozzle enable faster, more complete conversion than might otherwise be obtainable. Reactive gas is bled or pumped in, depending on the reactor conditions, directly into the reactor hot zone. In the case of air bleed into a graphite hot zone reactor, the oxygen reacts with the graphite nozzle and insulation to form carbon oxides *in situ*, thus providing a constant supply of reactive gas in the form of C_xO_y . Similarly, the gaseous byproducts are actively removed from the reaction zone by the effluent nozzle, in this instance attached to a rotary vacuum pump (Welch, Niles, IL, Model 1402). Thus reactants are constantly fed into the reactor, and byproducts removed, forcing the chemical equilibrium to the formation of carbon nanotubes, and thereby enhancing the rate of the desired reaction.

1.2.3 Process Overview

Carbo-Thermal Carbide Conversion (CTCC) is a process for selectively removing the metal or metalloid species from a crystalline carbide material while leaving the carbon species. The carbon remaining on the surface then graphitizes, forming carbon nanostructures. The process uses reducing gases to preferentially react with the metal/metalloid species, forming a vapor phase byproduct that is removed from the reactor *via* an effluent pump or condensation on a cold finger.

The substrates used are carbide ceramics, such as silicon carbide, in single crystal, polycrystalline or amorphous states. The carbide is present as a coating applied to a substrate by vapor deposition or as monolithic carbide materials

including powders, whiskers, and solid wafers. Thus, using the procedures and processes described here-in, novel carbon nanostructures are produced which are anchored on a substrate or free standing. Free standing (or bulk) SCNRs are fabricated as more or less interlaced clusters depending on the geometry, surface roughness and crystallinity of the starting carbide powder material. Interlaced SCNR clusters are formed by using starting material that is in the form of a powder consisting of individual particles that are polycrystalline and which are totally converted *via* the CTCC process.

The conversion process is best described as a high temperature anneal of the carbide starting material under a reactive atmosphere. Substrates are placed in a reactor and brought to temperature, typically 1400-1700°C. Care must be taken when choosing the source material and reactive gases to avoid side reactions that may hinder or prevent conversion. For instance, while ammonia is a reducing gas that will react with SiC, its choice is undesirable due to the possible passivation of the carbide via formation of nitrides on the surface. If oxygen is used in the reaction it will passivate the SiC surface with SiO₂ unless a reactive carbon source or other mechanism is used to convert oxygen to a reducing gas such as carbon oxide (CO or C_xO_y). Gas mixtures are chosen to selectively react with and remove the metal or metalloid from the material, creating the resulting carbon nanostructure. This is done by selecting a reactive gas that produces, for example, SiO as a product. SiO is a commercially valuable product and is relatively easy to handle and collect. This species is in the vapor phase at the temperatures involved

(above 870°C), and may be convectively removed from the hot zone via the effluent siphon or condensation on a cold finger.

Reaction time depends on the desired yield or conversion, with times typically ranging from 5 minutes to several days. Smaller product sizes and higher surface areas lead to faster processing times for equivalent mass of carbide, assuming an excess of reactive gas. Processing time also depends on the ratio of reactant mass to reactor volume. Gradual ramping of the reactor temperature may be used to prevent internal stresses within the substrate. Additionally, if an amorphous material is used, crystallization anneals serve to convert amorphous material to crystalline.

The process begins with a preliminary step of cleaning the surface of the carbide, if necessary, using high vapor pressure organic solvents such as acetone, alcohol, or hexanes. Oxides are removed by acid etching with hydrofluoric acid. Etching is done to remove oxide compounds that interfere with the growth process. For example SiC will passivate with exposure to oxygen, forming SiO₂ on the surface during manufacture (20).

The cleaned carbides are loaded into the reactor hot zone (see more detail in the examples below). The reactor is then sealed and evacuated using a mechanical vacuum pump (Welch 1402, Niles, IL). Typically, the reactor will operate between 0.1 and 10 Torr total pressure. Once the appropriate vacuum level is reached, the reactor is ramped to the process temperature at 3°C/min for the alumina reactor or 40°C/min for the graphite reactor. Once the process temperature is reached, the reactive gas is introduced via mass flow controller(s)

into the hot zone at the predetermined rate. After the reaction is allowed to proceed for the desired length of time, depending on the desired extent of conversion, the reactive gas bleed is stopped and the temperature cooled to ambient via natural cooling, typically 5 hours when using the graphite hot zone reactor described above. During this time, a vacuum level of 10^{-4} Torr is maintained. Once cooled, the vacuum is broken with ambient air to allow opening. The product is then scraped or otherwise removed from the reactor and collected for analysis or experimental use.

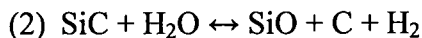
1.2.4 Reactive Gases

Reactive gases are chosen based on their ability to participate in the necessary redox reaction to produce elemental carbon (oxidation of carbon) and in the process form a volatile compound at the local temperature, which can be swept away in order to drive the equilibrium toward carbon production. Reactive gases used include H_2O , C_xO_y (carbon suboxide or monoxide), air, and admixtures of these gases. This work will focus on the most economical and safest process conditions, specifically the use of silicon carbide as starting material and H_2O vapor and carbon oxides formed *in situ* as the reactive gases.

The relevant reactions of SiC that occur within a graphite reactor zone at the appropriate temperature and in the presence of the appropriate reactive gases (oxygen and water) are believed to be:



And,

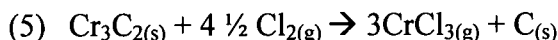
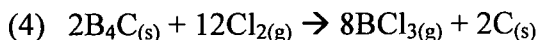
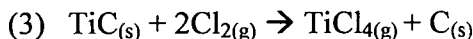
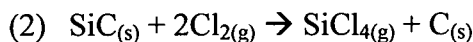
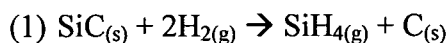


Carbon monoxide and suboxide are especially attractive for this process in their ability to aid in reaction as a carbon source. It has been shown previously that carbon monoxide and suboxide will form carbon particles in pyrolytic decomposition (21) (22). Carbon suboxide is produced *in situ* via reaction with oxygen and graphite components of the reactor (insulation and elements). Water is present as vapor in the air bleed. The presence of carbon suboxide was evident by a foul smell as described by Cotton (23). For all experiments cited in this work, relative humidity was controlled at 40 to 45% via the use of a gas bleed system. Compressed gas cylinders of dry air (21% O₂ and 79% N₂, AGA Gas, Dayton, OH) and 99.9% CO (AGA Gas, Dayton, OH) were used. Doubly distilled water vapor was supplied *via* vacuum evaporation. All reactive gases were supplied through a mixing manifold controlled by Omega Engineering (Stamford, CT) digital mass flow meters, FMA5510.

A generic reaction mechanism for carbide conversion is proposed below:

- Reactive Gas + Carbide \leftrightarrow Metal/Metalloid Byproduct + Carbon allotrope

where carbon (of the carbide) is necessarily oxidized, and the reactive gas and/or the metal/metalloid (of the carbide) is reduced. In addition to carbon oxides and water (Equations 1 and 2 above), carbides are also known to react with hydrogen and chlorine gas, as demonstrated in equations 1 through 5 below (24):



Thus, it is expected that these gases could be substituted for or used in combination with water and carbon oxides, such as carbon monoxide, to similarly form fullerenes or other carbon allotropes on or from carbide substrates. However, these reactions are not used in this work due to the handling issues created with hydrogen and chlorine gas, and products, liquid or gaseous silicon compounds that are poisonous and/or explosive. SiO has the advantage of being in the solid phase at room temperature, while gaseous at 870°C, and easily scavenged during reaction *via* condensation on the reactor walls or a cold finger. In addition, SiO is easily handled due to its low toxicity and chemical reactivity.

A reactive gas is chosen based on the desired chemical reaction and the other reactants involved. It is necessary that 1) the metallic component be reacted to form a gaseous compound at the processing temperature, 2) the reactive gas does not passify the carbide surface, 3) the reactive gas does not oxidize or reduce the carbon and 4) the gaseous product(s) of its reaction with the carbide does not competitively react with the carbon. To determine appropriate reactive gas bleed rates, work published by Kusunoki was used as a starting point (14) (19). In her

work, Kusunoki reports a reaction time of 1hr at 1700°C at 10^{-7} Torr produces a 200nm thick layer of CNTs on single crystal SiC. This reaction rate, 200nm per hour, was the basis for determining initial reactive gas bleed rates. This estimate was based on the percent conversion of planar SiC, using the height (change in thickness of the SiC wafer) of the resulting fullerene layer as a basis for the mass balance. The volume of SiC was used to calculate the mass of Si reacted, which was used to determine the amount of reactive gas needed for conversion.

1.2.5 Examples

A complete table of all the variations in the process is listed in the Appendix for reference (Table A.1). Specific examples demonstrating the validity of the process along with specific geometries most relevant to electrochemistry are described below. Alternative carbide starting materials are described to verify the broad applicability of the process to carbides in general. Silicon carbide is uniquely attractive for electrochemical applications as incomplete conversion of the carbide does not typically result in the presence of a reactive second phase (unconverted carbide), whereas iron or aluminum carbide would. Silicon carbide is also inexpensive compared with alternative carbides. Interestingly, regardless of processing temperature, carbon nanotubes (or their derivatives) do not form from amorphous starting materials.

Initial experiments in conversion of SiC powder yielded mixed results. Trays were initially loaded with thicker layers of SiC powder, approximately $\frac{1}{8}$

to ¼ inch thick. These early experiments failed to convert all of the SiC to carbon, predominately in the underlying layers of material. Thus, it was determined that mass transport was limited to the buried SiC particles. These experiments resulted in adoption of two key process parameters: thinner layers of SiC powder for conversion on trays, and use of reaction times in excess of those predicted using the planar SiC wafer experiments.

1.2.5.1 Example 1. SCNR Whiskers

The first example was intended to produce a SCNR material suited for paste electrode fabrication. The high aspect ratio material provides an ideal microstructure for non-linear mass transport to the electrode surface. Further, the mesoporous architecture of the resulting material should provide a novel adsorption/entrapment mechanism for both analyte and nanophase catalyst particles.

SiC whiskers (Alfa Aesar, Stock No. 38787) were loaded into a graphite hot zone reactor as received from the supplier. No pre-cleaning is necessary as multiple facets of the crystallites are exposed, offering multiple reactive surfaces. In this case, the particles of the starting material (SiC) have an aspect ratio of at least 5:1, length to diameter, and are defined as “whiskers”. The graphite hot zone reactor was used in this example. Isomolded graphite trays, 0.25in thick, and 12in square were used, separated by 1in cube graphite blocks, acting as spacers between the trays. The spacers allow enough free volume for mass transport of the

evolving gas phase product to be transported from the reactor bed due to concentration driven diffusion and convective flow from the feedstock and effluent streams. Each tray was dusted with powder to a thickness of 1/32 to 1/16 inch with the aforementioned SiC whiskers. The reactor was loaded with 10 trays, each holding approximately 5g of SiC whiskers. Additional trays may be used depending on the size of the reactor hot zone. The system was then evacuated to 1 Torr, and temperature ramped to 1700°C at 40°C/min. Six hours after 1700°C is reached, air/water vapor (40 to 45% RH) was introduced directly into the hot zone *via* a graphite gas nozzle at a rate of 60sccm via the Omega mass flow controllers. The 6 hour lag between reaching the reaction temperature and start of the reactive gas bleed was to allow complete utilization of the initial charge of moisture and air adsorbed on the reactor walls and material. This was done to ensure that the carbon oxides are the limiting reagent, allowing convenient control of the reaction. The graphite nozzle, resistive elements, and insulation serve to react with O₂ in the air bleed to form carbon oxides. Carbon monoxide is preferentially formed due to the large excess of reactive carbon present. Thus a supply of reactive gas was formed *in situ* and supplied constantly to the reactor. The process was allowed to proceed to the desired conversion. For this example, the reaction was allowed to proceed for 24 hours after 1700°C was reached. No gas was injected into the reactor during cool down. Figure 1.2 shows a typical Temperature/pressure – Time curve for production of SCNR whiskers using the procedure described above.

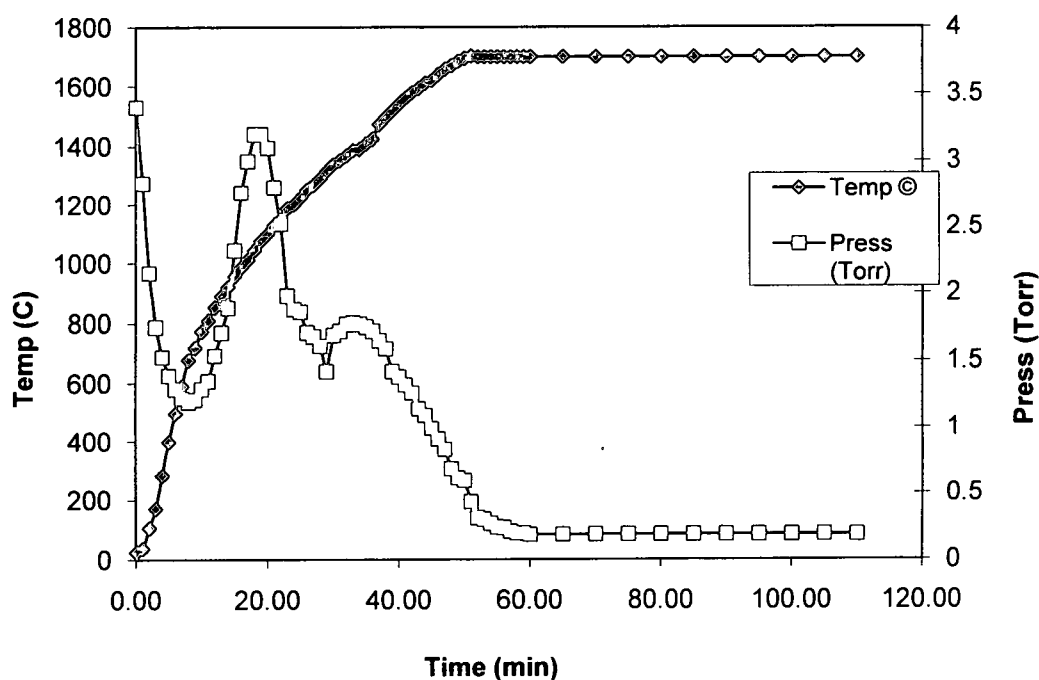


Figure 1.2. Time – Temperature – Pressure Profile of SCNR Whisker Production

The reactor was evacuated to approximately 3 Torr and heating begun. Initially, pressure declines sharply as air is pumped out. Beginning at approximately 550°C (10min), gases and moisture were desorbed from the starting material. This corresponds to the pressure increase beginning at approximately 10min and peaking at 20min (in this case). For larger batch sizes, a larger pressure peak was observed due to desorption of larger masses of water and organics from the raw material. Pressure steadily and sharply drops after desorption, until reaching a temperature of approximately 1300°C, where the chemical reaction of the carbide with the reactive gases begins. Pressure peaked (35min) as the residual gases present reacted with the carbide and then began to drop as the residual reactive species were consumed (40min). Pressure continued to fall, indicating

consumption of the initial charge of reactive gas, until steady state was reached (1hr) and remained at this low level (approximately 0.2 Torr) during the entire conversion process. Pressure was unaffected by the reactive gas bleed (started at 6hrs, in this case) due to the capacity of the pump exceeding the combined bleed rate and leak rate of the reactor. Reactive gas (humid air) bleed is typically started upon reaching 1700°C, but may be started at any point after pressure reaches steady state.

The finished product is shown in Figure 1.3. To prepare the sample for HRTEM imaging, a sample of SCNR whiskers was dispersed in methanol at 1mg/mL *via* sonication using a Cole Palmer (Vernon Hills, IL) Ultrasonic Bath, EW-08893. 50uL of the dispersion was pipetted on to a 400 line per inch TEM grid and allowed to dry before being imaged using a Hitachi H-7600 High Resolution Transmission Electron Microscope (HRTEM) at 80keV.

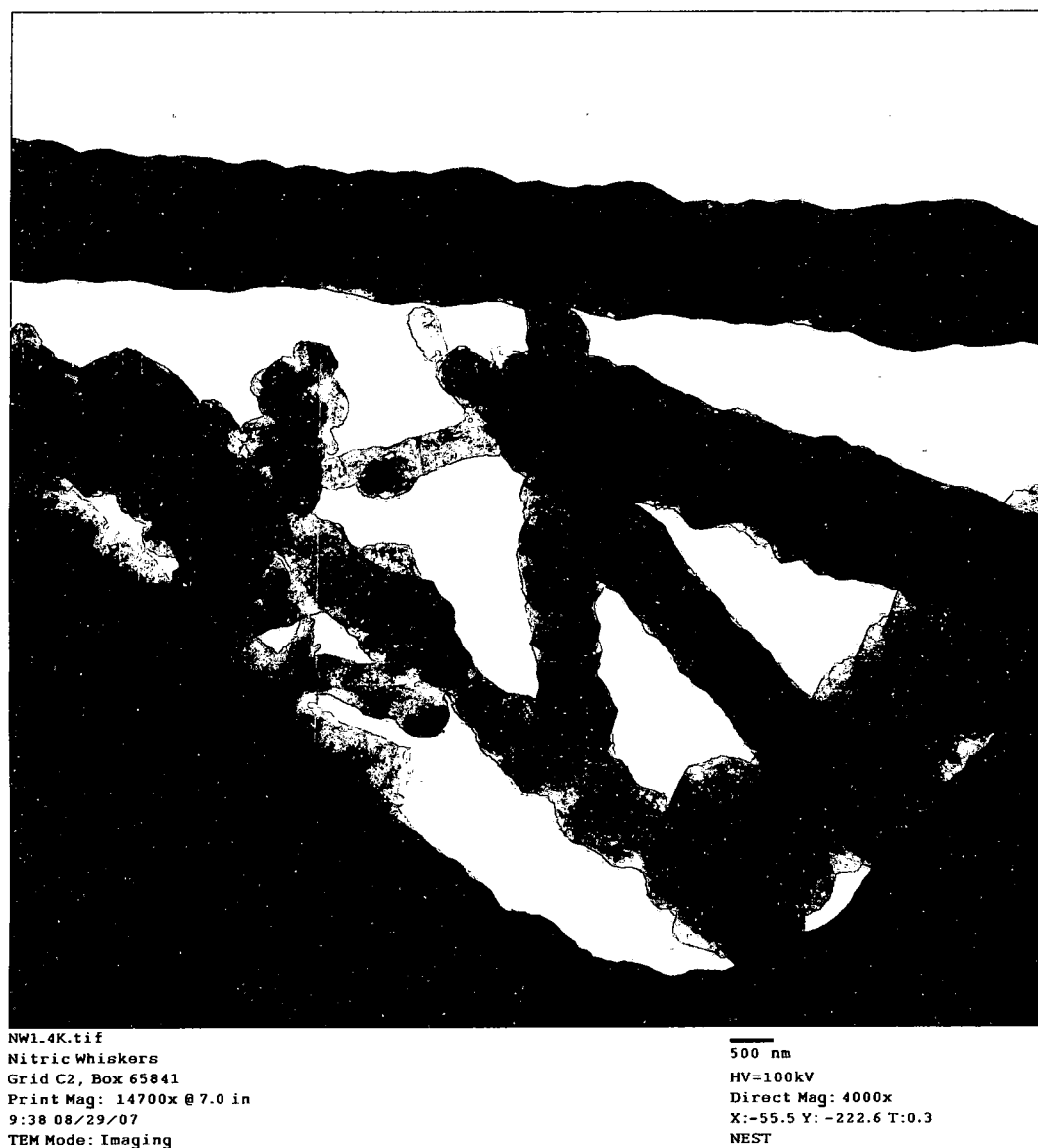


Figure 1.3. Low Magnification HRTEM Image of SCNR Whiskers

This image shows the general outward shape of the SiC whisker is retained after conversion of the carbide to the SCNR whiskers. Increasing magnification further reveals the interlaced SCNR architecture. Figure 1.4 shows the same material under increased magnification. The mesoporous architecture is more easily discernable at this magnification.



Figure 1.4. High Magnification HRTEM of SCNR Whiskers

Of particular interest in this image is the lack of catalyst particles typically seen in bulk CNT samples, seen as bright spots in electron micrographs. A novel mesoporous architecture is produced in the material, further increasing the potential utility for applications involving electrochemical capacitance or

enzyme/catalyst modification. A similar porous network is seen in all non-aligned SCNR arrays and clusters. Dark bands seen in the high magnification TEM image are a result of stresses induced in tight bends in the carbon structure (25).

1.2.5.2 Example 2. Planar Aligned Array

Great interest is shown in the literature for planar sensor arrays (26). Aside from the work done by Kusunoki, a review of the literature suggests few electrochemical sensors have been built using vertically aligned carbon nanotube arrays. This is no doubt a direct result of the presence of transition metal catalysts from the CVD production technique. CVD synthesis is the only other known process available for production of aligned CNT arrays. To produce aligned arrays of the carbide derived SCNRs, typically a single crystal polished and etched SiC wafer is obtained and cleaned with HF and ethanol prior to use. This pre-cleaning step is done to ensure no localized passivation of the SiC has occurred. This step is necessary only on substrates where a single crystal face is exposed. In all other instances, this step is omitted. Planar arrays are produced in small batches owing to the large purchase cost of SiC wafers. Nitrogen doped (N-type) 4H SiC wafers (University Wafers, South Boston, MA) are used for SCNR array production. Undoped wafers may be used for production, but are less attractive for sensor applications due to the electrically insulating nature of the underlying SiC layer.

Once cleaned, wafers were placed in a graphite hot zone reactor as described before, with the Si face up. If growth of fullerenes is not desired on the entire carbide face, a passivating layer of suitable composition may be deposited to pattern the surface. Suitable layers include silicon nitride, oxide, tungsten, and tantalum deposited *via* sputtering. The significance of the crystal orientation lies in the reaction rates observed. The Si face reacts significantly faster than the C face. Kusunoki provides some explanation for this observation (14). The system was evacuated prior to increasing the temperature. Temperature was ramped as before to 1700°C. Additional reactive gas was not necessary due to the small amount of source material present, as the residual air and adsorbed moisture left at 10^{-4} Torr were adequate for decomposition. Upon reaching 10^{-4} Torr, no variation in the pressure was seen. The reactor was maintained at 1700°C for 2hrs.

The height of the SCNRs varies directly with processing time until reaching a height of roughly 1 μ m, at which point, decay in growth rate was experienced. This was due to mass transport limitations of reactive gas to the carbide – carbon interface. Larger quantities of SCNR/CNT arrays may be produced per batch using influent reactive gas and gaseous product removal. A processed wafer was sectioned using a Focused Ion Beam (FIB) mill to allow a sufficiently thin cross section necessary for HRTEM imaging, Figure 1.5. This image was taken at WPAFB Materials and Manufacturing Directorate by J. Boeckl. In FIB sample preparation, a platinum layer was sputtered onto the array to allow smooth milling of a sufficiently thin sample for TEM imaging.

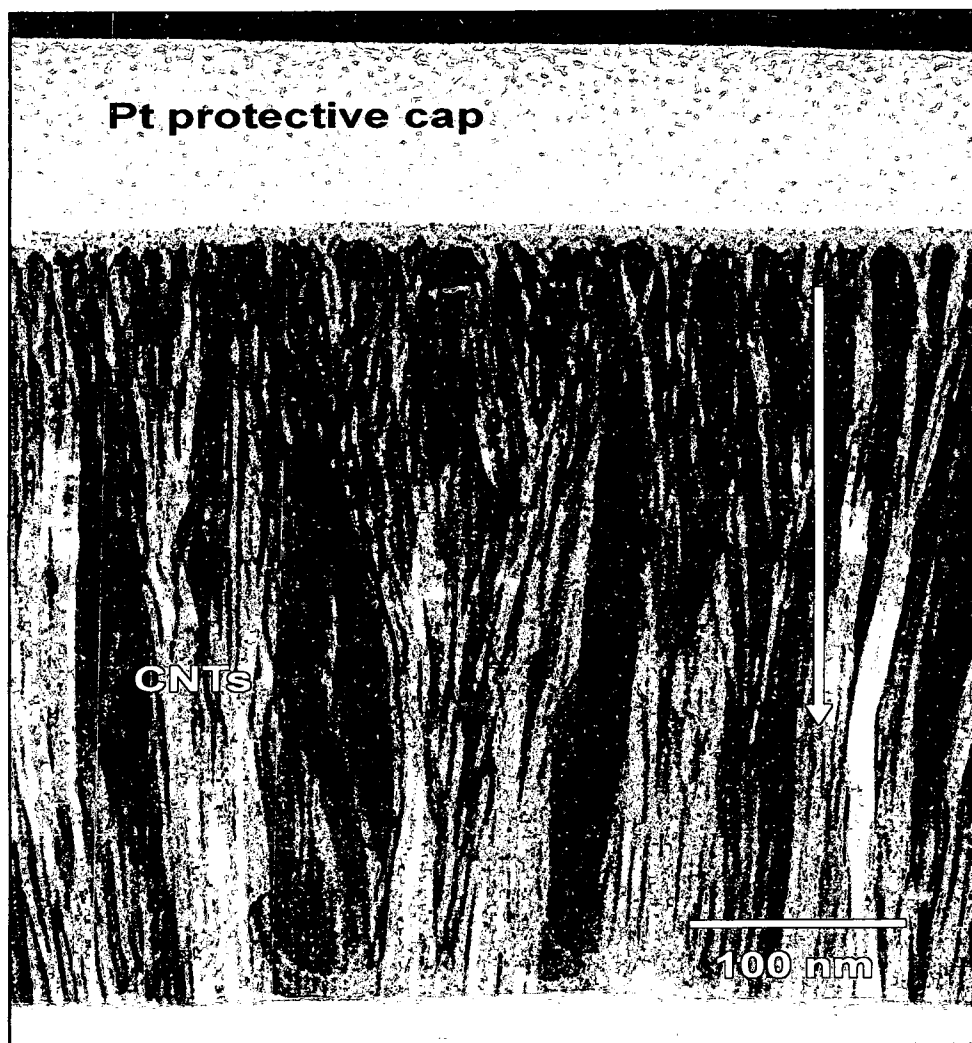


Figure 1.5. HRTEM Image of Aligned Array
(Image Courtesy of J. Boeckl)

This figure shows the dense forest of vertically aligned SCNRs produced via CTCC of a polished single crystal SiC wafer.

1.2.5.3 Example 3. Non-Planar SCNR Array, Open Cell Foam

There are many instances where a large electrochemical surface area material is desired that also allows for forced convection of solution through a self-supporting structure. As such, an open cell foam electrode provides an ideal platform for catalyst beds and fuel cell designs. A sample of ERG Materials and Aerospace (Oakland, CA) Duo Cell SiC coated reticulated vitreous carbon (RVC) foam was obtained at 45 pores per inch (ppi). It was noted that the material as received was polycrystalline, and therefore did not require further crystallization for processing into SCNRs. The sample was diced into 0.25in wide by 0.05in thick by 0.5in long pieces with a diamond saw. A fractured surface was imaged with a Scanning Electron Microscope (SEM) prior to conversion, at WPAFB to allow a cross sectional view, as seen below, by J. Boeckl, Figure 1.6.



Figure 1.6. SEM of ERG Aerospace Duo Cell SiC Foam
(Image Courtesy J. Boeckl)

Figure 1.6 shows a cross sectional view via Scanning Electron Microscopy (SEM) of a ligament of the open cell foam from ERG Aerospace (Oakland, CA). This material is comprised of a RVC core of approximately 45ppi density which is coated via CVD with a layer of 6-H polycrystalline SiC. The foam substrate was placed into a graphite reactor and the system evacuated to 1 Torr. The system was then heated to 1700°C at 40°C per minute, and maintained at that temperature for 2 hours. Additional reactive gas was not necessary due to the small amount of source material. Processing was identical to a planar array. Once processed via CTCC, a layer of adherent SCNRs was present on the surface of the foam. To

obtain a High Resolution Transmission Electron Microscope (HRTEM) image, a sample of the process foam was sliced from the foam using a Leo XB1540 Focused Ion Beam Mill (FIB). Figure 1.7 shows the mesoporous architecture of the resulting SCNR/CNT layer produced by CTCC. The reduced vertical alignment of the SCNRs on these foam materials as compared to the films grown from polished single crystal SiC wafers can be attributed to an increased surface roughness and to the polycrystalline nature of the SiC.

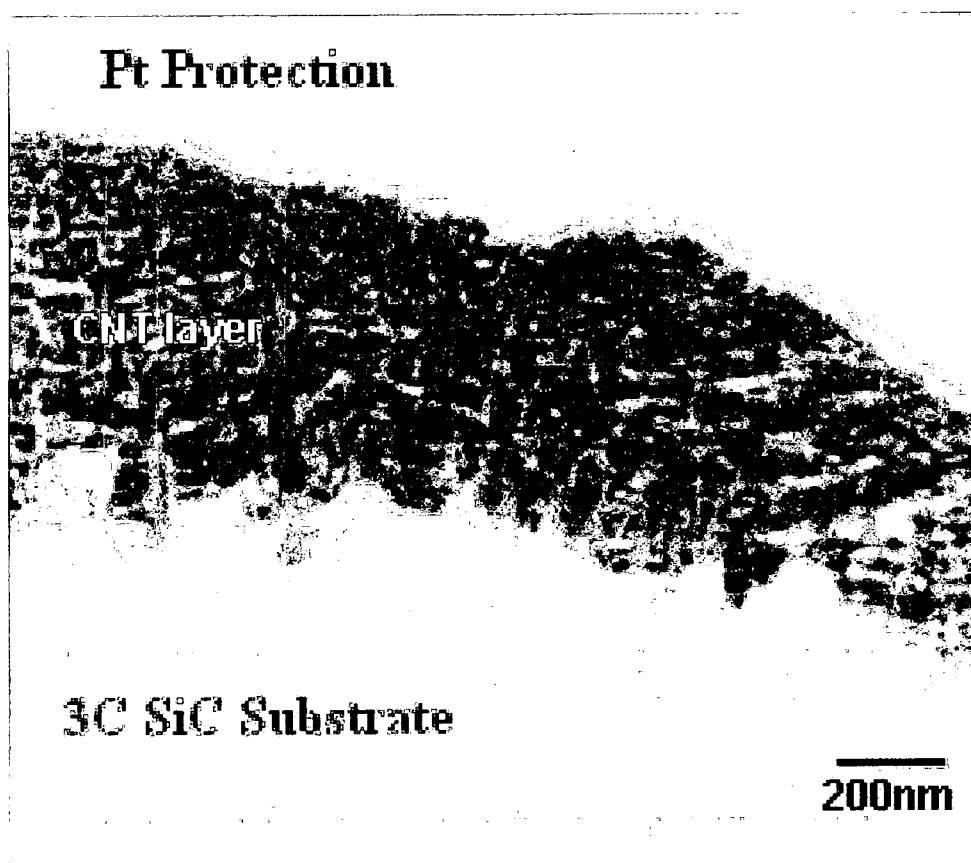


Fig 1.7. SEM of Non Planar SCNR Array
(Image Courtesy J. Boeckl)

1.2.5.4 Example 4. SiC Coated Carbon Fibers

Microelectrodes and ultra microelectrodes are gaining interest in applications where very small sample volumes are desired or required. Such examples include *in vivo* electrochemistry and determination of electron stoichiometries (27). To produce a microelectrode modified with an adherent layer of SCNRs, a sample of SCS-6 SiC coated carbon fiber was obtained from Specialty Materials, Inc. (Lowell, MA). This material, as received is amorphous SiC and coated with a thin layer of carbon as a lubricant. Therefore it was necessary to remove the carbon layer and crystallize the SiC prior to processing into SCNRs. This was accomplished by heating the sample in an alumina horizontal tube furnace to 1600°C for 96hrs in air resulting in crystallization and growth of a thick oxide layer. The carbon was oxidized off of the surface and the underlying SiC layer was passivated (thick SiO₂ layer), preventing unwanted decomposition of the SiC. Once cooled and removed from the furnace, the sample was cleaned with 25% HF for 24hrs to remove the passive oxide layer on the SiC. The samples were then processed *via* CTCC as in Examples 2 and 3. Conversion was allowed to proceed for 2hrs, as before. Figure 1.8, courtesy J. Boeckl of AFRL, shows a HRTEM of the resulting non-planar SCNR array after the same process was used to convert the SiC to SCNRs as with the carbon foam based non-planar array.

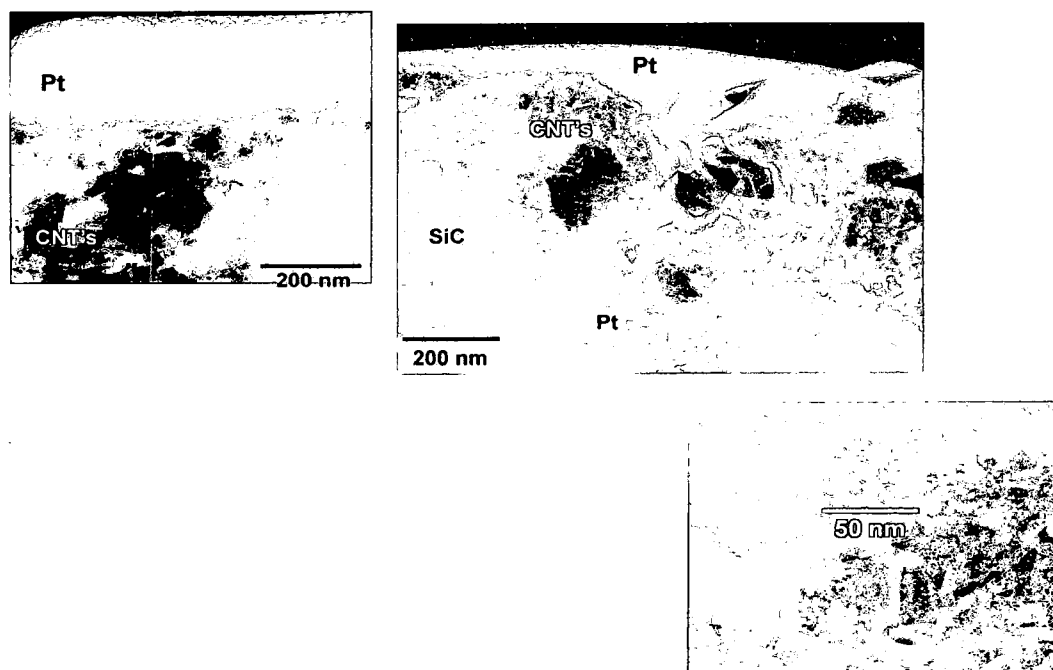


Figure 1.8. HRTEM of SCNR Coated Filament

A dense, non-aligned array of SCNRs was formed on the entire circumference of the filament. Like in Example 4, the array was intricately entangled, giving rise to mesoporous architecture of predominately edge plane carbon allotropes. This provides a unique microelectrode surface for electrochemical study.

1.2.5.5 Example 5. Large Production SCNR Nanoclusters

Example 5 represents an effort to demonstrate the scalable properties of the conversion process as well as to produce a novel mesoporous electrode structure with applications in catalyst entrapment and high surface area electrochemistry. Samples of SiC nanopowder were purchased from Sigma-Aldrich (St. Louis, MO), product 594911. The material was loaded into a

mechanically agitated reactor (or rotatable retort) capable of direct gas injection at temperature. A retort mechanically agitates the material, thus equalizing the carbide contact time with the reactive gas. Whereas before when using planar trays, mass transport of the reactive gas to the substrate or material relied solely on diffusion through the stagnant layer of reactive carbide. This slows the conversion process for the underlying layers of material. The retort was loaded $\frac{1}{4}$ to $\frac{1}{3}$ of volumetric capacity and installed into the reactor to avoid spillage from the effluent port on the retort. The system was then evacuated to 1 Torr and rotation of the retort started at approximately 5rpm. Temperature was then ramped to 1700°C at 40°C/min. Six hours after 1700°C was reached, 45% RH air was introduced directly into the hot zone via a graphite gas nozzle at a rate of 60sccm/min. Reaction was allowed to proceed for 72hrs after reactive gas was introduced to the reactor, then the reactor was shut down and allowed to cool. No gas was injected into the reactor during cool down, and the retort was stationary. Figure 1.9 shows the reactor modified with the graphite retort used for mechanically agitated production.

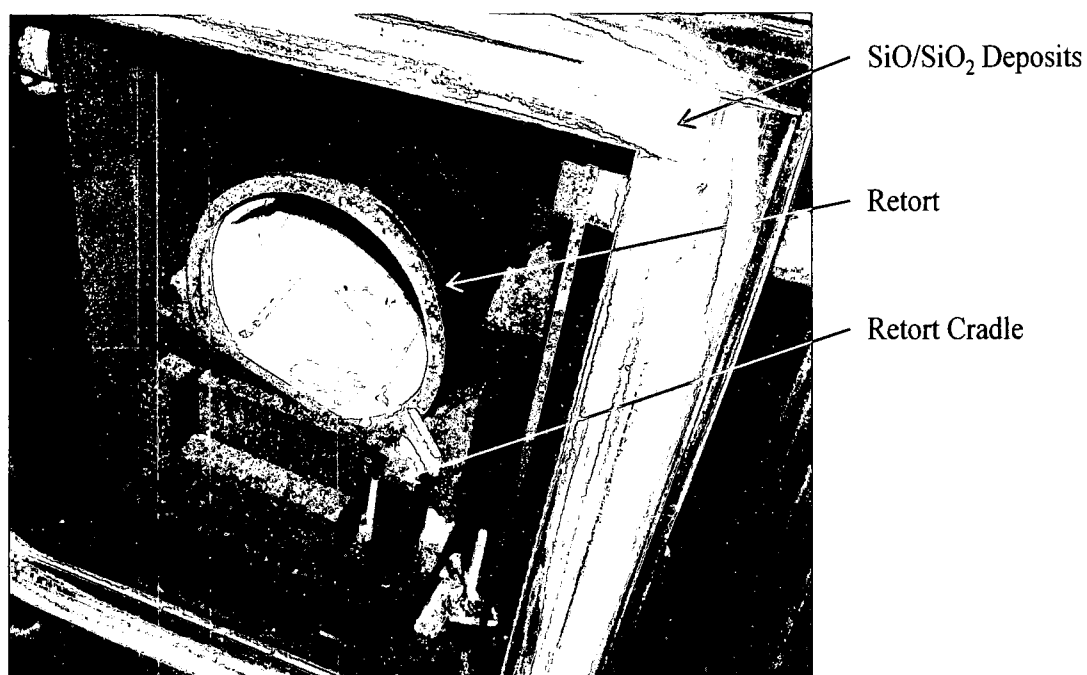


Figure 1.9. High Temperature Reactor with Retort

The retort is a graphite tube with an integral stud attached to the gas inlet side. Inside the retort are agitation blades, attached to the tube with high temperature carbon adhesive from the Graphite Store, part number 551RN. A total of 4 blades was used, equally spaced inside the retort. The effluent side of the retort was capped with a graphite plug, held in place *via* 4 ¼-20 graphite set screws. The retort was supported on a graphite cradle to provide strain relief during operation.

The following series of images was obtained with the help of J. Boeckl. Figure 1.10 shows the material as produced from this example in HRTEM at 25k magnification. As in the case of the SCNR whiskers, the outward geometry of the starting material was retained in the product.



Fig 1.10. HRTEM of SCNR Nanoclusters at 25k Magnification
(Image Courtesy J. Boeckl)

Figure 1.11 shows a SCNR nanocluster under 50k magnification, showing the mesoporous architecture resulting from polycrystalline carbide conversion.



Figure 1.11. HRTEM of SCNR Nanoclusters at 50k Magnification

Materials produced from this example were later used for electrochemical experiments in Chapter 3.

1.2.6 Alternate Carbide Examples

Examples of alternate carbide starting materials are given to demonstrate the broad applicability of the process. These examples were processed identically to Example 1. The graphite hot zone reactor was used for each example with a 45% RH air bleed as was used in prior examples. In each case the finished product was examined *via* TEM imaging to verify the presence of SCNRs. The Raman spectrum of each example is shown in the Appendix (Figure A.24 through A.27).

1.2.6.1 Example 6. Al_4C_3 Starting Material

Conversion of aluminum carbide was done to demonstrate the applicability of the process to another carbide system. This carbide is interesting due to its increased reactivity with water as compared with silicon carbide. This feature may be key to reduced process temperatures, alternate crystal structures, or increased production rates. However, additional experimentation is necessary to further explore the kinetics and thermodynamics of alternative carbide decomposition. Decomposition of the carbide has been described in the literature previously (28). Al_4C_3 , nominally 2.0 μ m particle size, was procured from Alfa Aesar (Ward Hill, MA) Stock No. 14038. The powder was utilized as received, with no pre-cleaning or treatment prior to use. 50g of the powder was dispersed evenly on to ten 12in by 12in by 0.25in thick medium grain extruded graphite plates, separated by 1in cube graphite blocks, stacked vertically. The plates were then loaded into a graphite hot zone reactor, evacuated to 1 Torr, and then heated to 1700°C at a rate of 40°C/min. Once at 1700°C, 45% RH air was introduced into the hot zone at a rate of 60sccm and the material allowed to react for 48hrs, then cooled without air injection to room temperature where the material was unloaded and examined. Analysis by Raman spectroscopy confirmed the presence of SCNR clusters (Figure A.24). This process is followed identically for other carbide examples that follow.

1.2.6.2 Example 7. B₄C Starting Material

Boron carbide, roughly 5.0 μ m particle size, was procured from Alfa Aesar (Stock No. 43002, Ward Hill, MA). The material was used as received, with no pre-cleaning or other treatment prior to use. 50g of the powder was dispersed evenly on to ten 12in by 12in by 0.25in thick medium grain extruded graphite plates, separated by 1" cube graphite blocks, stacked vertically. The plates were then loaded into a graphite hot zone reactor and evacuated to 1 Torr. The reactor was then heated to 1700°C at a rate of 40°C/min. Once at 1700°C, 45% RH air was introduced into the hot zone at a rate of 60sccm and the material allowed to react for 48hrs, then cooled without air injection to room temperature where the material was unloaded and examined. Analysis by Raman spectroscopy confirmed the presence of SCNR clusters, as shown in the Appendix (Figure A.25).

1.2.6.3 Example 8. TiC Starting Material

Titanium carbide, roughly 2.0 μ m particle size, was procured from Alfa Aesar (Stock No. 40178, Ward Hill, MA). The material was utilized as received, with no pre-cleaning or other treatment prior to use. 50g of the powder was dispersed evenly on to ten 12in by 12in by 0.25in thick medium grain extruded graphite plates, separated by 1in cube graphite blocks, stacked vertically. The plates were then loaded into a graphite hot zone reactor and evacuated to 1 Torr. The reactor was then heated to 1700°C at a rate of 40°C/min. Once at 1700°C,

45% RH air was introduced into the hot zone at a rate of 60sccm and the material allowed to react for 48hrs, then cooled without air injection to room temperature where the material was unloaded and examined. Analysis by Raman confirmed the presence of SCNR clusters, as shown in the Appendix (Figure A.27).

1.2.6.4 Example 9. ZrC Starting Material

Zirconium carbide, roughly 325 mesh particle size, was procured from Alfa Aesar (Stock No. 35808, Ward Hill, MA). The material was utilized as received, with no pre-cleaning or other treatment prior to use. 50g of the powder was dispersed evenly on to ten 12in by 12in by 0.25in thick medium grain extruded graphite plates, separated by 1" cube graphite blocks, stacked vertically. The plates were then loaded into a graphite hot zone reactor and evacuated to 1 Torr. The reactor was then heated to 1700°C at a rate of 40°C/min. Once at 1700°C, 45% RH air was introduced into the hot zone at a rate of 60sccm and the material allowed to react for 48hrs, then cooled without air injection to room temperature where the material was unloaded and examined. Analysis by TEM confirmed the presence of SCNR clusters, but due to size, decomposition was not complete. A Raman spectrum is shown in the Appendix (Figure A.26).

1.3 Verification of Silicon Carbide Chemistry

A significant portion of the value of this work is associated with the demonstration that carbide degradation is due to chemical reaction. Until now, the conversion process was believed to be either physical in nature (sublimation) or direct *oxidation by O_2* of silicon carbide (14) (19). Both of these proposed mechanisms are significantly flawed. Because silicon and carbon are covalently bonded, it is impossible to physically remove one species, silicon or carbon, without chemical reaction. This would be possible if silicon carbide were an *alloy* of silicon and carbon, not covalently bonded. The second proposed mechanism is flawed due to the self passivation of carbides in general, and silicon carbide in particular. Exposure of silicon carbide to elemental oxygen quickly forms surface films of SiO and SiO₂ (29).

To gain insight into the reaction products, and therefore the reaction mechanism, a cold finger was installed into the reactor to collect vapor phase byproducts. Direct investigation of the reactor headspace *via* spectroscopy was impractical due to the high temperatures involved. However, in contrast to the work done by Kusunoki, the greatly increased mass of reactants and consequently products used in this process, enable collection of vapor phase (in the reactor headspace) products for analysis. Figure 1.12 shows the white residue deposited after production using SiC starting material and humid air gas injection.

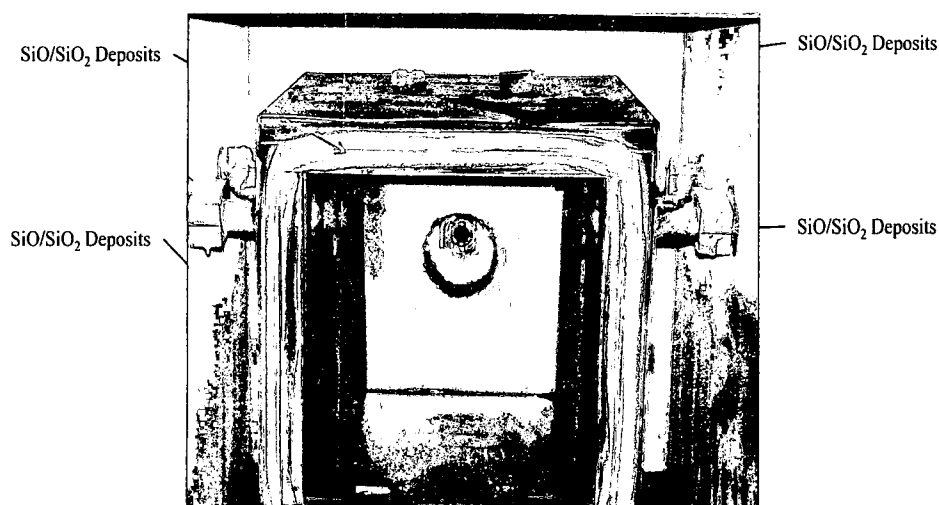


Figure 1.12. Post Production Picture of Reactor Showing SiO/SiO₂ Deposits

Using a new hot zone, including insulation, trays, and elements, a 50g batch of SiC whisker conversion with 45% RH air bleed, run was done in a freshly cleaned reactor. Samples of the white deposits left from the run were collected for analysis. Analysis was done *via* Ion Coupled Mass Spectroscopy (ICP-MS) at Galbraith Laboratories. The results indicated a 1:1.3 Si to O atomic ratio, suggesting a mix of SiO and SiO₂. Closer examination of the outside of the hot zone yielded a thin film deposit of material. Careful scraping of the material from the graphite foil on the insulation and ICP-MS analysis at Galbraith Laboratories indicated a nearly pure SiO film (composition: 47atomic% Si, 51atomic% O, 2atomic% C). It is believed that trace amounts of SiO₂ were present in the film, and the carbon source was the graphite itself. Figure 1.13 shows the deposition of silicon oxides on the hot zone cover and interior reactor walls.

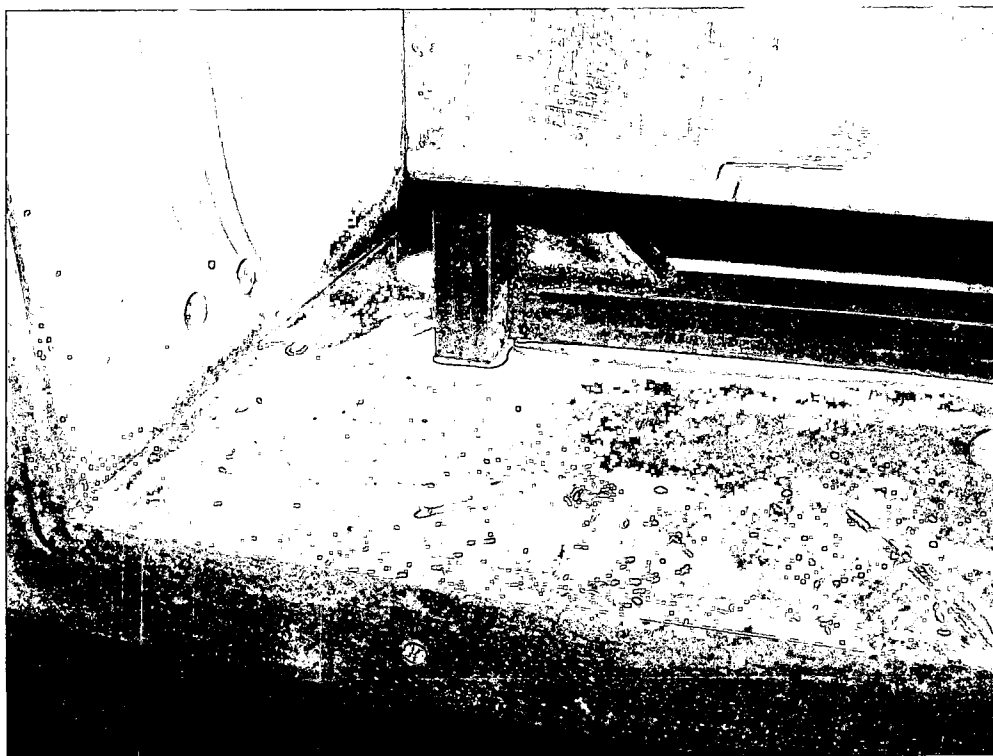


Figure 1.13. Picture Showing SiO/SiO₂ Deposits

A more rigorous mass balance was then performed on the SiC species during CTCC. 1.0000g of SiC nanopowder (Aldrich, 594911) was added to the conversion trays similar to *Example 1*. 45% RH air was supplied slowly at 5sccm, as a rate limiting reagent, but allowing the conversion to reach completion with excess time (24hrs). A 2 inch diameter superfine isomolded graphite bar (Graphite Store, IL, GT001593) was purchased and modified to act as a cold finger capable of insertion directly into the hot zone. Figure 1.14 shows a schematic of the cross section of the cold finger used in collection of the condensable reaction products in the reactor headspace.

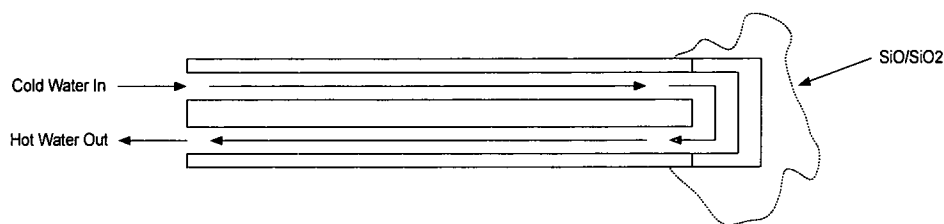


Figure 1.14. Cold Finger Design for Collection of SiO/SiO₂

The cold finger was inserted 2 inches into the hot zone of the reactor and sufficient water flow was used to avoid boiling in the finger. The reactor was then started, and the process proceeded normally. The run was allowed to continue for 24hrs at 1700C to ensure complete conversion of all the SiC nanopowder to SCNR clusters. The SCNR clusters were collected, weighed, and recorded as yield of fullerene in Table 1.1. The reaction byproduct (silicon oxide), was carefully scraped from the cold finger and weighed (1.1100g total mass of oxide). Both samples were sent to Galbraith Laboratories for analysis *via* ICP-MS. Table 1.1 shows the mass balance of the carbon (fullerene product) and silicon. Galbraith was instructed to dry the samples under vacuum at 120C for 24hrs prior to analysis to ensure no adsorbed moisture was present during the test.

Phase	Elemental Composition (atomic % / mass collected) – Material Balance				
	Silicon	Oxygen	Carbon	Yield (C or Si)	Theoretical Yield
Fullerene	0.01%	0.01%	99.97%	0.3185g	0.2996g
	NA	NA	0.3185g		
Silicon Oxide	41.0%	58.9%	0.01%	0.6872g	0.7004g
	0.6872g	0.4228g	NA		

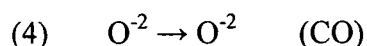
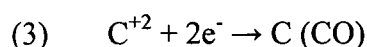
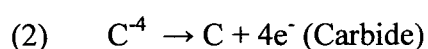
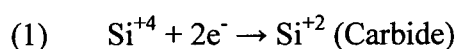
Table 1.1. Mass Balance of CTCC Conversion of SiC Nanopowder

The yield of silicon was lower than predicted due to incomplete recovery by the cold finger. Also, the analysis revealed a higher than expected oxygen content in the byproduct. It was expected that the reaction would yield predominately SiO, while the experiment indicated a stoichiometry of SiO_{1.47}. This is likely due to conversion of some SiO to SiO₂ through the use of excess reactive gas to ensure complete conversion of the carbide. Excess air/water entering the reactor hot zone could further oxidize the SiO present in the gas phase prior to condensing on the cold finger. Of particular noteworthiness is the apparent higher than stoichiometric production of carbon. This can be explained by the consumption of at least some of the C_xO_y (carbon monoxide/suboxide) reactive gas to form carbon nanotubes/nanorods. This phenomenon has interesting implications for the production of doped carbon nanotubes and their derivatives. If, for example, an appropriate admixture of C_xO_y and a reducing gas consisting of some component of boron is chosen, it would be possible to uniformly and controllably dope the product with boron. Such a gas may be BCl₃, or similar reducing gas.

The previously proposed decomposition mechanism by Kusunoki relies on higher vapor pressure of the silicon vs. carbon at elevated temperature (30). This theory does not account for the necessary electron balance needed due to the covalent nature of the carbide bonding. Based on the results shown in Table 1.1, a new reaction is proposed, Equation 1, below,



Notice that silicon is reduced in this reaction, going from an oxidation state of +4 to + 2, and carbon (of the carbide) oxidized from – 4 to 0. Without including CO in the reaction, there is a charge imbalance for the carbide material. This confirms that the reaction relies on the presence of a second reactant, the reducing gas. The following electron balanced equations support the newly proposed reaction:



This mechanism leads to an overall charge balance. Further support that the newly proposed mechanism is indeed the correct one is based on the analysis of residual material formed on the cooled walls of the reactor and cold finger (Table 1.1), which when analyzed was identified as predominately SiO. Although SiO is a gas when formed in the hot zone of the reactor, it subsequently condenses on the cooler walls of the reactor outside the hot zone. This is direct, empirical evidence that the formation of CNTs or SCNRs is a result of a chemical reaction of carbide ceramics and a reactive gas phase.

1.4 Conclusions

A process for the generic conversion of carbides into carbon nanotube materials is described. The process has been demonstrated with several engineering relevant carbide source materials. Of particular interest is the implication of scaling the process where increased production may be realized through agitation *via* mechanical mixing. Economy of production lays in the nature of suitable reactants, which are typically abrasive grade SiC and filtered 45% RH air. Complete conversion of multiple geometries of carbides is also shown.

This work is the first to suggest that carbon monoxide and suboxide are actually involved in the formation of fullerenes in the graphite reactor used. This has interesting implications on potential future processes and chemistries where reaction rate and extent of reaction may be enhanced greatly by increasing the partial pressure of suboxide in the reactive gas. Direct empirical evidence is shown supporting the hypothesis that the degradation of silicon carbide is a result of chemical reaction, not physical degradation.

CHAPTER 2.

CHARACTERIZATION OF CATALYST FREE CARBON NANOMATERIALS

2.1 Introduction

Three characteristics are necessary for a successful carbon nanotube production process: economy of scale, consistency of product, and purity. Economic factors are outside the scope of this work, but will be generally addressed in the Conclusions. Nearly all conventional processes rely on some form of transition metal catalyst to improve reaction yield to an acceptable level. The use of catalysts necessarily influences, at a minimum, two of the aforementioned characteristics: cost and purity. Strict control of catalyst and process parameters have reportedly led to the production of highly consistent materials from the company Southwest NanoTech (SWeNT), in particular, with a very high percentage of SWCNTs of consistent chirality (US Patent 7,354,881). However, this is not the rule, rather the exception. In all cases the use of metal catalyst results in unacceptable impurities for electrochemical applications. Regardless of the purification route employed, it is impossible to remove enough catalyst to result in an electrochemical grade material.

This has been shown multiple times, most notably and convincingly by Banks (31). So called “super washing” has also been demonstrated as largely ineffective in purification to a level necessary for electrochemical applications. Further evidence of persistent catalyst contamination is given by Pumera, who states that nanoparticles of catalysts are often sheathed, and thus shielded from acid attack (32). The use of as produced, via CTCC, material in electrochemical applications has not yielded any such misleading results. Various techniques are employed to determine the extent of metal contamination, while direct electrochemical investigation remains the most relevant and sensitive. Consistency is the second physical key for successful CNT technology. Physical parameters such as diameter, length, aspect ratio, and chirality effect the chemical and electronic properties of fullerenes. Consistency is best shown via electron microscopy and verified by Raman spectroscopy.

2.2 Purity Characterization

Samples of SCNRs were sent for elemental analysis to an external laboratory for verification of purity. Table 2.1 lists the composition of typical SCNRs as produced in this work. Testing was done by Galbraith Laboratories (Oakridge, TN) by ICP-MS. The technicians were instructed to dry samples for 24 hours under vacuum at 90C prior to analysis to ensure adsorbed moisture would not interfere with the test. The materials were tested for carbon, oxygen, silicon, and iron.

Material	Lot No.	Species Tested For	Mass %
SCNR Nanoclusters	FebCentorr06	Carbon	99.91
		Oxygen	<0.05
		Silicon	0.08
		Iron	<LDL
SCNR Whiskers	111407Whisker	Carbon	99.98
		Oxygen	<0.05
		Silicon	0.01
		Iron	<LDL

Table 2.1. Elemental Analysis of CTCC Produced Materials via ICP-MS
(Galbraith Laboratories)

While ICP-MS is an extremely sensitive test for elemental composition, Energy Dispersive X-Ray Analysis (EDS) is attractive as it is quite common for electron microscopes to employ these instruments as integral parts of the system. Thus, EDS was used for analysis of another lot of material produced. Figure 2.1 shows an EDS analysis of SCNR clusters, indicating 99.87% carbon content. Comparison of both tests shows good agreement in the compositional analysis. This spectrum was obtained at WPAFB with the assistance of J. Boeckl.

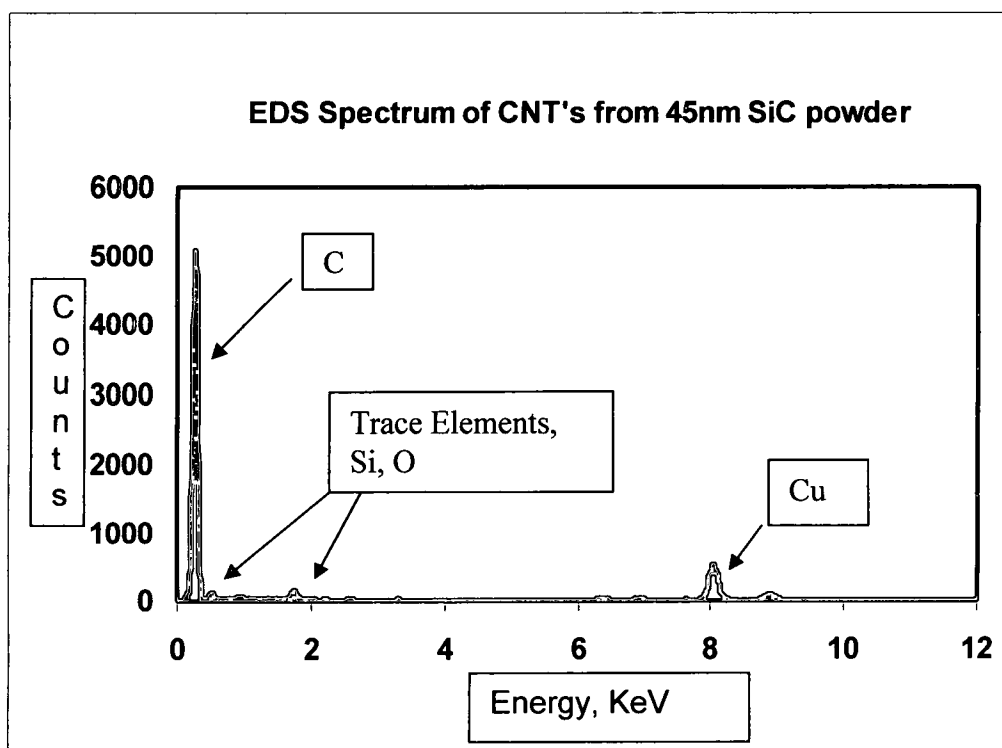


Figure 2.1. EDS of SCNR Nanoclusters
(Image Courtesy J. Boeckl)

The EDS spectrum of the nanomaterial in Figure 2.1 shows only carbon and copper (8 KeV). The source of copper in the spectrum is the copper TEM grid used as the sample support. Trace amounts of oxygen and silicon were present, at levels less than 0.1% each. This experiment provides additional direct evidence for the high purity of material produced with the CTCC process.

ICP-MS and EDS have shown CTCC synthesized fullerenes are significantly more pure than commercially available CNTs, which are advertised as 95% or less carbon.

2.3 Raman Spectroscopy

Raman spectroscopy is a very powerful technique for the investigation of electronic structure, generally in carbon, and specifically carbon nanostructures. It is widely recognized as the most definitive analytical tool for fullerene study, and for carbon nanotubes in particular (33). This analytical tool employs a laser for exciting atoms to specific vibrational and rotational states. Relaxation to ground state results in the emission of photons of different wavelength than the excitation source. The wavelength and intensity of scattered laser light is measured and indicates specific changes in vibrational and rotational energies of the scattering molecules, which are dependent on molecular symmetry. The wavelength and intensity of the scattered light also depends on the wavelength of the laser used for excitation. Raman spectra of CNTs are rich with information on chirality, electronic conductivity, physical dimensions, defect or disorder content, type, and electronic structure. A thorough understanding of the information and basis for the interpretation of Raman spectroscopy is vital to the understanding of the electronic, electrochemical, thermal and mechanical properties of CNTs.

Of particular interest in cylindrical and tubular nanostructured crystalline carbon such as SCNRs and CNTs are: Radial Breathing Mode (RBM) vibrations, typically in the range of 100 to 400 cm^{-1} which are often used to determine diameters of CNTs and verify the presence of tubular structures such as concentric rings of CNTs and SCNRs; “G” band vibrations, typically around 1580 cm^{-1} , indicating in plane vibrations; “D” band vibrations- often termed

“defect band”, typically around 1350cm^{-1} , indicating disruptions in the sp^2 bonds ; and “G*” band vibrations, typically around 2650cm^{-1} , which are second harmonics of the G band transition. These features are classified as either first order (or electronic transitions), or second order (phonon processes). Raman spectroscopy in its varied forms can be used to investigate the electronic structure and physical dimensions of CNTs. Consequently, Raman spectroscopy can be used as a definitive tool to differentiate various carbon crystalline structures. Improper application of Raman spectroscopy has lead to significant misinterpretations of results. For example, it is often cited in the literature that MWCNTs have no RBM signal, when in fact *all* CNTs display a diameter dependant RBM (18). However, with significant variations in diameter, the signal-to-noise ratio between the RBM signal and background noise becomes so low as to prevent detection. Additionally, MWCNTs have been characterized by having broad D and G bands when compared with SWCNTs. Again, this is an artifact of the large variations in tube structure, specifically diameter (18). Whereas the G bands of fullerenes are attributed to in-plane resonance, the D band may be derived from multiple sources. This includes amorphous carbon impurities as well as side wall defects (34). Fullerenes exhibit a disorder induced D band due to loss of transitional symmetry (35). Sources of the D band include: sidewall defects, amorphous carbon impurities, bending, and finite size defects. Thus, the use of other overlapping characterization techniques, such as HRTEM microscopy, becomes vital in the study of any nanoscale fullerene material. Because material produced *via* CTCC contains negligible amounts of non-

crystalline carbon, it exhibits low D band intensities using a 514nm excitation laser as compared with that of other commercial materials, such as MWCNTs. When a 785nm laser is used, side wall defects and internal kinks become the major source of D band intensities. Thus, a significant increase in the D band is observed as compared with that of the commercial material investigated.

Raman spectra of selected materials were obtained on a Renishaw (Gloucestershire, UK) *inVivo* Raman Spectrometer with green (514nm) and red (785nm) laser sources. A carbon SEM “dot” was used to affix the CNT samples to a standard flint glass microscope slide. 0.1g of nanomaterial was deposited onto the dot and compressed with another glass slide. Non-adherent material was shaken from the dot prior to analysis. This procedure was used for each example. In each instance shown, the spectrum was obtained at 10% laser power, 60s excitation time, with two integrations. Figure 2.2 shows a Raman spectrum of commercially available MWCNTs from Alfa Aesar, showing the characteristically large D:G ratios using a 514nm excitation laser as a result of significant amorphous carbon contamination. The major features are indicated in the spectrum. These include the D band at approximately 1350cm^{-1} , G band at 1580cm^{-1} , and G* band at 2700cm^{-1} . All spectra shown are background corrected.

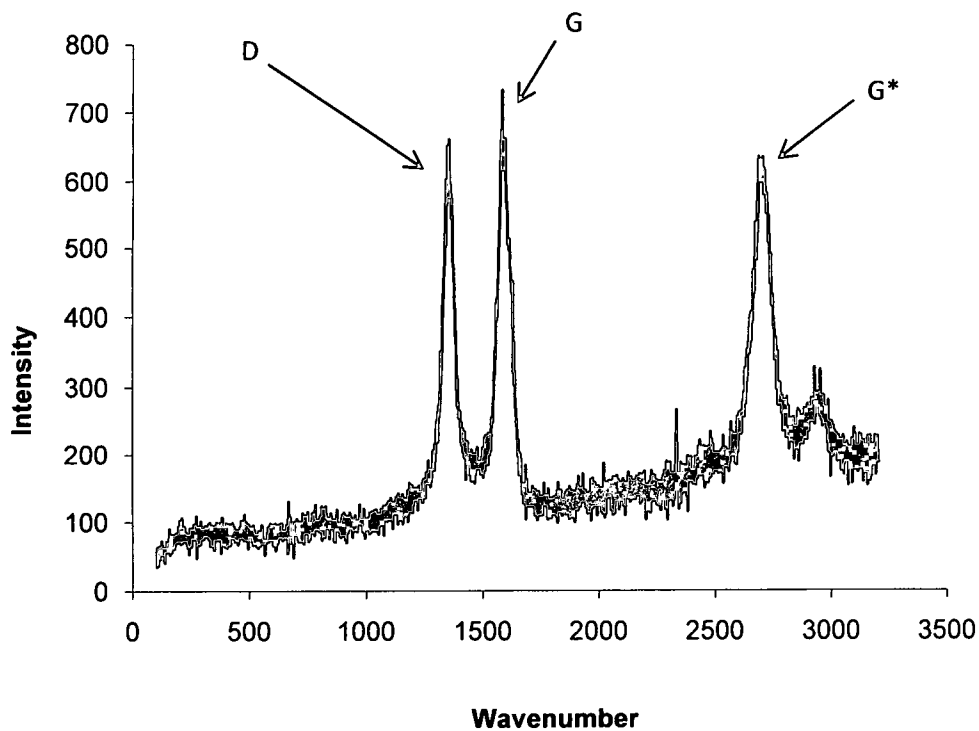


Figure 2.2. Raman Spectrum of Alfa Aesar MWCNTs using a 514nm Excitation Laser

Figure 2.2 clearly shows the broad G (1580cm^{-1}) and D (1350cm^{-1}) peaks commonly associated with MWCNTs. Also shown is a strong G* (2700cm^{-1}) band. Spectra similar to these have become representative of nearly all commercially available MWCNTs. Figure 2.3 is an analogous spectrum taken of NanoLab (Newton, MA) MWCNTs.

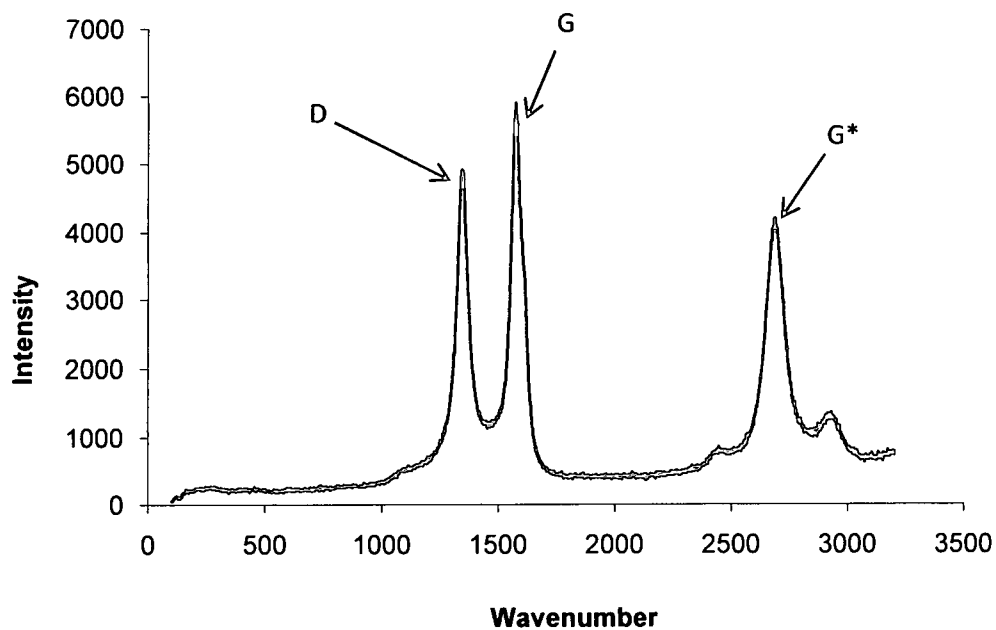


Figure 2.3. Raman Spectrum of NanoLab MWCNTs Using a 514nm Excitation Laser

Figure 2.3 more clearly shows the classical Raman spectrum of CVD synthesized MWCNTs. Figure 2.4 shows the Raman spectrum of the Alfa Aesar MWCNTs samples using a 785nm excitation frequency.

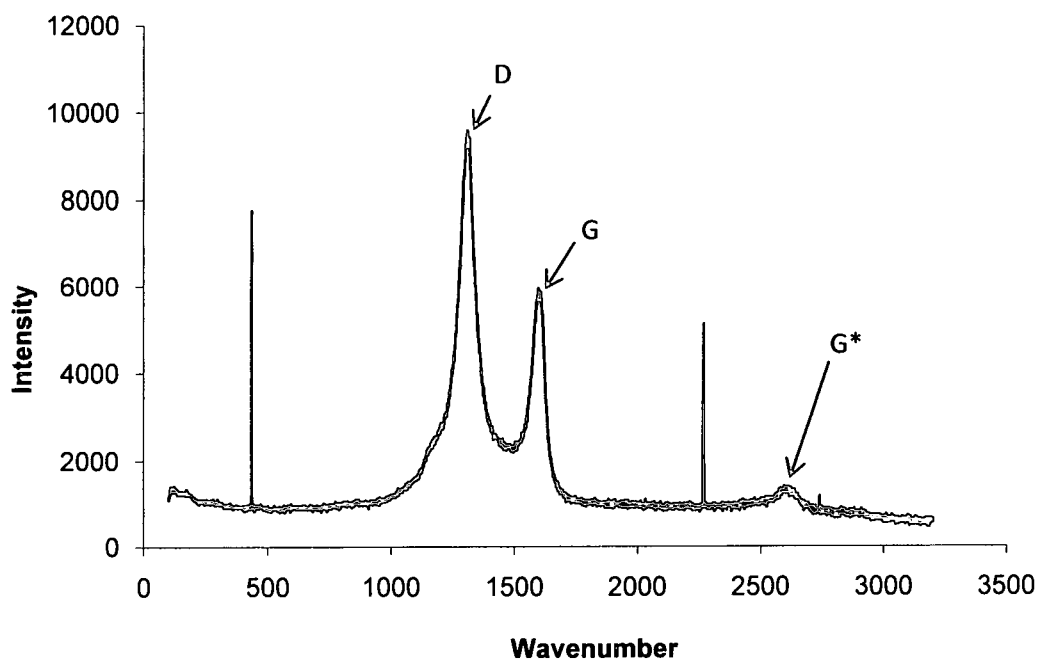


Figure 2.4. Raman Spectrum of Alfa Aesar MWCNTs using a 785nm Excitation Laser

Characteristically large, broad peaks are again present in the commercial MWCNTs. The broad peaks in the spectrum indicate variations in diameter, length, and chirality. Figure 2.5 shows the analogous spectrum for NanoLab Research Grade MWCNTs.

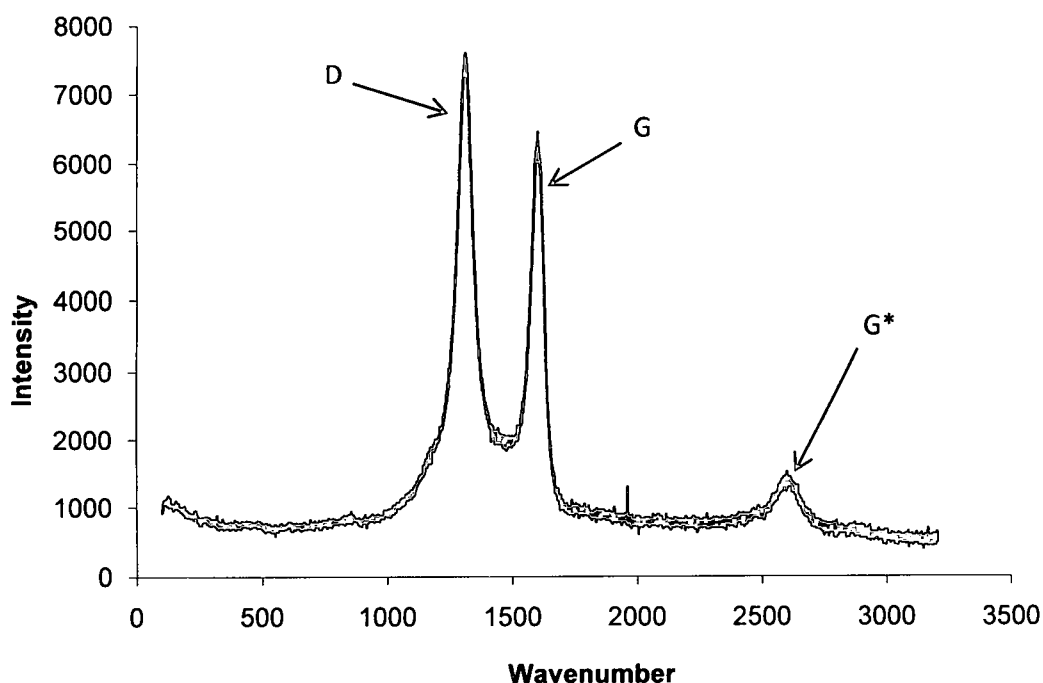


Figure 2.5. Raman Spectrum of NanoLab MWCNTs using a 785nm Excitation Laser

Figures 2.1 through 2.5 are typical of what one would expect from conventional MWCNTs produced via chemical vapor deposition – large D:G ratio, obscured RBMs, and broad peaks resulting from the distribution of chiralities and geometries. These spectra are shown for comparison purposes to the as produced SW/MW-SCNR materials produced via CTCC. Figure 2.6 shows the Raman spectrum of typical SCNR materials using a 514nm excitation frequency. The process to produce these materials was outlined in the examples described in Chapter 1.

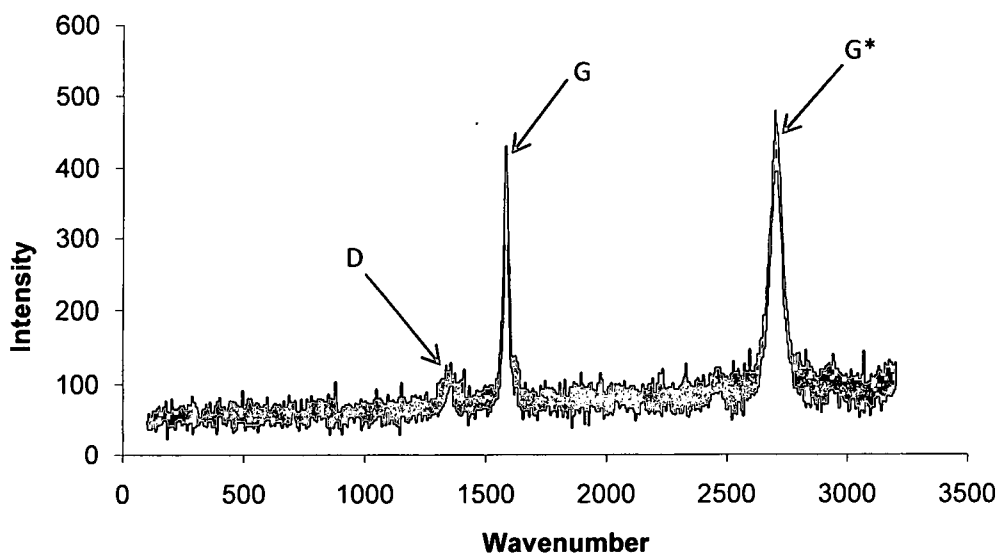


Figure 2.6. Raman Spectrum of SCNR Nanoclusters using a 514nm Excitation Laser

Particularly noteworthy in the spectrum is the much reduced D:G ratio seen as opposed to commercially available MWCNTs, indicating negligible amorphous carbon content. Figure 2.7 shows the analogous Raman spectrum of SCNR whiskers, as produced in *Example 1*.

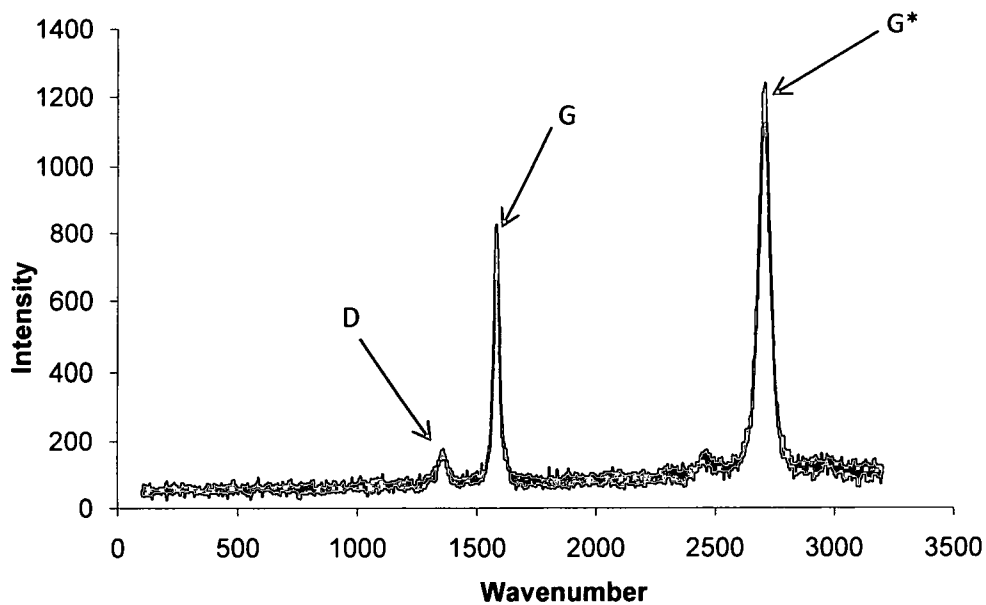


Figure 2.7. Raman Spectrum of SCNR Whiskers using a 514nm Excitation Laser

Of note in the SCNR whisker spectrum is the sharp, well defined G peak, very large G* band intensity, and the smaller D:G band ratios as compared with the commercial CNT material. Figure 2.8 shows the Raman spectrum of nanoclusters using a 785nm excitation laser.

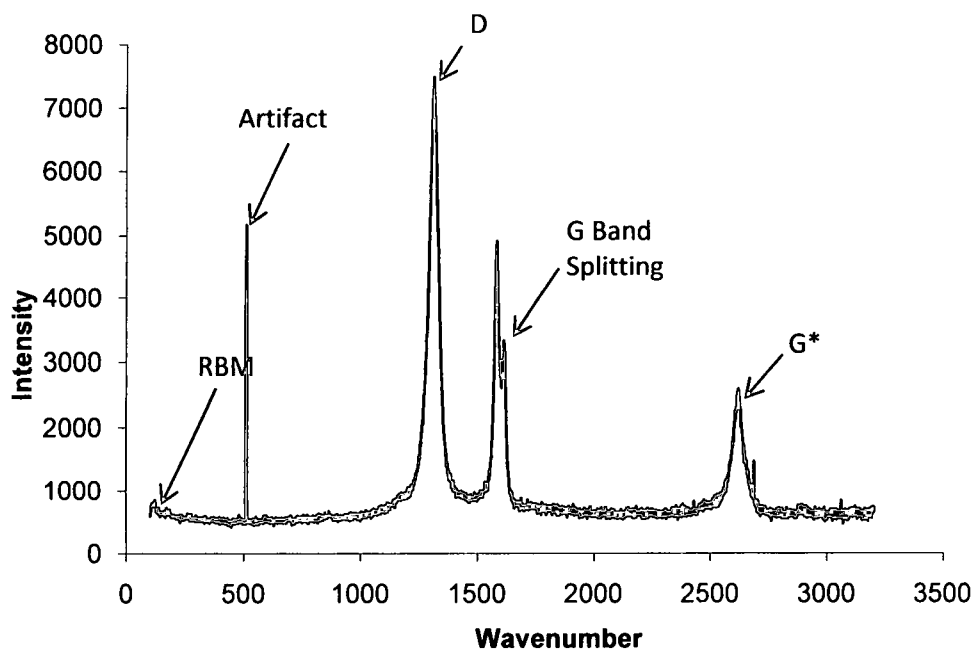


Figure 2.8. Raman Spectrum of SCNR Nanoclusters using a 785nm Excitaion Laser

Figure 2.8 is particularly interesting as it shows distinct splitting of the G peak into the G^+/G^- peaks. This is typically only seen in individual CNTs. Splitting of the G peak into separate peaks is largely due to diameter consistency, allowing the resolution of the tangential and in plane excitation and relaxation modes. Figure 2.9 is the analogous spectrum of the whisker material.

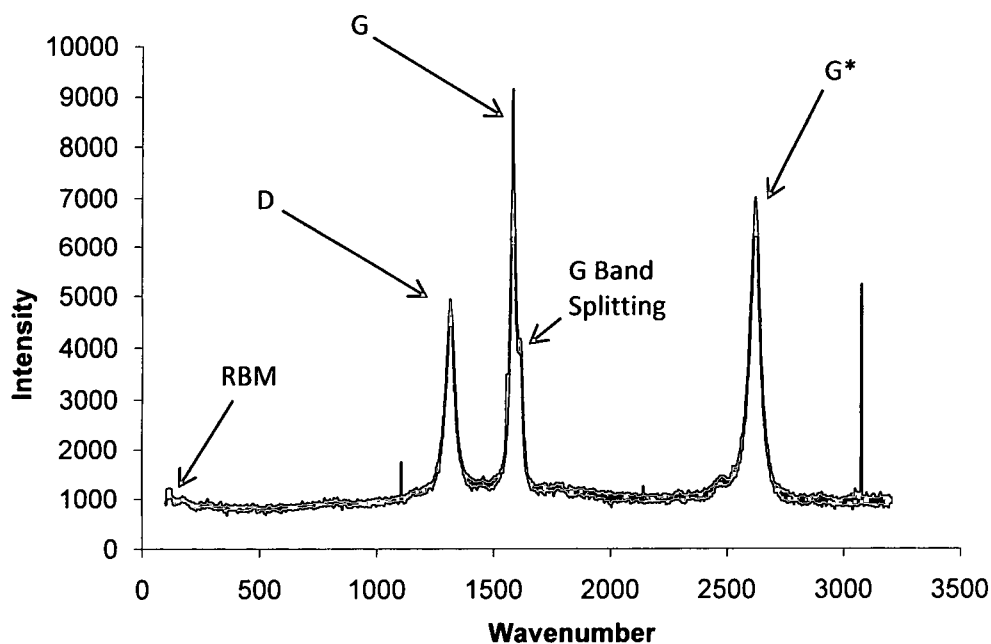


Figure 2.9. Raman Spectrum of SCNR Whiskers using a 785nm Excitation Laser

The 785nm excitation frequency allows observation of two key features in SCNR morphology as compared with MWCNTs, verifying the consistency and utility of the material. Firstly, note that the D and G peaks are significantly narrower in width than the commercial MWCNT materials. This is a direct result of the consistency of the product. Peak locations vary with material dimensions and defect content and type, resulting in a smearing of multiple peaks into a single, broader peak present in commercial material. Thus greater consistency is evident in the material produced *via* the CTCC process by the G band separation (into G⁺ and G⁻). This separation is a result of the variation in the elastic vibrations of the crystal structure in the direction of the rod axis, and that of the vibration tangential to the tube circumference.

Secondly, a characteristic of all cylindrical structured fullerenes is the Radial Breathing Mode. The RBM feature of CNTs is still debated, with sources citing the feature is present but obscured in all samples, while others state it is present only in SWCNTs (36). Regardless, RBM features are a result of a phonon effect where all of the atoms comprising the cylindrical structure vibrate radially. The RBM feature is dependent on chirality, diameter, finite length effects, defects, inter-tube distance, and temperature (37). Thus, when interpreted in combination with other Raman features and analytical tools, the RBM feature can be used to determine chirality, and by consequence electronic conductivity, as well as diameters. However, great care must be taken when using the RBM feature to determine diameters and chiralities (38). If a distribution of tube diameters or chiralities is present, the peaks become broader. Additionally, if the tubes are bundled, then a dampening effect will be noticed (39). Figures 2.10 and 2.11 shows the spectral region for RBM vibrations for whisker and nanocluster materials using a 785nm excitation laser from the previous two images.

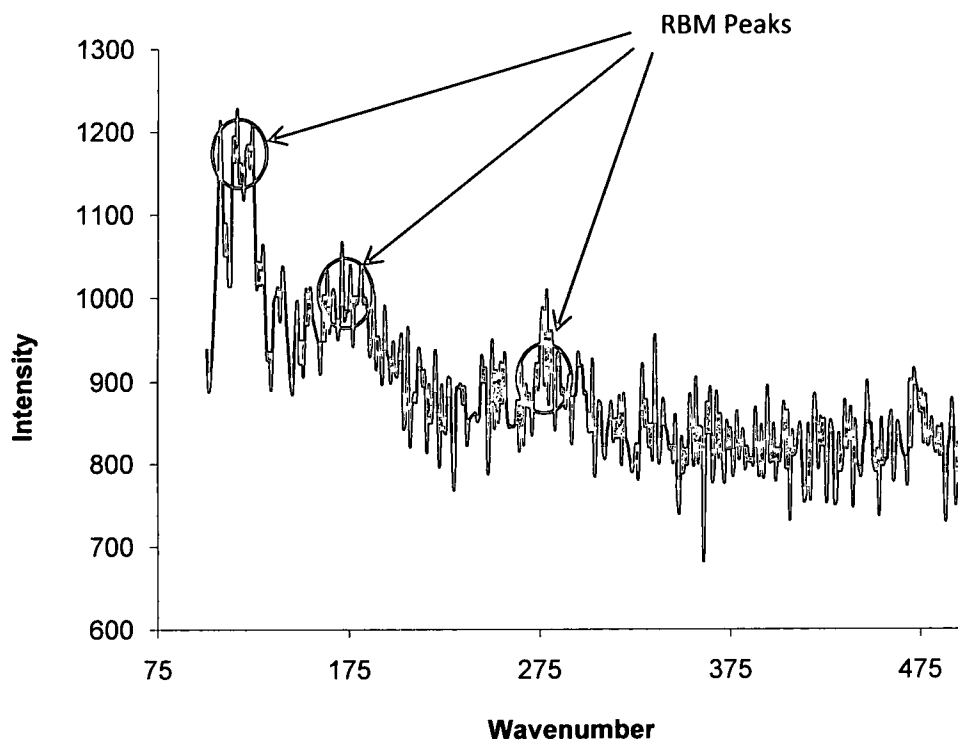


Figure 2.10. RBM Vibrations of SCNR Whiskers

Individual peaks are difficult to separate from the background due to low signal to noise, a result of a poor resonance condition. Figures A.28 and A.29 in the Appendix show a typical Raman spectrum of SCNRs in good resonance, distinctly showing the RBMs consistent with those shown in Figure 2.10. Figure 2.11 shows the analogous spectrum for nanoclusters.

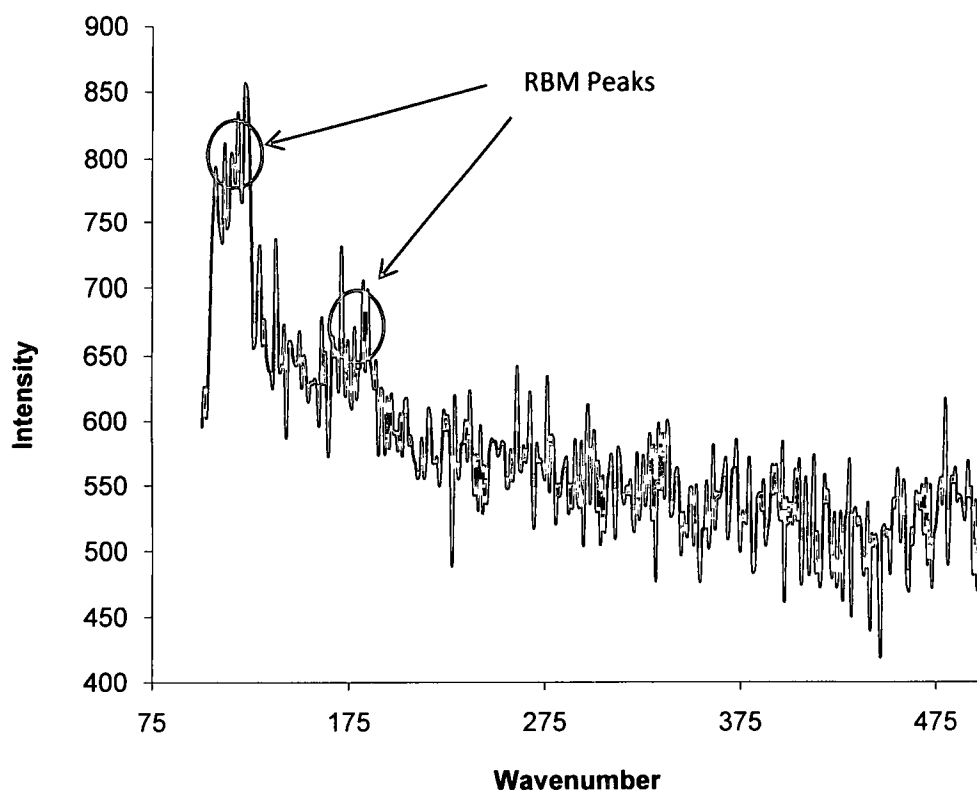


Figure 2.11. RBM Vibrations of SCNR Nanoclusters

Both materials exhibit RBM features between 110 and 200 cm^{-1} . The whisker product exhibits a low intensity peak at 175 cm^{-1} corresponding to a tube diameter of approximately 1.2nm (40). The larger feature located at approximately 115 cm^{-1} represents tube diameters of approximately 2nm. HRTEM images of these materials indicate that the tubes are roughly 0.4nm in diameter. The discrepancy seen is largely due to bundling of the tubes and finite tube lengths. The longer aspect ratio present in the whisker samples gives rise to a more intense RBM peak at 175nm.

As can be seen by comparing Raman spectra, CTCC produced material exhibits a more defined diameter range, while the MW-CNT samples, by virtue of the broader, smeared peaks indicate a larger distribution of diameters than the SCNR samples. This is typical of CVD produced CNTs, and MW-CNTs in particular.

Table 2.2 summarizes the Raman spectra, listing the main features examined with SW and MW-CNTs, and SCNRs. These include the disorder band, the so called “D” band, the in plane graphitic band, the so called “G” band and its splitting, and the G* and RBM bands. Splitting of the “G” band occurs on consistent cylindrical materials, such as SW-CNTs and SCNRs due to the two modes of stretching seen in the rolled graphite sheet, axial (along the cylinder or tube axis) and tangential (normal to the RBM stretching). Peaks are background corrected.

Material	Excitation	RBM		D		G(G-)		G+		G*	
		cm ⁻¹	cnts	cm ⁻¹	cnts	cm ⁻¹	cnts	cm ⁻¹	cnts	cm ⁻¹	cnts
Alfa MWCNT	514	NA	NA	1354	560	1583	632			2710	516
	785	NA	NA	1311	8609	1607	4916			2621	411
NanoLab MWCNT	514	NA	NA	1351	4481	1575	5544			2691	3750
	785	NA	NA	1312	6783	1600	5480			2608	675
SCNR NC	514	NA	NA	1354	64	1581	359			2698	483
	785	115	188	1312	6834	1581	4259	1612	3630	2621	1790
SCNR Whisker	514	NA	NA	1366	98	1581	764			2710	1162
	785	115	438	1313	4151	1580	8386	1611	3399	2617	6168

Table 2.2. Typical CNT and SCNR Raman Spectral Features

In general, peak shape and location illustrate consistency in the materials produced via CTCC over commercially available CVD produced MWCNTs. The G band splitting for SCNRs serves to demonstrate this consistency, above that of MWCNTs where the splitting is obscured due to variations in tube dimensions and chirality. While the G band is weakly dependent on tube diameter, the radial breathing mode is strongly dependent on diameter (33).

In summary, specific Raman features which define the SCNR nanostructure compositions of the CTCC process as compared to MW-CNTs are as follows: 1) very low D/G band intensity ratios (0.3 or less) compared to MWCNTs at 514nm excitation, 2) narrower G, D and G* bands compared to MWCNTs at 514nm and 785nm excitation, 3) Presence of RBMs at 785 nm excitation and 4) splitting of the G peak into G⁺ and G⁻ peaks at 785nm excitation.

2.4 Electron Microscopy

It is arguable that HRTEM enabled the discovery and subsequent characterization of nano materials in general and CNTs specifically. It is argued that the discovery of CNTs is incorrectly attributed to Iijima, *et al* in 1991, but should be attributed to the Russian scientists V. Radushkevich and V. M. Lukyanovich (41). The authors (Reference 40) go on to cite other prior examples of electron micrographs showing hollow structures of carbon in journal articles,

theses, and issued patents decades prior to 1991. The discovery of the allotrope aside, Iijima may certainly be cited as creating the scientific buzz currently seen in the scientific and engineering community. No doubt, HRTEM microscopy has played a significant role in the characterization and study of fullerene structures. HRTEM is not however, conclusive evidence of any particular characteristic or aspect of a CNT material. It does give verification or validation of a property or structure when used in conjunction with a more mathematically defined tool, such as Raman spectroscopy. It is in this light that a HRTEM study was performed on the material at Wright Patterson Air Force Base with the assistance of John Boeckl, Ph.D. (RXPS) and Craig E. Banks, Ph.D. of Manchester Metropolitan University.

With the structure of the material produced characterized via Raman spectroscopy, HRTEM was used to provide a less abstract picture of the material. Beyond providing a more visual concept of the material being investigated, the use of HRTEM imaging helps corroborate the conclusions drawn from Raman spectroscopy. For example, HRTEM is particularly useful in verifying the source of the D band in a particular sample of material as amorphous carbon is readily identifiable in HRTEM images as dark spots. Figure 2.12 shows a HRTEM image of SCNR Nanoclusters at low magnification. A sample of nanoclusters was dispersed in methanol (10mg/mL) and sonicated in a low intensity ultrasonic bath for 10min. A 50uL aliquot of the dispersion was pipetted onto a copper TEM grid and imaged at AFRL with the assistance of J. Boeckl.

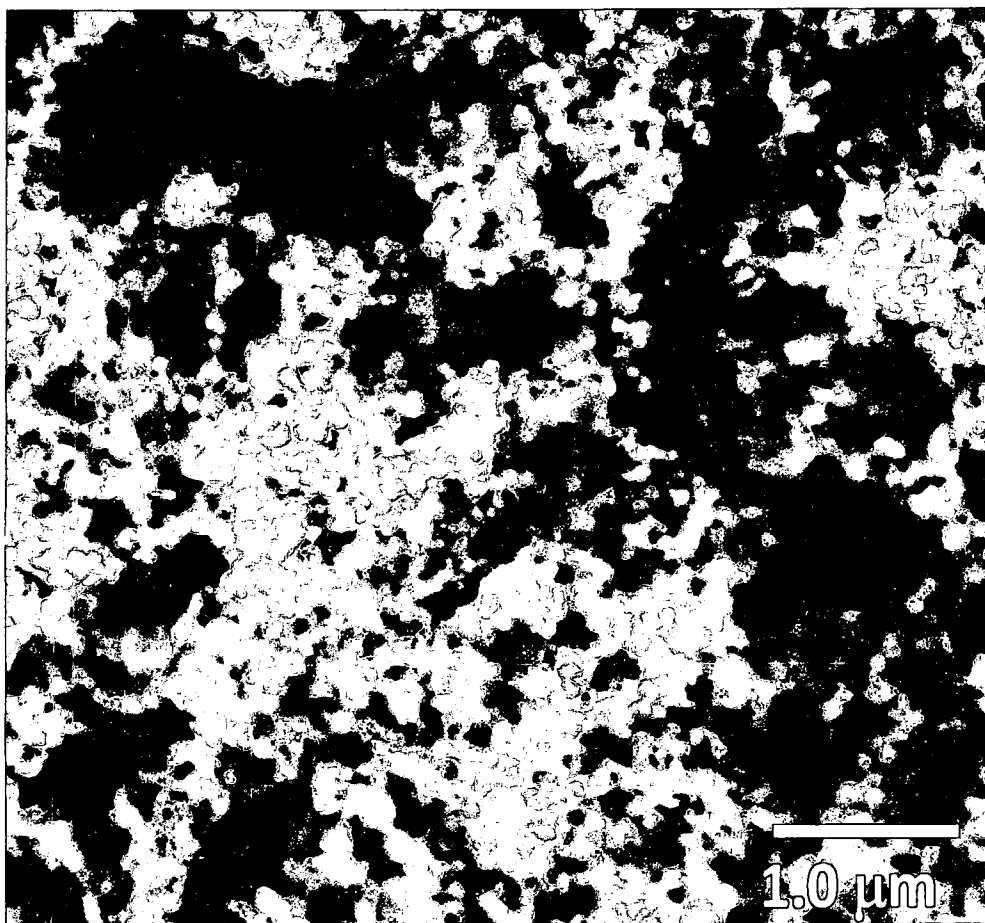


Figure 2.12. SEM Image of Bulk SCNR Nanoclusters
(Image Courtesy J. Boeckl)

This figure gives some insight into the potential utility of nanoclusters for use in high surface area applications. In Figure 2.13, a collection of individual nanoclusters can be seen. Each nanocluster is comprised of an irreducible, by physical means, network of SW-SCNRs and MW-SCNRs. Figure 2.13 shows the same material in Figure 2.12 at increased magnification. Resolution of the individual SCNRs is still not possible at this magnification, though insight is gained in the distribution of size of the individual SCNR clusters.

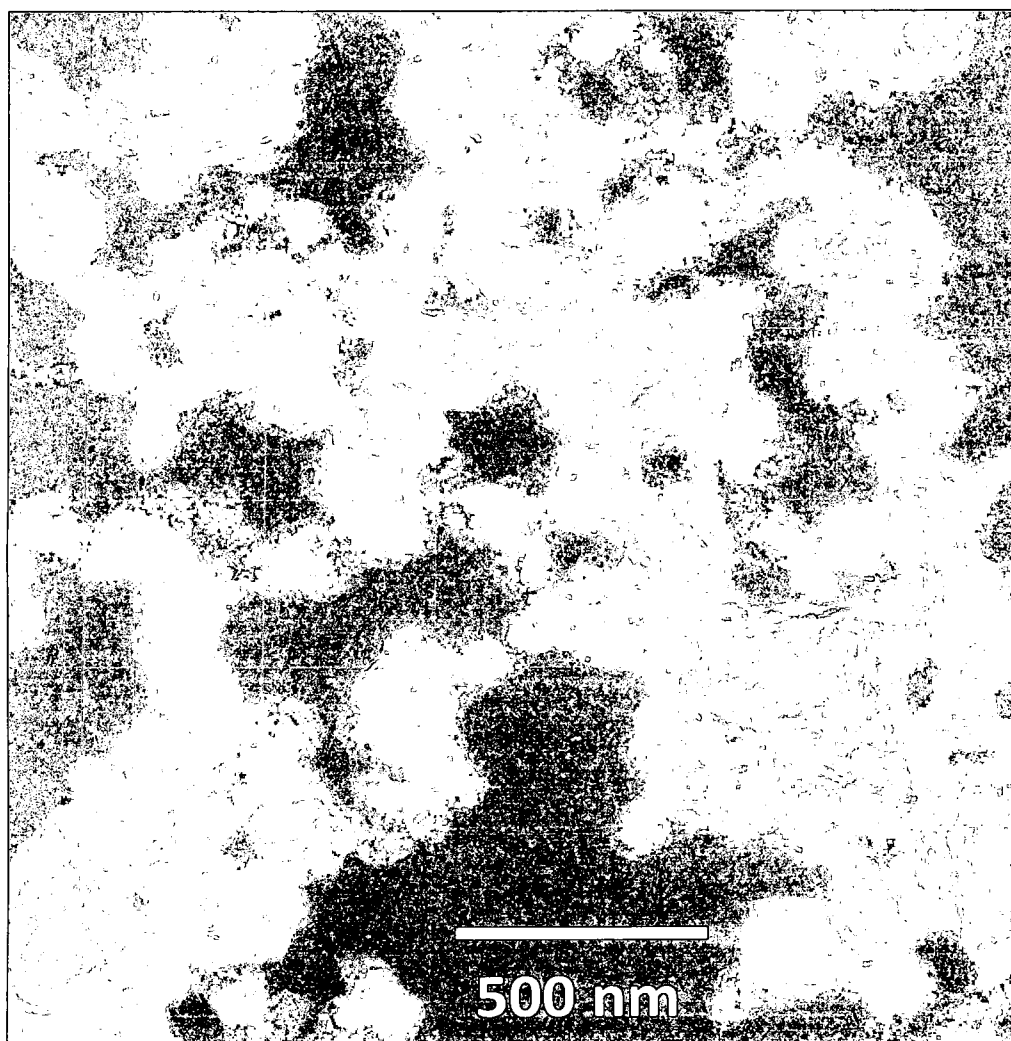


Figure 2.13 Medium Magnification HRTEM Image of Bulk SCNR Nanoclusters
(Image Courtesy J. Boeckl)

Further increasing magnification allows resolution of SW-SCNR bundles and MW-SCNRs. Figure 2.14 shows a pair of nanoclusters and the irreducible network of SCNRs that comprise them. A key feature to the electrochemical activity of CTCC produced material from polycrystalline reactant is visible at this magnification: the high degree of localized defect sites. These defects, or disorder in the π/sp^2 bonding, lead to increased edge plane character (discussed in greater

detail in Chapter 3), and are consistent with high D band intensities in the Raman spectra using a 785nm excitation source, as seen in Figure 2.8.



Figure 2.14. High Magnification HRTEM Image of Single SCNR Nanocluster
(Image Courtesy J. Boeckl)

Even at this magnification, it is difficult to definitively resolve the nanostructures predicted by the Raman spectra. To allow inspection of the SW-SCNRs and MW-SCNRs adequately, HRTEM is used to resolve the graphitic layering present in

the material. Figure 2.15 clearly shows the *ultra-small carbon nanotubes* (USCNTs) or SW-SCNRs individually and in bundles as labeled in the figure. The preceding images were obtained with the help of J. Boeckl (AFRL) with a JEOL 3000 HRTEM located at WPAFB AFRL. Figure 2.15 was obtained under the direction of Dr. C. E. Banks and has been published (42).

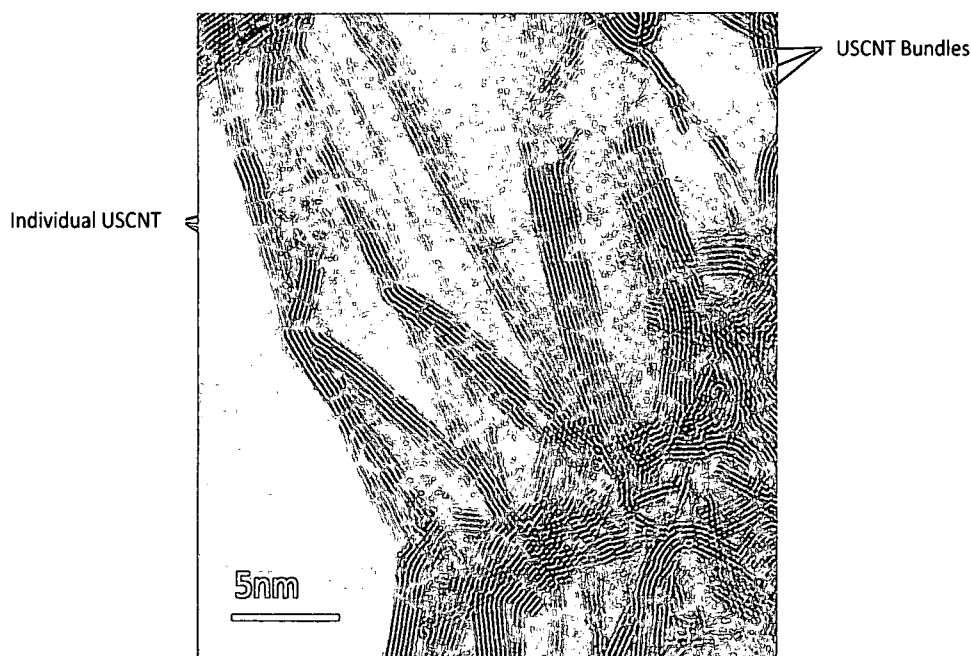


Figure 2.15. High Magnification HRTEM Image of Single SCNR Nanocluster
(Image Courtesy of C.E. Banks)

The preceding image, Figure 2.15, was obtained using the VGX900-W operating system. HRTEM micrographs were taken on a JEOL 3000FEG (TEM) instrument, which was equipped with an Oxford Instruments energy dispersive X-ray spectrometer with a super-atmospheric thin window (SATW). HRTEM imaging of materials produced via CTCC verify the structure and properties

predicted from Raman spectroscopy and the electrochemical behavior of the material as seen in Chapter 3. An additional HRTEM image of SCNR clusters is shown in the Appendix (Figure A.6), of a different production lot than shown above. Of key importance to the electrochemist is the high degree of disorder, mesoporous architecture, and purity as seen via electron microscopy. The small diameters and sharp bends of SW and MW-SCNRs seen in the images contribute directly to high edge plane character. A unique mesoporous structure is created by the high degree of kinks. This has interesting implications in terms of creating thin layer electrochemical behavior in bulk materials, which will be further discussed in Chapter 3. As an additional test of purity, no amorphous carbon or metallic impurities are seen in the images shown, thus verifying what is seen in ICP-MS and EDS investigation. These images support the conclusions drawn from the Raman study. The material has characteristically small diameter tubes present, typically tightly bundled, with a significant degree of bends.

2.5 Conclusions

The unique structure of the CTCC produced material was characterized *via* Raman spectroscopy, and structure and purity confirmed with HRTEM. The high intensity D band in the Raman spectra predicts electrochemistry behavior dominated by edge plane character. This provides justification for further investigation of the electrochemical behavior of the material for sensor, fuel cell, battery, and capacitor applications. The large defect ratios predict interesting electrochemical behavior. The features as predicted by Raman and verified by HRTEM indicate the material should exhibit very fast heterogeneous electron transfer rates, high electrochemical surface area, and potentially some thin layer behavior due to the mesoporous architecture. The tubes are much smaller in diameter than typical SWCNTs and MWCNTs, typically 0.4nm in diameter as determined by HRTEM. Furthermore, the material does not exhibit large degrees of metallic and amorphous carbon impurities typically found in commercial CNT samples.

CHAPTER 3.

ELECTROCHEMICAL BEHAVIOR

3.1 Introduction

Arguably, the greatest potential gains to be seen in a product utilizing carbon nanotube materials are electrochemical in nature. This encompasses batteries, fuel cells, sensors, and capacitors. Carbon is a uniquely interesting electrode material as it displays several advantageous properties. Carbon, in one form or another, displays a large electrochemical window in aqueous and many non-aqueous solvents. Additionally, due to the many allotropes present, it is possible to select a form that is particularly suited for the system to be studied. For example, lithium ions display good intercalation properties in soft carbons like graphite. Organics typically display better electrochemistry at hard carbons, such as glassy carbon or diamond (43). It is, however, this field that best illustrates the shortcomings of current CNT production technology. Metal catalyst impurities lead to significant background currents, transient electrode behavior, and falsely identified electrocatalytic properties (44). Carbon nanotubes are interesting electrochemically for several reasons: high electrical conductivity, chemical stability, thermal conductivity, and chemical activity. The nature of

CNT's electrical/thermal conductivity and mechanical properties has been well studied and documented in the literature (45) (46). A great deal of the conductivity seen in CNTs stems from the lack of crystal defects. As described earlier, the chemical and electrochemical activity of fullerenes are a result of the cylindrical structure, resulting in π bond disruptions and strained pyramidization. Also, as mentioned previously, intensity of the D band observed in the Raman spectrum using a 785nm excitation laser is indicative of edge plane character of fullerene materials (38).

The most appropriate comparison of conventional carbon electrode material to CNTs is with Highly Ordered Pyrolytic Graphite (HOPG). This is due to the separation of basal plane character and edge plane character. Three dimensional graphite displays distinctly different electrical, thermal and electrochemical properties normal (basal plane) and orthogonal (edge plane) to the "stacked sheets." This is best seen in HOPG which displays distinctly better electron transfer properties at the edge plane in comparison with the basal plane (47). In fact, some authors have stated that CNTs and MWCNTs in particular are only electrochemically active at edge plane-like sites, such as open ends of MWCNTs (7). Recent work has shown that electrodes modified with carbon nanotubes display increased signal-to-noise ratios and reduced overpotential for a number of different analytes (48). Additionally, CNTs have been widely recognized as providing extremely fast electron transfer rates for a number of different redox couples (49). Banks, *et al* convincingly argue that the most ideal electrochemical behavior that may be seen from carbon nanotubes and their like

structures is that of edge plane HOPG, but fullerenes offer significantly higher surface area than HOPG due to smaller particle size.

Post production purification steps are currently considered vital to the electrochemical use of CNTs, regardless of source. However, it has been shown that purification steps typically lead to changes in the properties of material (50). It has also been shown that neither sonication nor acid digestion has an affect on the electrochemical activity of CVD grown CNTs (51). Some authors have indicated perfect purification of SWCNTs using a combination of oxidation of non- nanotube carbon and iron catalyst, followed by acid digestion (52). These techniques have not proven to be as effective with MWCNTs due to catalyst shielding by the nanotube structure and there is even disagreement in the literature on the effectiveness with SWCNTs (31).

Thus, three electrode formats were studied: paste, basal plane HOPG modified with SCNRs, and SCNR arrays grown on open cell foam. Each type of electrode was tested in quadruplicate, with each electrode fabricated using material of a different production lot. The three types of electrodes represent a cross section of common electrode types with applications ranging from chemical and biological sensing to analytical/kinetic investigations to power generation and storage.

3.2. Experimental Setup

3.2.1 Instrumentation

3.2.1.1 Carbon Paste and Open Cell Foam

Carbon paste and SCNR modified open cell foam electrodes were investigated using a Gamry (Warminster, PA) Reference 600 Potentiostat/Galvanostat/ZRA/Frequency Analyzer, calibrated using the supplied calibration cell prior to use. All paste electrode experiments were conducted using a Gamry Doctor Bob's Small Volume Electrochemical Cell. Cell volume was 30mL for all experiments. A BAS (Lafayette, IN) MW-1033 platinum wire electrode was used for a counter electrode. Solutions were degassed via 15min 99.9% pure argon gas purge (AGA Gas, Dayton, OH) prior to experiments.

3.2.1.2 Immobilized Nanomaterial

Electrochemical experiments were performed using a *i*-Autolab type III potentiostat (Eco-Chemie, Utrecht, The Netherlands) controlled by General Purpose Electrochemical Systems v.4.7 software. For all electrochemical experiments carried out with immobilized CNTs or SCNRs, the working electrode used was a basal plane pyrolytic graphite electrode (4.9 mm diameter, Le Carbone, Ltd., Sussex, U.K.). The counter electrode was a bright platinum wire

with a large surface area, and a saturated calomel reference electrode completed the circuit. This portion of the experimental section was partially taken from (53), of which Bill Riehl is a co-author, published in *Langmuir* 2007. These experiments were conducted in Dr. Craig E. Banks' laboratory at Nottingham-Trent University, U.K (hydrazine oxidation) as well as at Riehl Engineering, Ltd in Dayton, Ohio (all other experiments).

3.2.2 Chemicals Used

All chemicals were purchased from Aldrich, obtained at the highest grade available, and used directly without further purification. All experiments were carried out at room temperature, and otherwise uncontrolled for temperature. Aqueous electrolyte solutions were prepared with KCl (99.5%, Aldrich) or KNO₃ (99.5%, Aldrich) using ultrapure water from a Vivendi UHQ grade water system (Vivendi, U.K.) for U.K. experiments or Thermo Scientific Barnstead NANOpure Water Purification System for U.S. experiments. Water exhibited resistivity of not less than 18.2 MΩcm⁻¹. All solutions were degassed with oxygen-free nitrogen (BOC Gases, Guildford, Surrey, U.K.) for U.K. experiments or oxygen free argon (AGA Gases, Dayton, OH) for U.S. experiments.

3.3 Electrode Overview

Three forms of nano carbon electrodes were investigated: MWCNT and SCNR paste electrodes, SCNR modified open cell foam electrodes, and MWCNT and SCNR modified basal plane HOPG electrodes. A graphite paste electrode was also included as a benchmark for paste electrode performance. Carbon paste electrodes were studied due to the applicability of the design to chemical sensors, with potential application to measuring a wide range of analytes including: cysteine, NADH, dopamine, and ascorbic acid (51) (54) (47). The SCNR – HOPG electrode was studied to determine electrochemical purity of the material as well as to reduce thin layer effects of the electrode seen in paste electrodes. The SCNR modified, open cell foam electrode was studied to provide initial insight into the behavior of the electrode with an appropriate geometry for fuel cell/biofuel cell and ultracapacitor applications.

3.3.1 Carbon Paste Electrodes

Carbon Paste (CP) electrodes, most commonly using conductive graphite as the carbon material, are popular for electrochemical sensor applications. The electrode most typically incorporates two phases: conductive carbon and a pasting liquid, often mineral oil. Perhaps the most well known and widest use of CP electrodes is with home blood-glucose test strips. CP electrodes have several important advantages over other macroscopic electrode designs, including simple

fabrication and renewable surface. Fabrication is of lesser importance than the ease of surface renewal. Electrodes often become fouled with biological contaminants or chemical/electrochemical byproducts. The CP electrode surface may be quickly and easily renewed by scraping or wiping the electrode surface clean with no other action necessary. The ease of fabrication can also be extended into the production of admixtures of electrode materials for selectivity, sensitivity or for economic reasons. Improved selectivity may be accomplished through the incorporation of enzymes, antibodies or other nanophase materials into the bulk electrode composite. Sensitivity of an electrode may often be increased through modification of the bulk electrode with secondary phases, such as boron doped diamond, or carbon nanotubes (51). Additionally, less expensive materials may be incorporated into paste electrodes as fillers where appropriate. There are distinct disadvantages for the CP electrode, including variability in fabrication, and dependence on the user's experience in producing electrodes.

Paste electrodes were prepared by milling CNTs and SCNRs in mineral oil (Aldrich) at 50 wt%. Carbon paste electrode material was obtained from Bioanalytical System (West Lafayette, IN), and consisted of graphite dispersed in paraffin. A BAS carbon paste electrode holder, MF-2010, was used for all paste electrode builds. Milled paste material was tamped into the electrode holder and compressed using a glass microscope slide and scraped level with the slides edge. In each experiment, a BAS MW-4130 Pt wire 6.5cm in length counter electrode was used. A Gamry Double Junction Ag/AgCl reference electrode was used for all measurements.

3.3.2 Immobilized Nanomaterial Electrodes

Immobilized CNT/SCNR electrodes have been used effectively to accurately study the electron transfer kinetics of CNTs and SCNRs (7). Basal plane HOPG has the advantage of providing a robust platform for electrically addressing a monolayer of nanomaterial at the surface of a nearly inert electrode material. This allows the study of the nanomaterial directly, without interference from the macro-electrode, as is the case when using glassy carbon (55).

The process for modifying basal plane HOPG with CNTs or SCNRs was taken from (54). Research Grade MWCNTs, produced via catalytic CVD, were purchased from NanoLab (Brighton, MA), advertised as >95% purity, 10-20nm in diameter, and 5-20um in length. SCNRs were produced via CTCC as described previously in Chapter 1. CNTs or SCNRs are gently rubbed onto the clean basal plane via clean, fine filter paper (56). Electrodes used for hydrazine detection were fabricated and tested in Dr. Banks laboratory at Manchester Metropolitan University, UK and Oxford University, UK. Electrodes used for ferricyanide detection were fabricated and tested at Riehl Engineering in the US.

3.3.3 Open Cell Foam Electrodes

CNT arrays on open cell foam electrodes were produced to serve as an enhanced surface area electrode for fuel cell, battery, and capacitor systems. To the best of the author's knowledge, this is the first example of such an electrode

system tested, and illustrates a key advantage of the CTCC process. Until now, there were no effective means discussed in the literature for the production of CNTs on the surface of a current collector for electrochemical applications. All previous technology required the use of transition metal catalysts for the production of CNTs, and subsequent attachment of the nanostructure to the current collector. A previous example of CVD produced CNTs on a typical electrode material used Fe catalyzed production of CNTs on a planar Pt surface. It is extremely difficult to create an adherent film of CNTs on the surface of a current collector that is electrochemically robust and inert due to the inherent limitations of CVD growth. The catalyst used in CNT growth *via* CVD also serves as the attachment point for the CNT to the substrate, and thus is an electrochemically unstable substrate. SiC is an ideal substrate for such studies as it does not play a role in most common electrochemical processes. Thus, stable carbon nanotubes or nanotube derivatives may be produced that are electrically and mechanically attached to the current collector exhibiting clean, definable and repeatable electrochemical behavior.

Samples of Erg Aerospace (Oakland, CA) 100ppi Duo Cell SiC coated reticulated vitreous carbon foam were purchased. The foam was then processed *via* CTCC resulting in the growth of a thin layer of SCNRs at the surface of the SiC, as shown in Figure 1.7. The foam sample was then sliced with a diamond dicing saw as described in Example 3. According to ERG literature, 45ppi foam has a surface area of approximately 2000 ft² per cubic foot of foam (or approximately 6500m² per cubic meter). Thus individual foam samples have an

approximate geometric surface area of 328mm^2 . Electrical contact to the electrode was made via 24ga solid copper wire bonded to the electrode with EpoTek (Billerica, MA) H77 Graphite Conductive Epoxy. The electrodes were then encapsulated in 0.25in diameter polypropylene tubes with Hexion (Ashland, CA) EPON862/EPICURE8230 2 part epoxy (100:32 mix ratio by weight) with 10mm of the electrode un-potted. The epoxy was allowed to gel overnight and post baked for 24hrs at 90C to ensure complete polymerization. Figure 3.1 shows an encapsulated SCNR modified foam electrode used in this work.

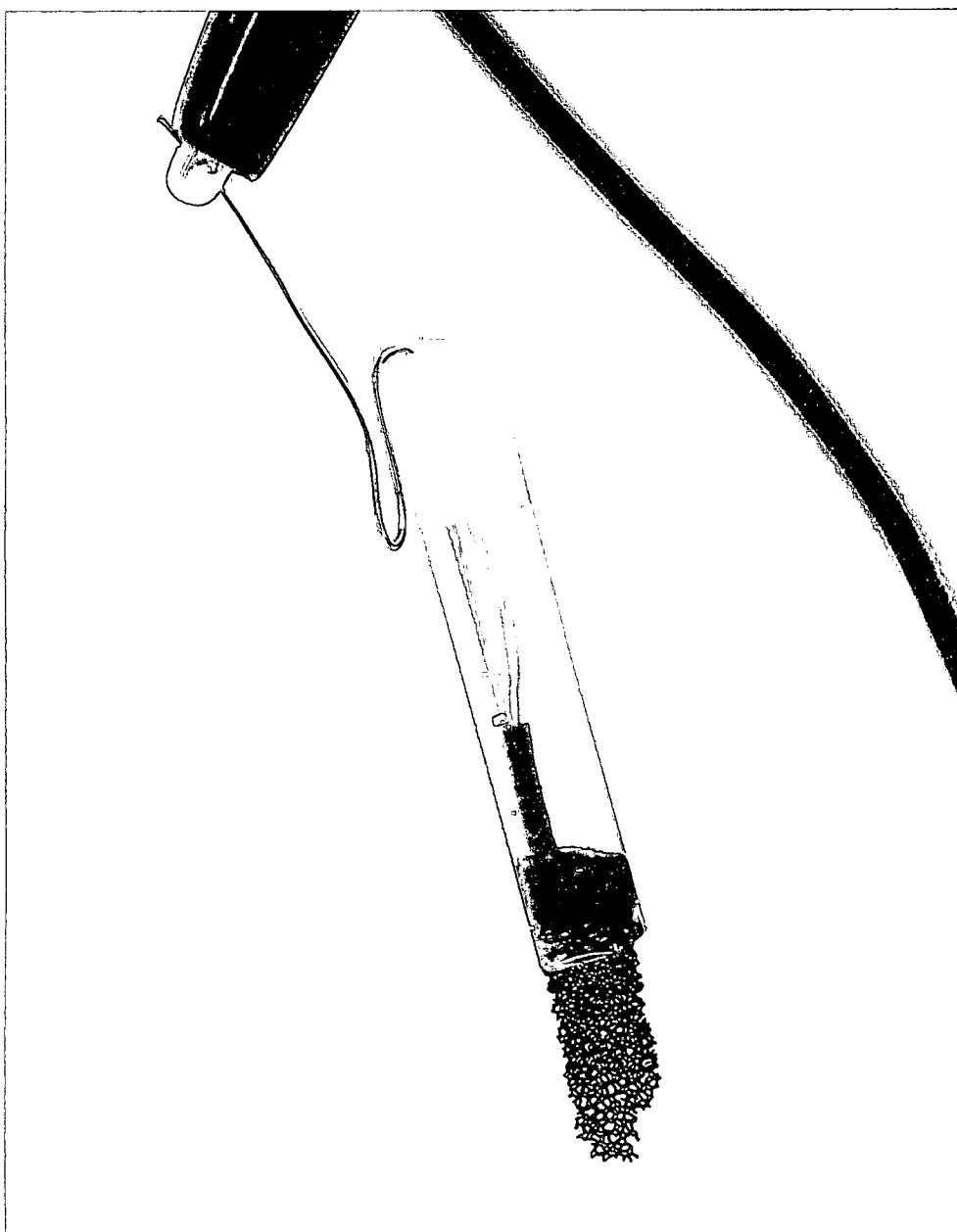


Figure 3.1. SCNR Modified Open Cell Foam Electrode

3.4 Electrochemical Behavior

Two classical electrochemical techniques were used to characterize the behavior of various nanocarbon electrode forms. Cyclic Voltammetry (CV) is one of the most useful tools at the disposal of the electrochemist. CVs are rich with qualitative and quantitative information about the electrochemical system being studied. Therefore, it is only appropriate that the initial characterization of the novel structures produced in this work be studied with this technique. In cyclic voltammetry a triangular potential wave form is applied and both current and voltage followed, with current plotted along the Y axis and applied voltage along the X axis. Chronocoulometry (CC) was used to further investigate the foam electrodes. Chronocoulometry is a large potential step experiment where the charge transferred to/from an electrode is recorded as a function of time.

3.4.1 Paste Electrode Behavior

It is useful to compare the background current of an electrode with well defined or standard electrode materials. This can be seen in Figure 3.2 and Figure 3.3 which show typical background scans done using cyclic voltammetry on electrodes fabricated with commercially available carbon paste electrodes (BAS Inc, MF-2010/CF-1010), and nanocarbon paste electrodes made by milling MWCNTs and SCNR nanoclusters, respectively, into mineral oil at 50wt%. Electrodes were immersed in a 1.0M KNO_3 aqueous solution and cyclic

voltammetry performed using a scan rate of 100mV / sec. Figure 3.2 shows both the first and second scans performed on the paste electrodes and allows a comparison of the background currents obtained.

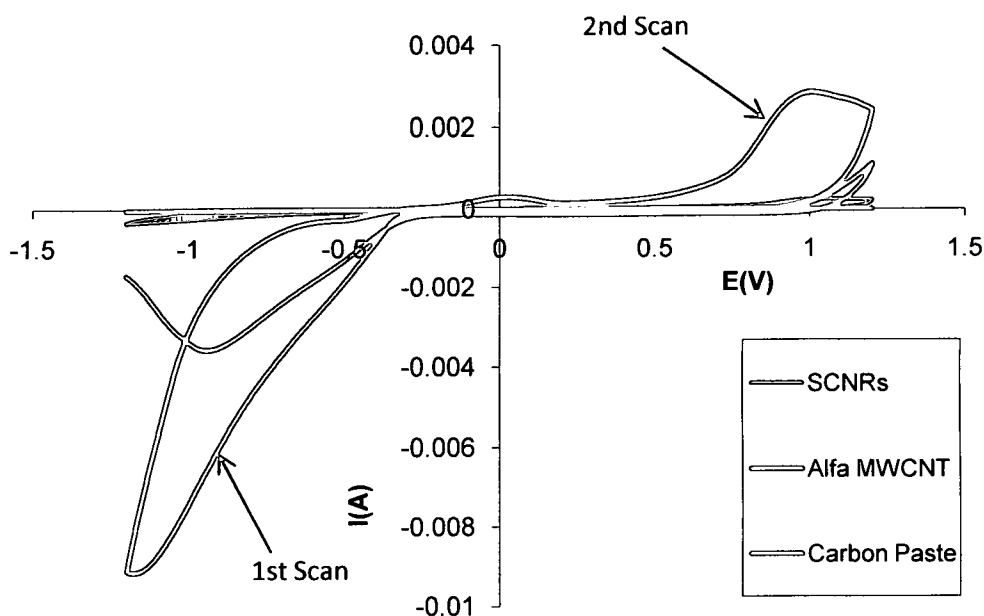


Figure 3.2. Background CV Scans on Various Carbon Paste Electrode Materials

The background current of MWCNTs is much greater on the first scan than the second and continues to decay for several scans thereafter. Figure 3.3 shows the data presented in Figure 3.2 using an altered scale to allow comparison of the three electrode materials without scale compression due to the oxidation-reduction processes dominating the voltamograms at potential extremes.

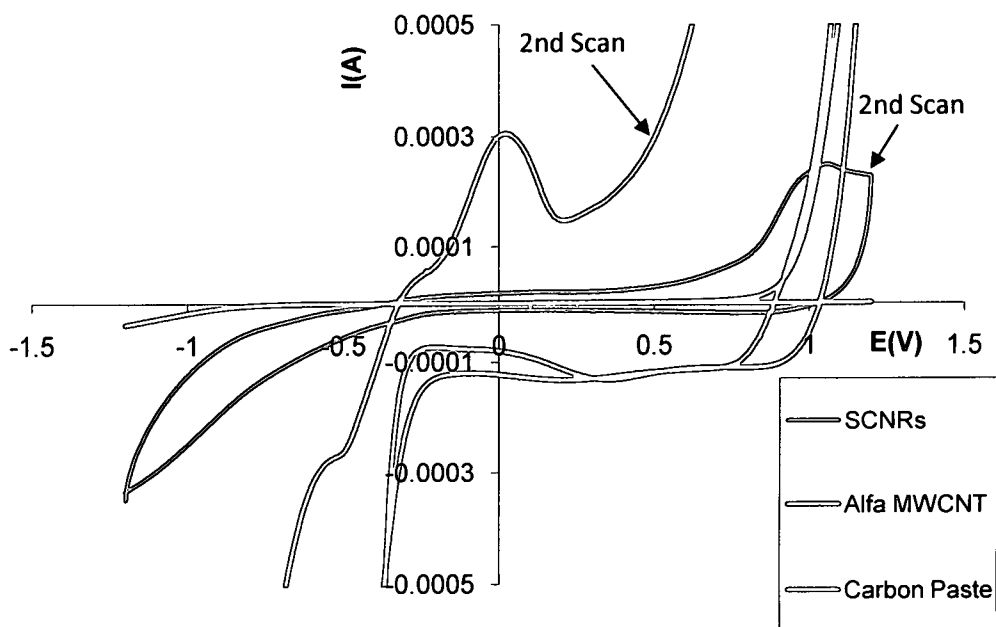


Figure 3.3. Background Current Comparison of Paste Electrodes Using Expanded Scale

The oxidation currents for the paste electrode begins to increase at roughly 0.75V, as expected, for all of the carbon electrode materials. This is likely due to progressive oxidation of the electrode *via* electrochemical reaction (57). Regardless of the number of scans the background currents of MWCNTs remain elevated compared to the electrode containing CTCC nanocarbon (SCNRs) which has background currents more comparable to the low background currents seen on commercially available carbon paste electrodes. At 0.5V vs. the reference during the oxidation scan, the MWCNT has a background current of 290 μ A, the SCNR 1.25 μ A, and the BAS 22nA. Figure 3.4 shows the background current of the carbon paste electrode separately. The carbon paste shows a lower background current than either carbon nanotube paste electrode.

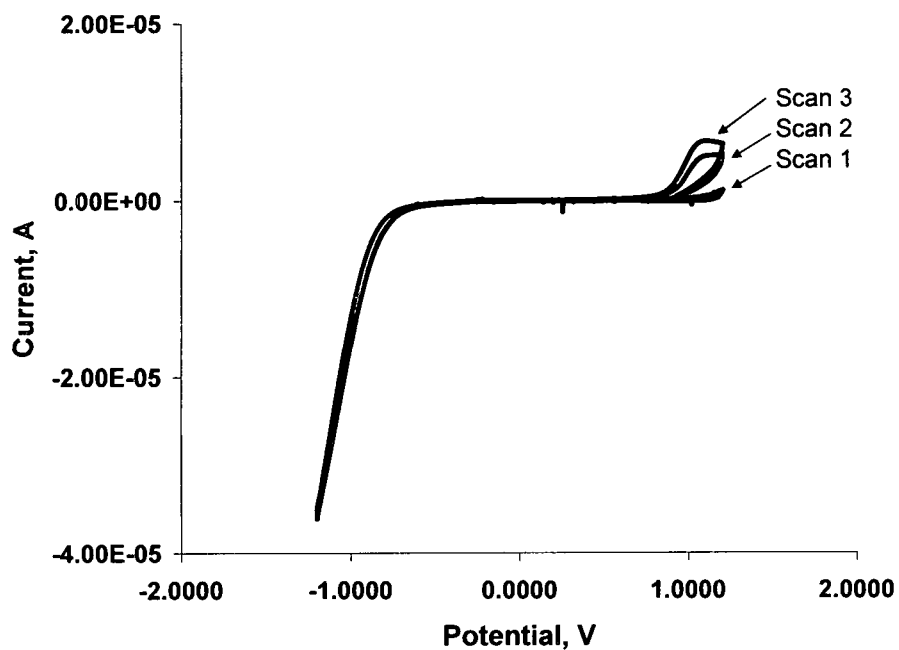


Figure 3.4. Background CVs of BAS Carbon Paste Electrode

Oxidation current increases with repeated scans due to oxidation of the edge plane carbon. To illustrate the detrimental effect of metal catalyst impurities on an electrode, the background scan of commercial (Alfa Aesar, 44945) MWCNTs advertised as 95% pure, is shown in Figure 3.5.

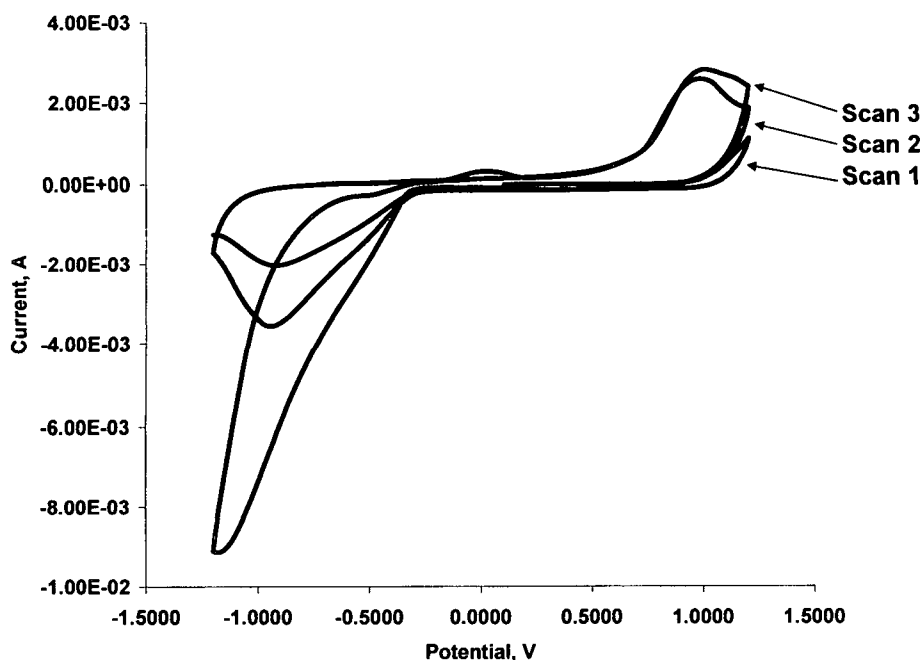


Figure 3.5. Background CVs of MWCNT Paste Electrode

Of key interest in this figure is the transient behavior of the electrode with successive scans. Electrodes that display transient behavior are not well suited for electrochemical applications. Transient behavior is typically difficult to characterize and account for in a wide range of conditions. This figure indicates, after the first 3 scans, that the potential window of the electrode is roughly -450mV to 750mV vs Ag/AgCl reference electrode (BAS Inc, RE-6). For comparison, a CTCC nanocarbon paste electrode identical to the commercial MWCNT electrode is shown in Figure 3.6.

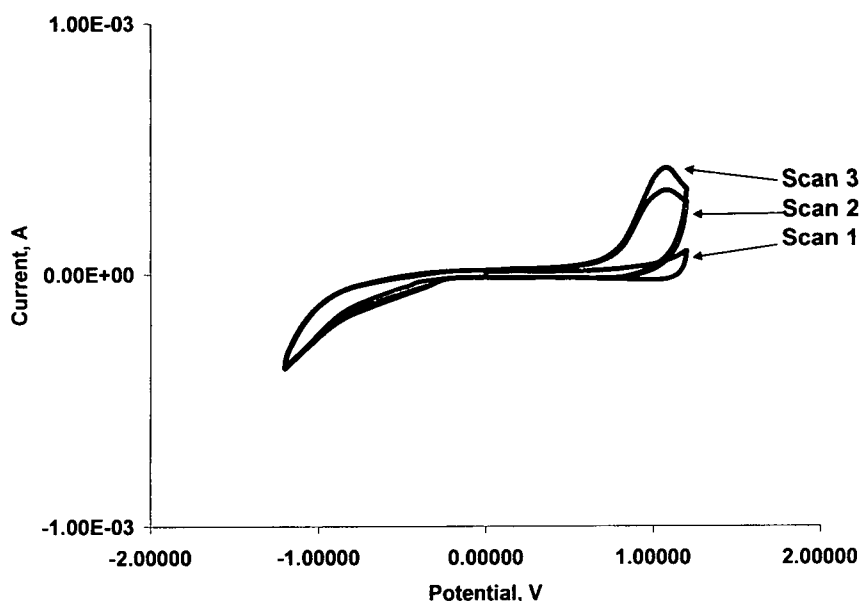


Figure 3.6. Background CVs of SCNR Paste Electrode

The CTCC-SCNR paste electrode displays significantly more stable background, with no transient behavior seen below 750mV vs Ag/AgCl because no metal catalyst is present. This is an improvement over conventional CVD grown CNT materials. Aside from increased background currents, purified and stabilized CVD grown CNTs lead to significant electrochemical issues not seen with CTCC grown materials as even extensive washing procedures cannot fully remove all traces of active metal contamination.

A comparison of the electrochemical performance of the paste electrodes with a model redox couple is now in order. The ferricyanide-ferrocyanide couple was chosen because of its nearly reversible behavior on edge plane HOPG. Figure

3.7 shows the response to 1mM $K_3Fe(CN)_6$ of the BAS carbon paste electrode in deaerated 1M KNO_3 .

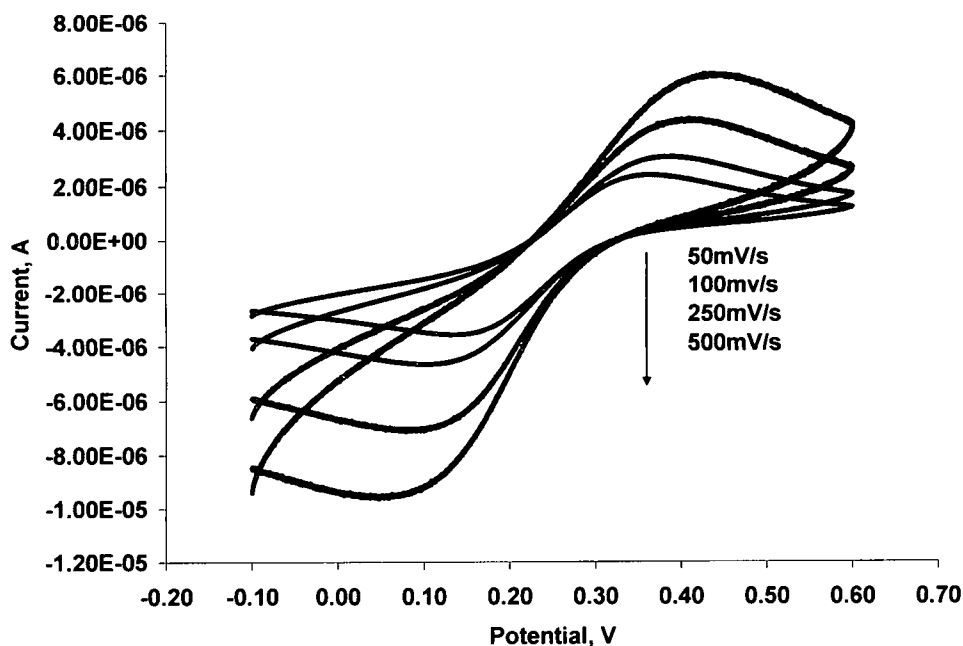


Figure 3.7. Cyclic Voltammograms of 1mM Ferricyanide at Carbon Paste Electrode

The ferricyanide-ferrocyanide couple displays definite irreversible electrochemistry at the carbon paste electrode, as indicated by peak to peak separations greater than 200mV for slower scan rates. This is due to blending of edge plane character and basal plane character in the finite grains of graphite used. In contrast to this behavior, Figure 3.8 shows the response of the same couple under the same conditions at a MWCNT paste electrode.

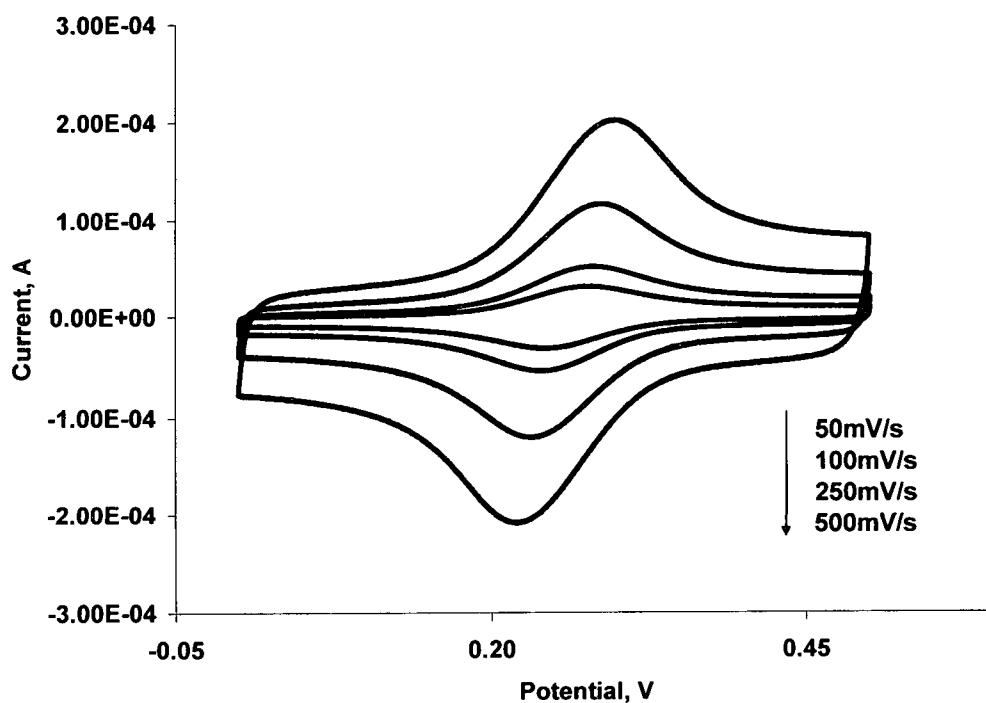


Figure 3.8. Cyclic Voltammograms of 1mM Ferricyanide at MWCNT Paste Electrode

The nanocarbon electrode exhibits much more ideal behavior even at fast scan rates of several hundred millivolts per second. This acts as further evidence of the intrinsic properties that attract researchers to their use. Figure 3.9 shows the identical experiment using CTCC nanocarbon.

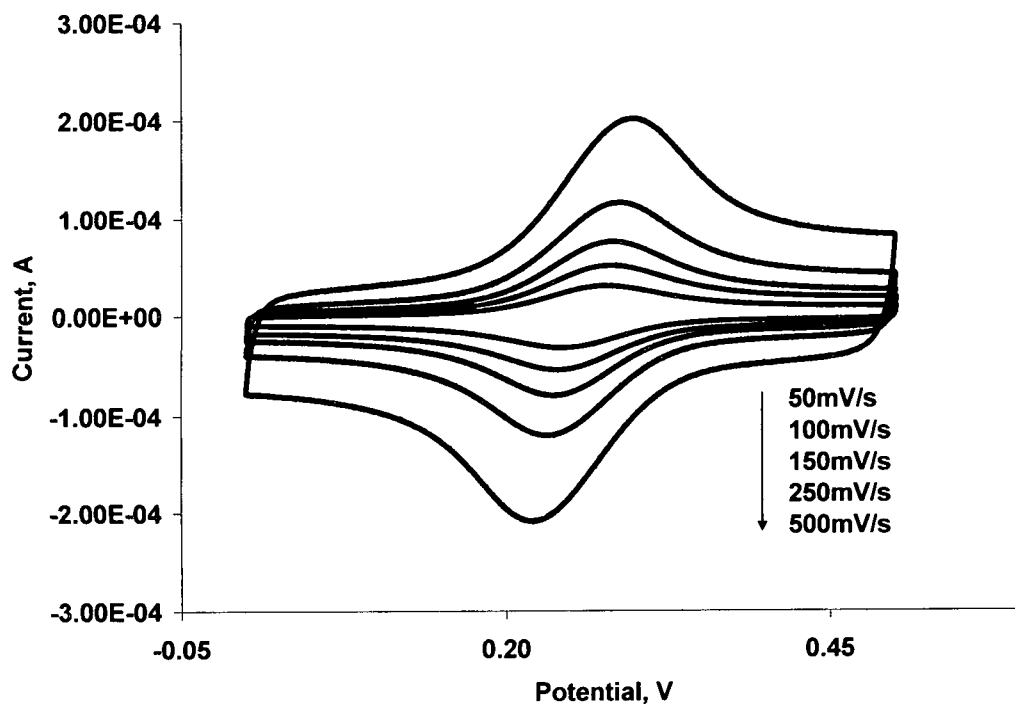


Figure 3.9. Cyclic Voltammograms of 1mM Ferricyanide at SCNR Paste Electrode

Figures 3.7 through 3.9 illustrate key properties of the bulk material produced via CTCC. At moderate scan rates, below 100mV/s, the MWCNT and SCNR paste electrodes exhibit lower than Nerstian peak separations, as would be expected in a thin layer cell. Figure 3.10 shows a plot of peak separations for both commercial MWCNTs and CTCC nanocarbon paste electrodes, taken from Figures 3.8 and 3.9.

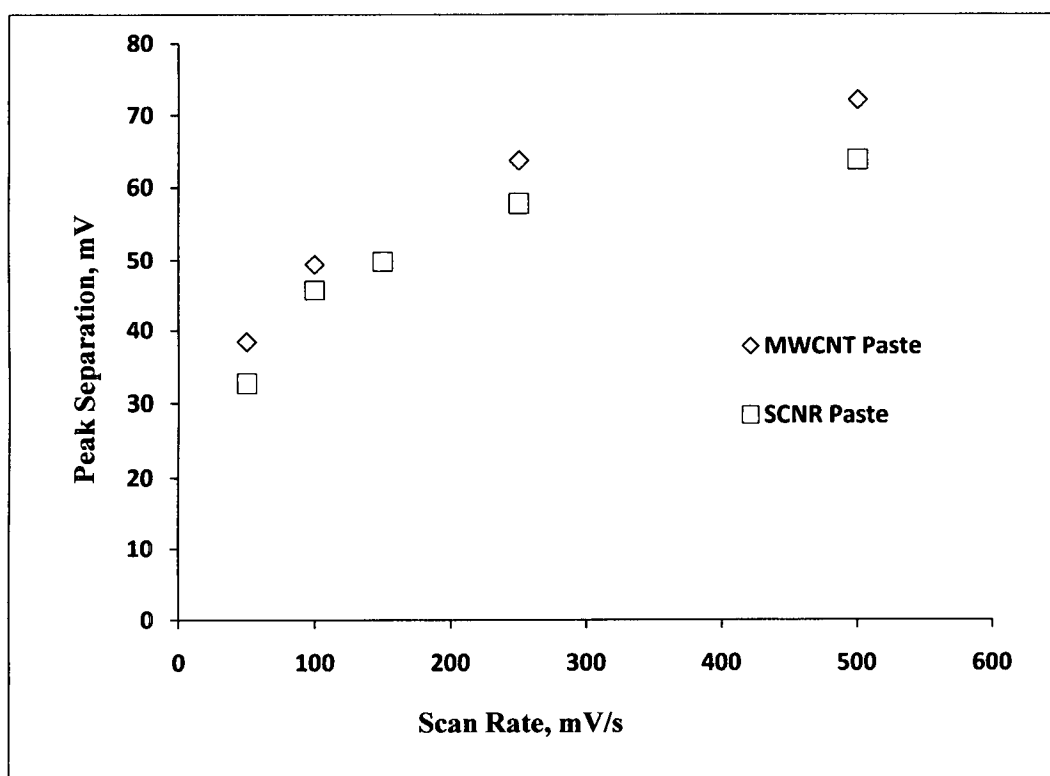


Figure 3.10. Peak Separation of Nanostructured Paste Electrodes

Lower than Nerstain peak separations were observed at scan rates slower than 250mV/s. This is due to the mesoporous architecture seen in the nanocarbon samples. Porosity resulting from imperfection in paste preparation for both the MWCNT paste and SCNR pastes likely also leads to a thin layer cell effect. Analyte, in this instance ferricyanide, becomes effectively trapped in the porous structure created by the carbon and carbon-binder interfaces. This phenomena prevents a normal concentration dependent diffusion profile from developing, thus yielding peak separations less then 58mV for single electron couples (58). Results on replicate SCNR paste electrodes, shown in the Appendix (Figures A.11 through A.14), display variations in performance, which are an inherent limitation of paste electrodes. To better study the SCNRs as electrode materials,

immobilized SCNRs on basal plane highly ordered pyrolytic graphite are characterized in the following section.

3.4.2 Immobilized Nanomaterial Behavior

Carbon nanotubes are often attributed with electrocatalytic properties, most frequently with hydrogen peroxide (7) (2). In order to demonstrate that significant residual catalyst is present in commercial CNT samples, HOPG immobilized electrodes were fabricated. It is known that hydrazine is electrochemically active at metal surfaces, but not on carbon due to large overpotential (59). Thus, it provides an ideal electrochemical probe to determine the presence of residual metal contamination. Figure 3.11 illustrates the fact that the presence of the metal impurities in commercially available MW-CNTs can grossly affect electrochemical behavior when such materials are incorporated into electrodes, and is included, as published, with permission of Dr. Banks.

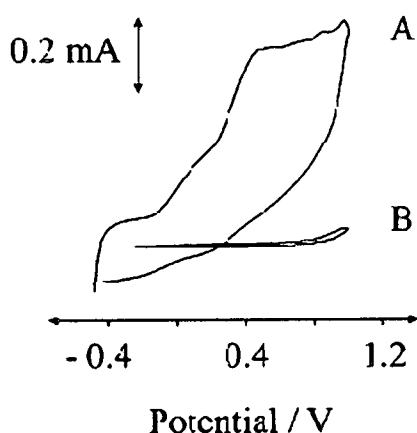


Figure 3.11 Cyclic Voltammogram of MWCNTs (A) and SCNR Nanoclusters (B) in the Presence of 1mM Hydrazine, Second Scan Shown (Image from *Langmuir*, 2007)

Electrodes were prepared by immobilizing the carbon nanomaterial under test on a basal plane graphite electrode (42). The basal plane graphite substrate by itself generally displays slow heterogeneous electron transfer rates when species present in the solution are probed, thus providing an ideal immobilization platform for nanomaterials (7). CV scans (1mV/sec) were done in pH 7.1 phosphate buffer which contained 1mM hydrazine, shown in Figure 3.11. This electrochemical probe (hydrazine) is highly sensitive to metallic impurities, since it can only be oxidized at a metal containing electrode and not on a pure carbon electrode. The presence of a large electrochemical oxidation wave at about +460mV (vs. SCE), confirms the presence of metal impurities in the electrode fabricated using commercially available MW-CNTs (NanoLab) and its absence in the scan on the electrode containing SCNRs clusters confirms the absence of metal impurities in these materials.

Figure 3.12 shows the effect of increasing SCNR cluster loadings on the cyclic voltamograms of ferricyanide at the modified HOPG. The response of the electrodes in a 4mM potassium ferricyanide / 1M KNO₃ solution was evaluated varying the amount of clusters used.

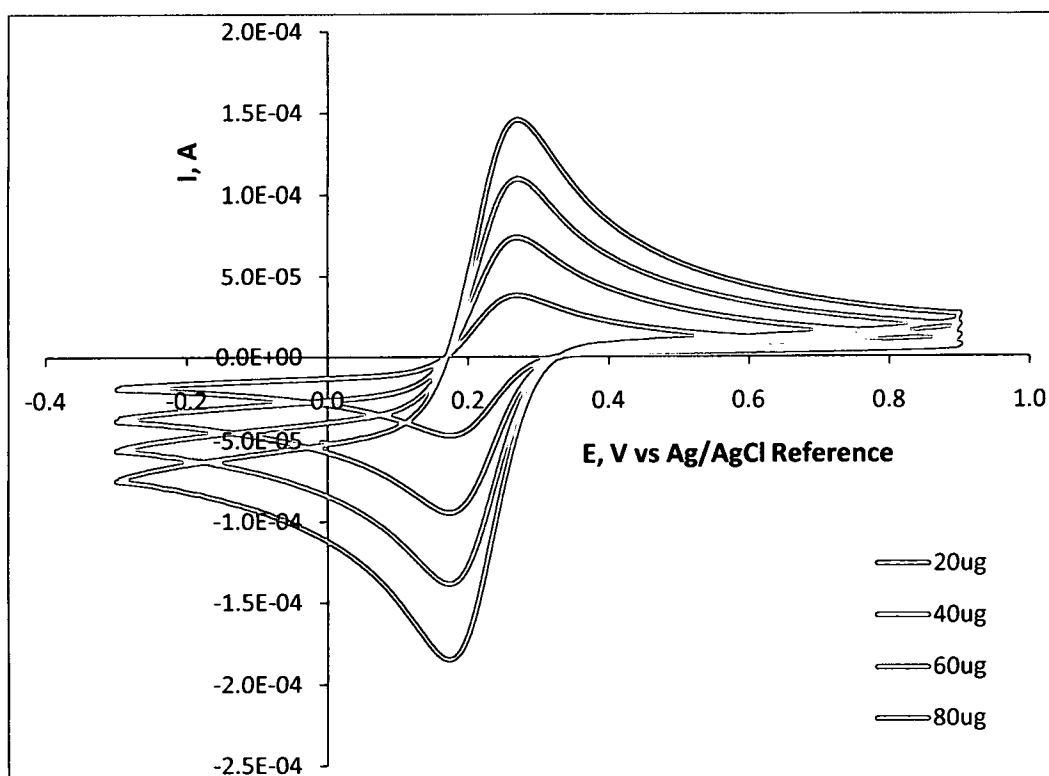


Figure 3.12. Cyclic Voltammograms of Ferricyanide on an Electrode Fabricated with Increasing SCNR Loading at 10mV/s Scan Rate

Ferri-ferricyanide is a model redox couple which is commonly used to judge electrode performance. Curves result from increasing amounts, 20-80 micrograms in 20 microgram increments, of SCNR clusters immobilized on the basal plane pyrolytic graphite surface. Figure 3.12 shows that the electrochemical response of the electrode is dominated by the SCNRs and not the basal plane HOPG.

To show the electrochemical consistency of the material produced *via* the CTCC process, multiple cluster modified HOPG electrodes were fabricated. The same HOPG platform was used in each experiment, polished and cleaned between experiments as outlined earlier. 80ug of clusters were deposited as before onto the surface. Three electrodes were made using clusters made from a different lot of

SiC material. Figure 3.13 shows cyclic voltamograms of 4mM ferricyanide/1M KCl solution at the SCNR modified HOPG electrodes. Consistent with electrochemical theory, the potential difference measured between the oxidation and reduction peaks (ΔE_p) should be 58mVs for a reversible single electron redox couple.

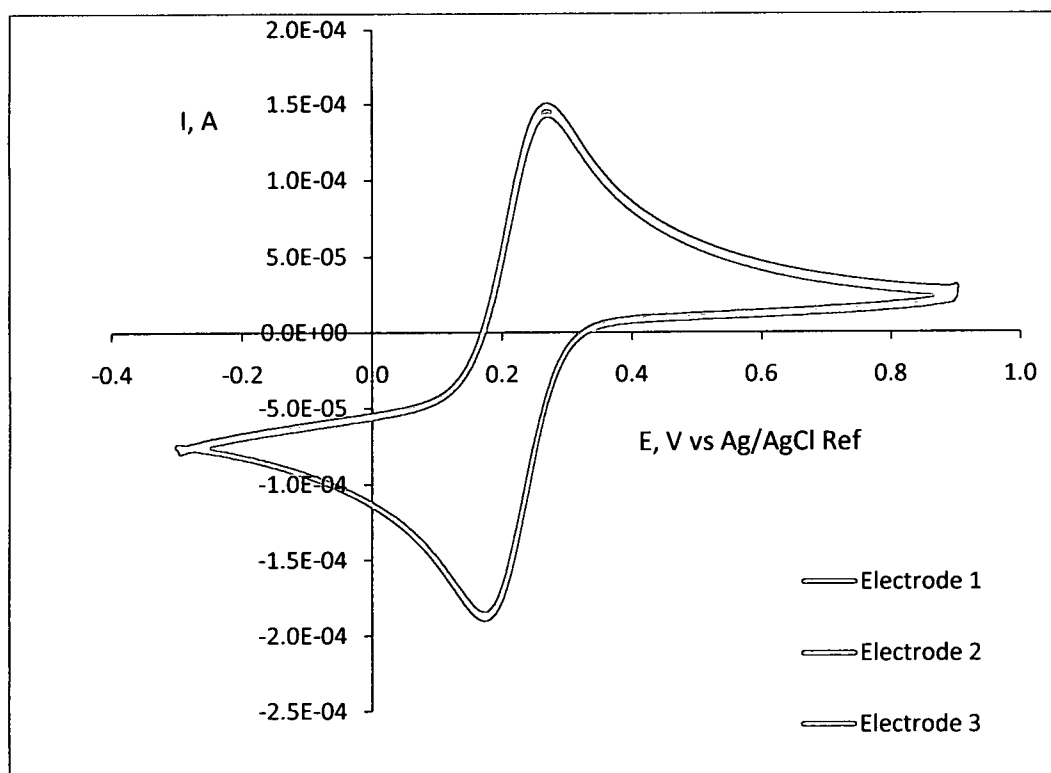


Figure 3.13. Cyclic Voltamograms of Ferricyanide on Electrodes Fabricated with Different Lots of SCNR Clusters at 10mV/s Scan Rate

For electrodes fabricated using SCNR clusters, the peak-to-peak separation measured at a scan rate of 10mV/s was 60mV. This shows electrodes incorporating the SCNR clusters display high consistency between lots. These experiments also illustrate that CTCC produced CNTs (or SCNRs) have high

edge plane character, leading to nearly reversible electrode behavior with ferricyanide. Additionally, CVs were performed on the replicate SCNR modified HOPG electrodes at varying scan rates and are shown in the Appendix (Figures A.15 through A.18). This allows solution of the Randles-Sevcik Equation for area, which is 0.15cm^2 (+/- 3% variation) for the 80ug loading (Figure A.18) for the replicates.

3.4.3 SCNR Modified Open Cell Foam Electrode Behavior

SCNR modified open cell foams were studied for the purpose of characterizing their behavior for bio-fuel cell electrodes and electrochemical double layer capacitors. Arguably, the most significant property of carbon electrodes in general is their extremely high double layer capacitance. It is this property that both complicates their utility for some applications, and ensures their superiority in others. An electrode was initially characterized in 0.1M NaCl (Aldrich, 99.5%) and 0.05M phosphate buffer (Aldrich, 99.5%), of pH 7.2. A background scan of the electrode was done to establish the electrochemical window in an aqueous solution. Figure 3.14 shows the background scan of a representative electrode in 0.1M NaCl and 0.05M phosphate buffer solution, degassed *via* bubbling argon for 15min.

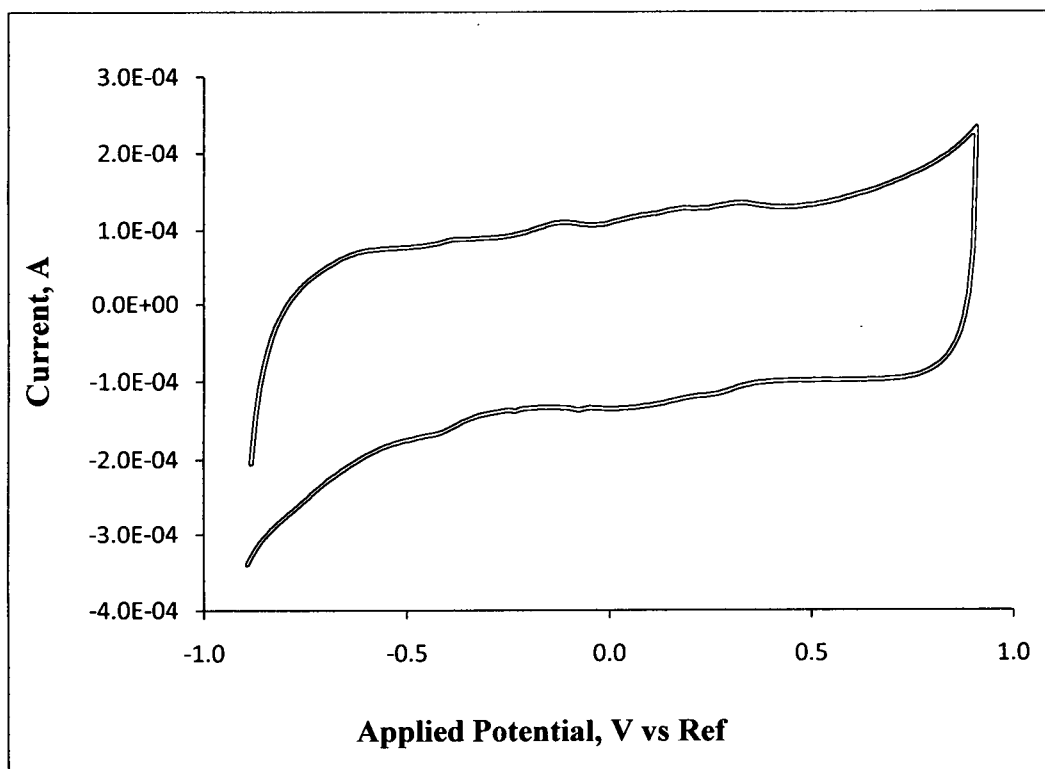


Figure 3.14. Background CV of SCNR Modified Open Cell Foam Electrode

As expected, the foam electrode displayed significant electrochemical capacitance, hinting on utility for fabrication of an electrochemical double layer capacitor, *aka* an ultracapacitor. The high capacitance is a result of the mesoporous architecture created by the interlaced SCNR coating on the electrode. This architecture creates a greatly extended electrochemically active surface area in comparison with the geometric surface area given by ERG. Within this potential window, no unexpected electrochemical waves were observed.

The electrode was then evaluated using the 1mM ferricyanide-ferrocyanide redox couple in 1M KNO_3 as before. Figure 3.15 shows a plot of CVs of the foam electrode at varying scan rates. Cyclic voltamograms using scan rates of 10mV/s, 50mV/s, 100mV/s, 250mV/s, and 500mV/s were obtained in 1M

KNO₃ and 4mM ferricyanide. The second trace of each scan is shown in Figure 3.15.

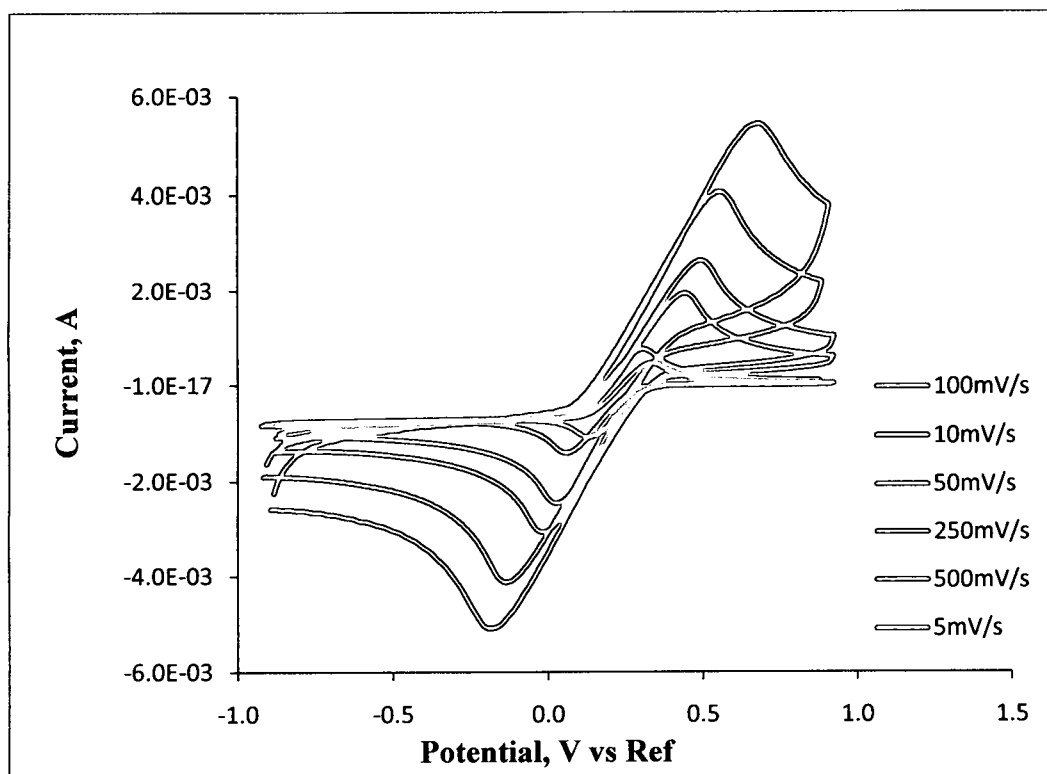


Figure 3.15. CVs of Ferricyanide on SCNR Modified Open Cell Foam Electrode with Varying Scan Rates

Replicate experiments on similar foam electrodes are shown in the Appendix (Figures A.19 through A.23). Variations in size and internal resistance leads to variations in peak separation as well as peak currents (Figure A.19). When corrected for differences in surface area and internal resistance, more consistent performance is observed (Figure A.23).

The data generated in Figure 3.15 was used to develop a plot of current vs. the square root of scan rate, shown in Figure 3.16. This is often used to determine

the area of a given electrode and gain insight into electrochemical reversibility (60).

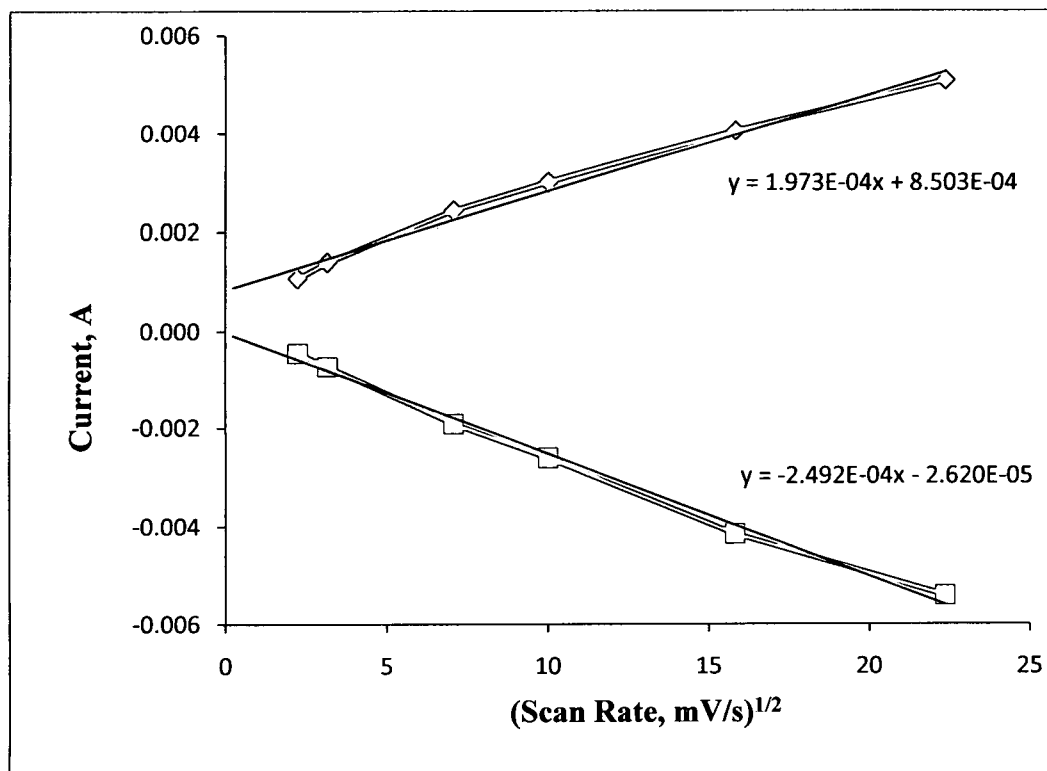


Figure 3.16. Plot of Peak Current vs. Square Root of Scan Rate

Both cathodic and anodic currents vs. the square root of scan rate are approximately linear, indicating a quasi-reversible redox process (58) (61). Using the slope of the trend line in Figure 3.16, one can solve for an approximation of area if diffusivity and concentration are known using the Randles-Sevcik Equation (43). Because the Randles-Sevcik Equation applies strictly for reversible systems, it can be used to determine the minimum area for a quasi-reversible couple. Solution for area yields 10.1cm^2 for the oxidation scan, and 11.7cm^2 for the reduction scan. $7.67 \times 10^{-6} \text{ cm}^2/\text{s}$ is used as the diffusivity for ferricyanide and ferrocyanide (62). The discrepancy in area is likely due to the difference in

starting concentrations (bulk solution concentrations) of ferricyanide and ferrocyanide. The CV in Figure 3.17 shows, as expected, a significant oxidized depolarizer (ferricyanide) bulk concentration effect (43). As these experiments use ferricyanide salt, all ferrocyanide ions present are generated at the electrode, and is thus at significantly lower bulk concentration than the oxidized species.

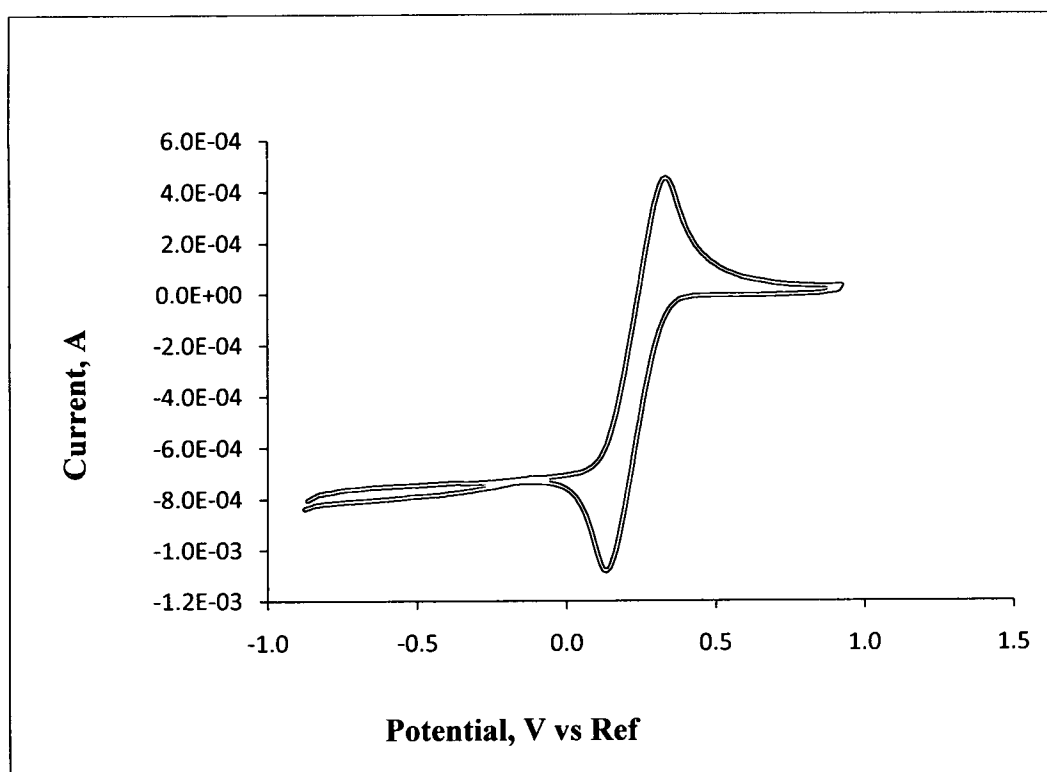


Figure 3.17. Cyclic Voltammogram of Ferricyanide on SCNR Modified Open Cell Foam Electrode, 5mV/s Scan Rate

Bulk concentration effects manifest as significantly greater peak cathodic current than peak anodic current, as well as greater steady state current for the reduction portion of the scan. The use of a 1:1 ratio of ferri-ferrocyanide would have reduced the cathodic current to match that of the anodic current (43).

Interestingly, at slow scan rates, 5 to 10mV/s, the cyclic voltamograms suggest microelectrode behavior as seen in Figure 3.17 (43). This is supported by what is described in the literature for electrodes of 100 μ m and smaller dimension (58). Microelectrode behavior is characterized by non-zero steady state currents in the CVs (58).

A plot of the difference between peak cathodic potential and anodic potential vs. the $\log_{10}(\text{scan rate})$ is shown in Figure 3.18, using data from Figure 3.15. For an electrochemically reversible couple, this should be a horizontal line at $y = 58\text{mV}$ (62).

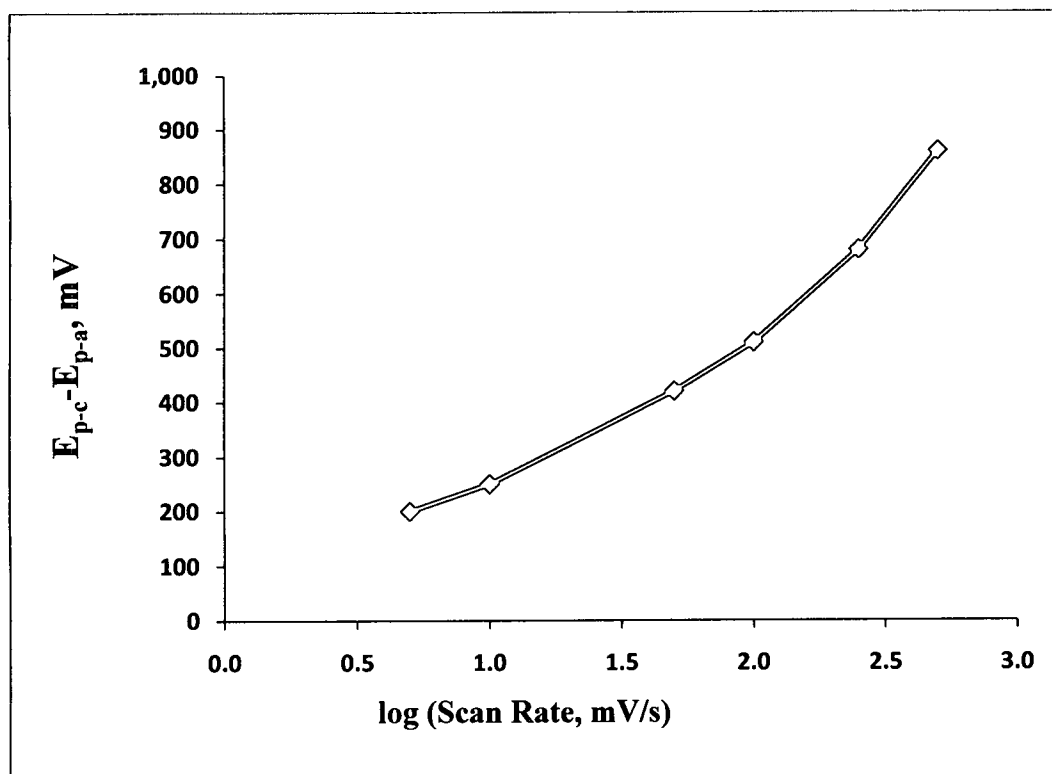


Figure 3.18. Plot of Peak Separation vs \log_{10} of Scan Rate

Deviation of the theoretical ΔE_p Cathodic-Anodic (58mV) is observed at all scan rates. This degree of irreversibility is in conflict with the quasi-reversible behavior seen

in Figure 3.16. This deviation is primarily attributed to the high internal resistance of the electrode.

The principal component of the internal resistance is the undoped polycrystalline SiC layer. Figure 3.19 shows a representation of the series of internal resistors and capacitors present in the open cell foam as tested.

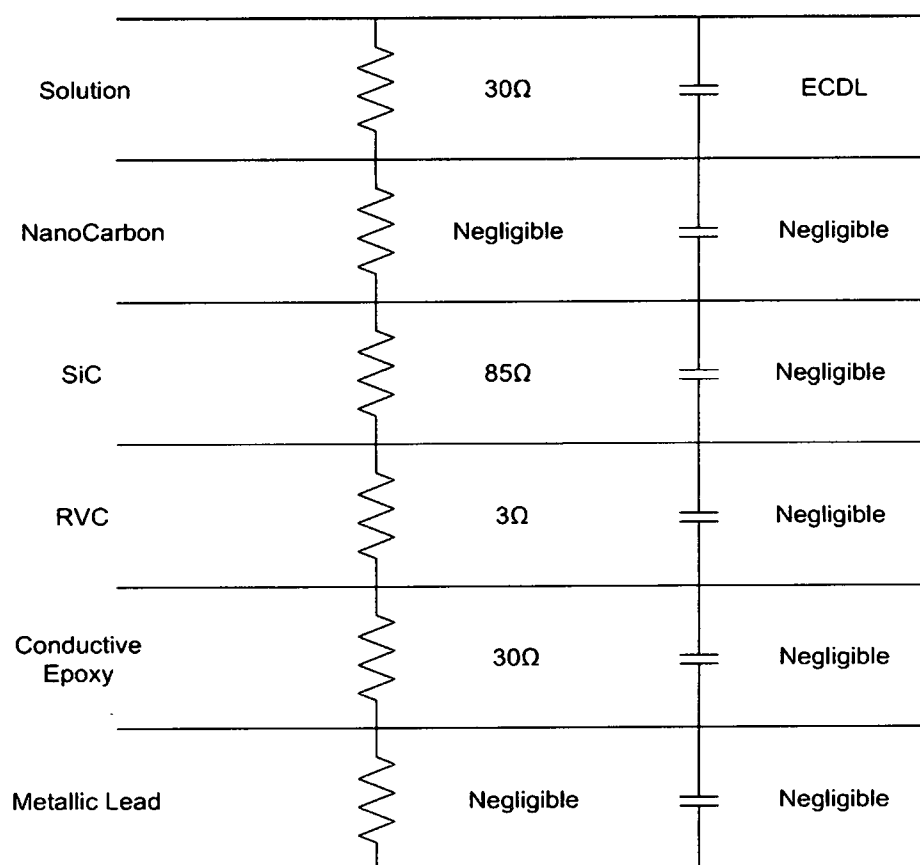


Figure 3.19. Model Electrical Circuit of Open Cell Foam Electrode

As a comparison, the RVC skeleton has a resistance of roughly 1 ohm through a 1mm by 5mm by 10mm piece through the longest dimension. A SiC piece of identical dimensions is 93 ohms, and a SCNR coated piece is roughly the same.

While this does not fully explain the peak separation seen, it contributes to it. By plotting the data shown in Figure 3.15 corrected for internal resistance of the foam electrode, a more accurate view of the electrode performance may be obtained (43). This is shown in Figure 3.20.

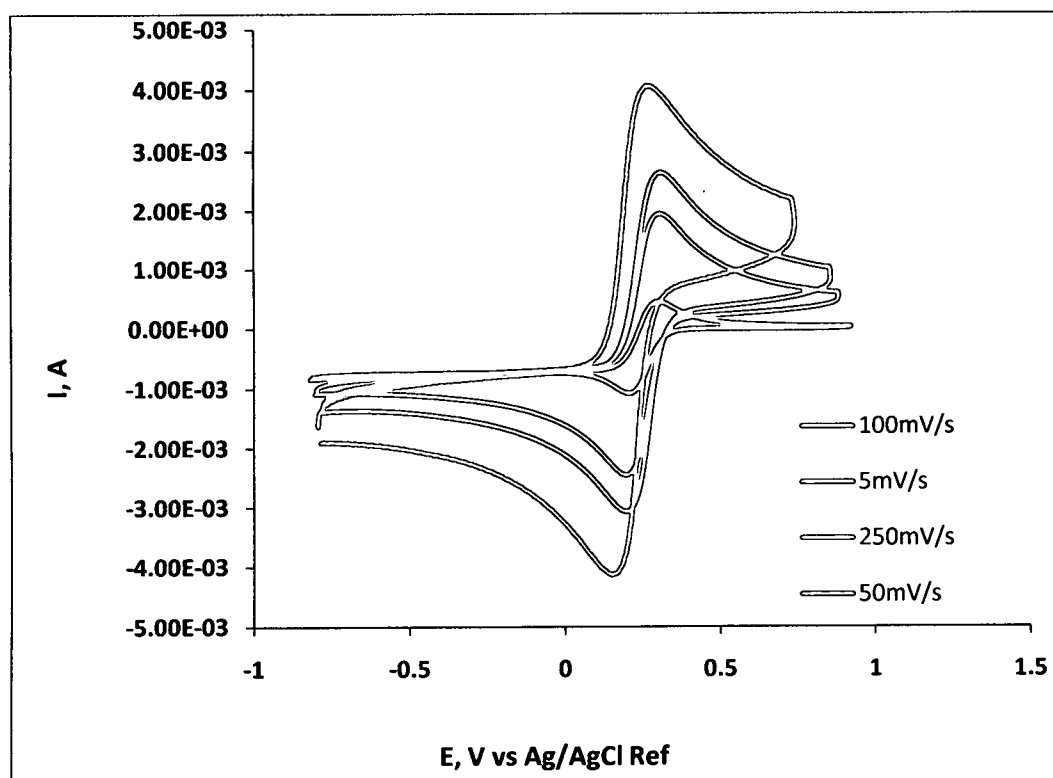


Figure 3.20. IR Compensated CVs of Open Cell Foam Electrode

As can be seen above, at slower scan rates (5mV/s) bulk concentration effects and possible microelectrode behavior can still be seen. Whereas at faster scan rates, in excess of 50mV/s, bulk concentration effects and microelectrode behavior become less significant. Figure 3.21 shows the CV of the open cell foam at 5mV/s scan rate, both uncompensated and compensated for comparison.

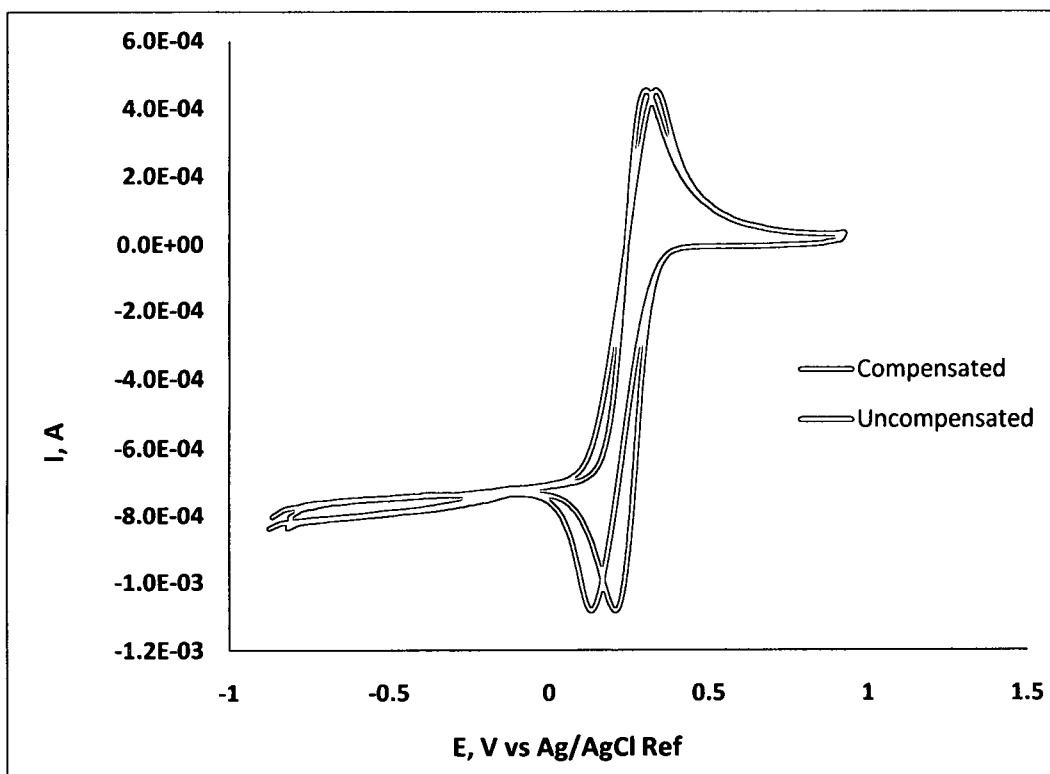


Figure 3.21. Comparison of IR Compensated and Uncompensated CVs of Open Cell Foam Electrode

The uncompensated CV has a peak separation of approximately 180mV, whereas the compensated CV peak separation is roughly 65mV at 5mV/s scan rate. This is much closer to the anticipated performance of a high edge plane carbon material. Plotting peak separation vs. the \log_{10} of scan rate of the IR compensated data yields improved results. This is shown in Figure 3.22.

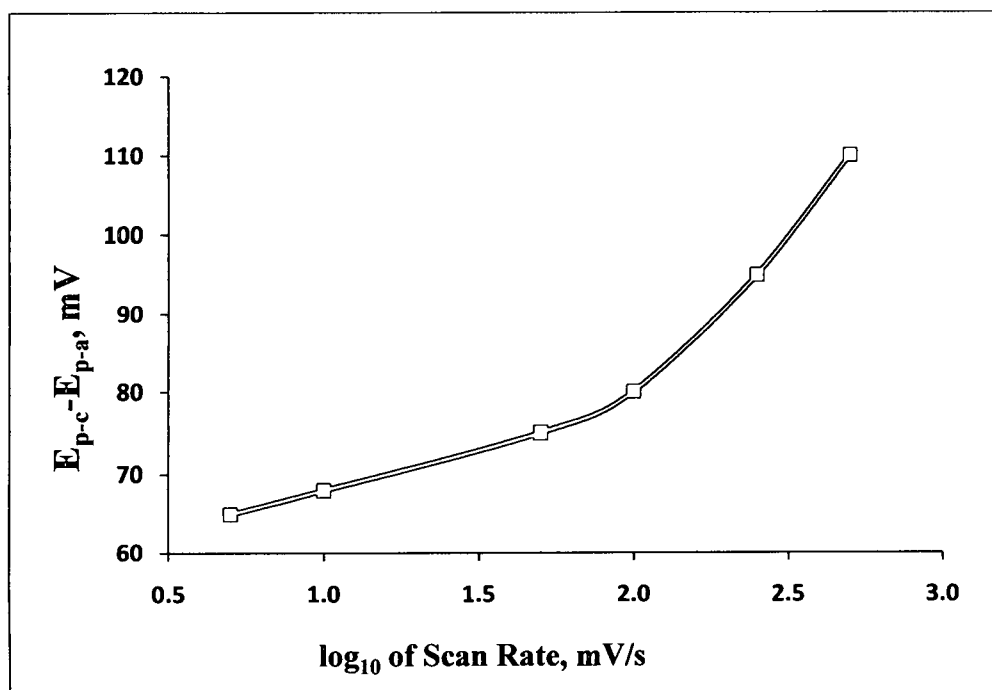


Figure 3.22. Plot of Peak Separation vs \log_{10} of Scan Rate of IR Corrected Electrode

The y-intercept of the trendline shown in Figure 3.22 is 59.8mV. At slower scan rates (5mV/s), quasi-reversible behavior is noted. Thus it is shown that a portion of the irreversible behavior seen with the foam electrode in Figure 3.18 is a result of high internal Ohmic losses.

Charge time experiments can help elucidate many aspects of an electrochemical system, including: concentration, diffusivities, kinetics of heterogenous reactions, and charging/discharging effects (63). Chronocoulometry (CC) uses the same experimental set-up as chronoamperometry, where at a specific time a fixed potential is applied to the electrode. In CC, the total charge passing through the electrode is quantified (current is integrated with time) thus providing a larger signal with time. CC is also useful in systems where there is adsorbed/entrapped analyte. In these systems it is expected that the analyte will be

instantaneously oxidized or reduced. Figure 3.23 shows a double step CC charge – time plot of the open cell foam electrode using the same electrochemical cell as before, in 1M KNO_3 , 4mM potassium ferricyanide. The potential was initially set at 0.6V vs. the reference, then stepped to 0.1V and back to 0.6V at a range of pulse widths of 1s to 30s.

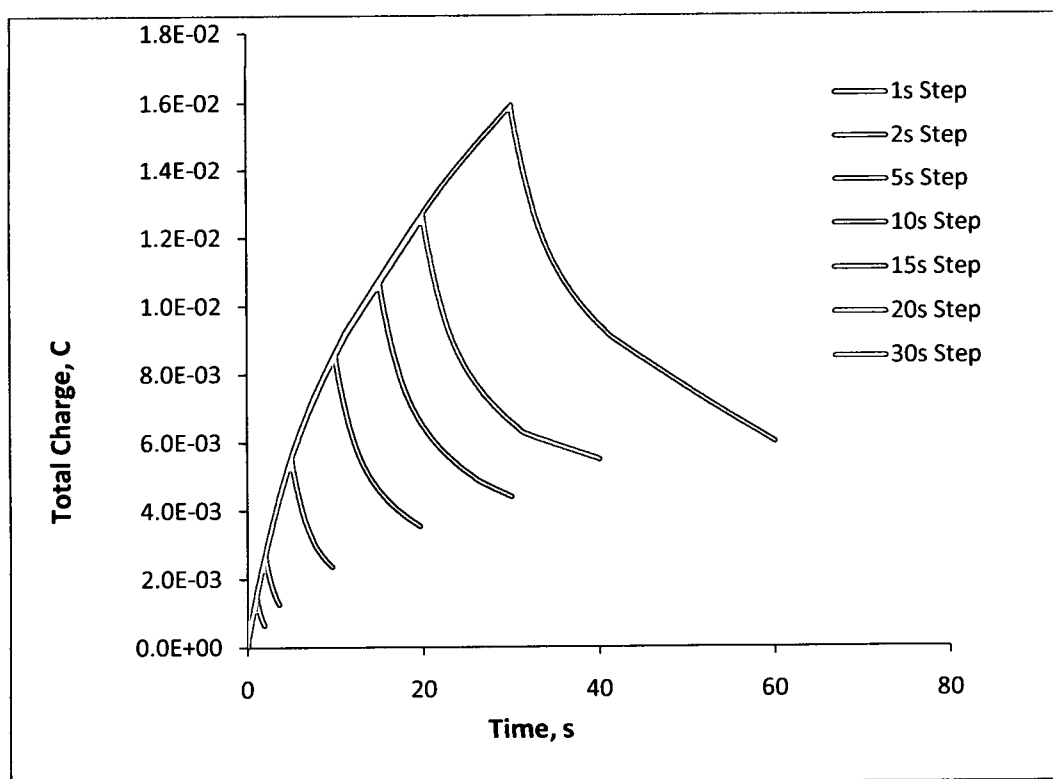


Figure 3.23. Charge – Time Plots of Open Cell Foam Electrode

Inspection of the graph shows no discernable thin layer behavior, typically seen as a plateau during the last third of the initial potential step (58). This is due to exhaustion of the analyte, resulting in no further charge transfer. Adsorbed species behavior is also not seen, which would manifest itself as the second step charge dropping below the x axis. To further verify that an adsorbed species is not present, a plot of charge vs. the square root of time (Q vs. $t^{0.5}$), called an Anson

Plot, is shown in Figure 3.18 (58). The presence of an adsorbed species would be seen as a large difference in y intercepts between the reduction and oxidation steps in the Anson Plot (61). The difference in intercepts shown between the two curves is insignificant considering the uncertainty associated with fitting the data to a straight line and confirms the absence of an adsorbed species.

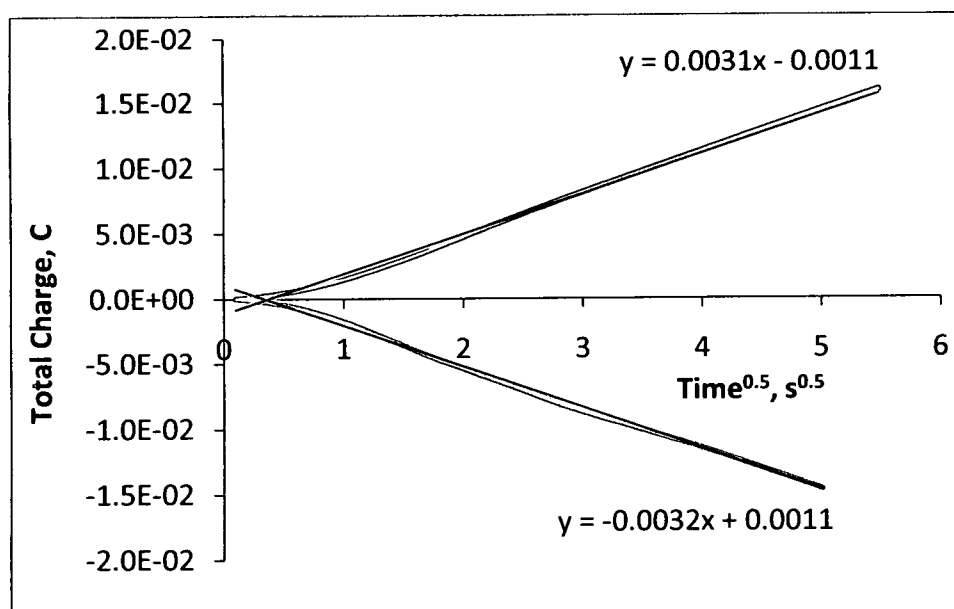


Figure 3.24. Anson Plot of 30s Step Time for Open Cell Foam Electrode

The reduction of ferricyanide to ferrocyanide and re-oxidation is nearly as predicted by the Cottrell equation, as depicted by the linear plots shown in Figure 3.24 above. Using the diffusion coefficient of $7.67 \times 10^{-6} \text{ cm}^2/\text{s}$ for ferricyanide (4mM in 0.1M KNO_3), solving the Cottrell equation for electrode area yields approximately $10\text{-}12 \text{ cm}^2$, which is in good agreement with the area determined using the Randles-Sevcik Equation. Additional charge time experiments are shown in the Appendix (Figures A.8 through A.10).

3.5 Conclusions

The SCNR material exhibits clean electrochemical behavior and the fast electron transfer kinetics expected of high edge plane character materials. The electrochemical behavior of the material is unique among carbon nanotube and nanotube derived materials. Of particular interest is the electrochemical behavior of the SCNR modified foam electrode. No effect of the SiC support material is observed in the background scan. The foam material exhibited the high capacitance expected of a high activity, mesoporous electrode. Some degree of microelectrode behavior is suggested based on the CVs of the material, possibly due to the non-linear mass transport to the individual cell ligaments and to the micrometer size surface features. The most prominent feature of the SCNR modified foam electrode is the peak separation resulting from the high internal resistance. When corrected for the electrical resistance of the electrode, improved reversibility was seen. The electrochemical behavior of these materials suggests value in further investigation for sensor, battery, capacitor, and fuel cell applications.

CHAPTER 4.

SUMMARY AND CONCLUSIONS

4.1 Summary

An economical and scalable process for the production of carbon nanotubes is described and a new mechanism is proposed that more adequately explains the decomposition of silicon carbide and extends it further to alternate carbides. Material produced *via* the process described also displays high edge plane character. Complete conversion of carbide materials into bulk fullerenes is also shown. An investigation into the properties of the material is done with Raman spectroscopy and high resolution transmission electron microscopy. The electrochemical behavior of the material is then studied with cyclic voltammetry and chronocoulometry.

It was determined that other metal or metalloid carbides can be used to produce unique and valuable carbon nanotube derivative materials. The process described by Kusunoki necessitated the use of small quantities of silicon carbide under economically unscalable conditions. Kusunoki describes a process requiring high vacuum levels, 10^{-7} Torr, and very slow ramp rates to produce

CNTs. The process described herein allows the production of material in a mechanically agitated process to allow radically increased production capabilities.

The material was characterized via Raman spectroscopy and high resolution transmission electron microscopy. Purity was determined with ICP-MS and EDS, and confirmed with electrochemistry. SCNRs produced via the CTCC process have a unique blend of SWCNT and MWCNT characteristics. Materials produced *via* CTCC display narrow G and D bands in the Raman spectra more characteristic of isolated SWCNTs. Further verification of the cylindrical structure of the material is shown by the splitting of the G band into individual G^+/G^- peaks, typically only seen in isolated SWCNT spectra.

Perhaps most interestingly, CTCC produced materials exhibit unique and enhanced electrochemical behavior over other carbon electrode materials, including commercial MWCNTs. The importance of electrochemical purity is demonstrated through comparison of background scans and CVs in the presence of hydrazine. Increased electron transfer rates are shown by comparison of peak separation of SCNRs vs. graphite paste electrodes in the cyclic voltamograms. The first instance of electrochemistry using substrate attached carbon nanotubes was shown with the SCNR open cell foam electrode.

4.2 Conclusions

Carbon nanotubes (CNTs) have been produced by the decomposition of organic vapors and studied extensively since their discovery in 1952 by

Radushkevich and Lukyanovich, presented in the Russian Journal of Physics. Single walled carbon nanotubes (SWCNTs) have been fabricated via organic vapor synthesis since 1976. Single walled and multi-walled carbon nanotubes (MWCNTs) have been discovered occurring naturally in carbonaceous materials and synthesized by a multitude of techniques for decades. However, solid state production techniques have not been investigated until now for the scalable production of carbon nanotubes or the related structure, solid carbon nanorods (SCNRs).

Arguably, the most significant impact CNTs will have on technology will be in the electronic and electrochemical industries. However, it is in these industries where research has been most misled by prior research. As has been demonstrated in the literature, the electrocatalytic nature of CNTs may be attributed significantly to the presence of residual catalyst. This is as significant an issue for the application of CNTs in the energy storage and generation industry as it is in the sensors industry. For CNTs and their related structures to be applied to industrial scale energy devices and production, significant advancement must be made in three areas: production quantity, consistency and purity. The use of a solid state production technique will result in greater consistency as a result of the greater control over process parameters and raw materials. Additionally, since no catalysts are used in synthesis, no residual catalyst is present in the as produced carbon nanostructures. Further post treatment also makes obtaining consistent materials difficult. Post-treatment of CNTs to remove residual catalyst influences their properties through oxidation and bond scission, thus changing edge plane

character and redox state of the allotrope. Potential for increasing production quantity was demonstrated through the use of a retort.

It has been demonstrated conclusively that residual metal catalyst may interfere with electrochemical behavior of carbon nanotube electrodes, and that all current methods of production leave residual impurities. Additionally, the extremely high aspect ratio of commercial CNTs may also serve to hinder incorporation into some processes, such as ink jet printing. The high aspect ratio inhibits the formation of micelles in aqueous media, necessitating the use of extremely expensive and inconsistent functionalized CNT materials. As a consequence, SCNR clusters may be effectively dispersed in organic and aqueous media thus allowing efficient production of printed electrodes for thin film batteries.

It is believed that the commercialization of this technology will enable the successful integration of carbon nanotube derivative materials into electrochemical applications. In electrochemistry, the value of an electrode is directly related to its purity and consistency. It has been demonstrated that the consistency and performance of nano-phase carbon electrodes is greatly influenced by post treatment. As produced SCNR material provided sufficiently clean electrochemical response for most applications, not needing further treatment prior to use. Both the MWCNT paste electrode and SCNR paste electrode exhibited significantly faster heterogeneous electron transfer rates over the carbon paste electrode due to their higher effective edge plane content. At 50 wt% carbon content in mineral oil, both the CNT and SCNR electrodes exhibited

thin layer electrode behavior, indicating entrapment of analyte in the lattice work. This may provide a convenient mode of storage for hydrogen, catalyst particles, and lithium or other metal ions. Additionally, the SCNR paste electrode exhibited a more stable background current with successive scans. The nanoporous nature of the SCNR electrode, fast electron transfer rates, and clean electrochemistry as produced indicate high value in battery, capacitor and especially fuel cell electrode applications. SCNR modified open cell foams represent a very promising electrode material for applications requiring a robust, stable platform exhibiting high surface area. Such applications include electrochemical double layer capacitors and fuel cell/battery electrodes. Currently, research is underway to better understand the electrochemical behavior of substrate grown SCNR electrodes. This includes modification with green energy relevant proteins including: glucose oxidase, nitrate reductase, glycerol oxidase, and alcohol oxidase. Electrodes are being functionalized to improve attachment of enzymes and improve electron transport, with the goal of achieving direct electron transport.

APPENDIX

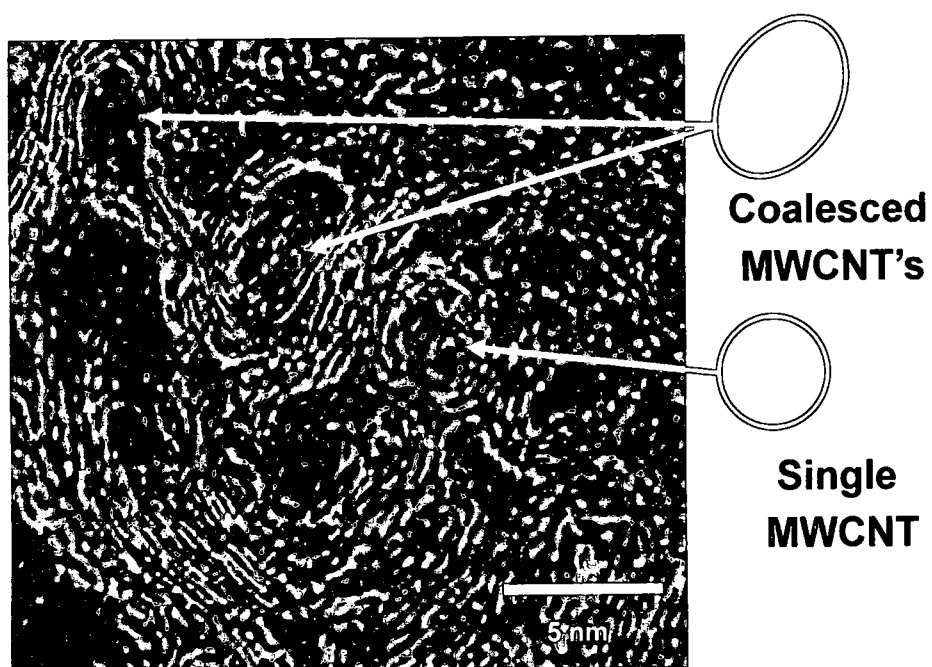


Figure A.1. Plan View of Vertically Aligned CNT Array form Single Crystal SiC
(Image Courtesy J. Boeckl)

Figure A.1 was obtained *via* top down imaging using a high resolution SEM microscope at WPAFB-AFRL with the assistance of J. Boeckl. This images shows a typical “plan view” seen with vertically aligned MWCNTs as produced with the Kusunoki process. Hollow structures can be seen as indicated, demonstrating concentric rings of graphene forming the cylindrical structure.

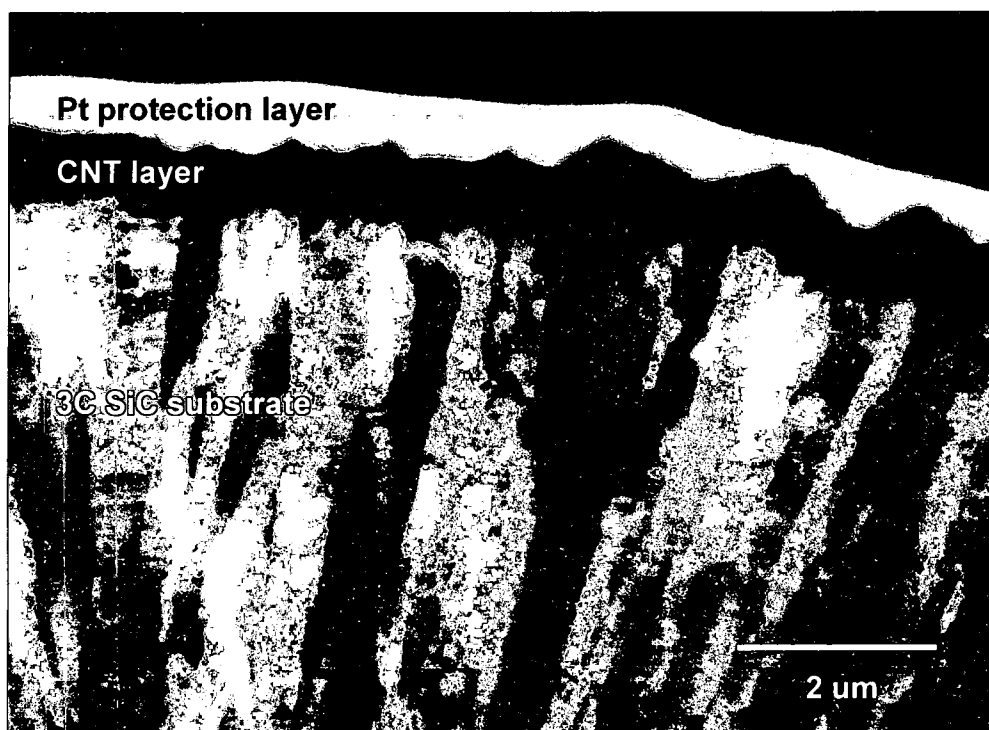


Figure A.2. Low Magnification HRTEM Image of SCNR Layer Grown From ERG Aerospace Open Cell Foam (Image Courtesy J. Boeckl)

Figure A.2 shows the columnar structure of the SiC layer as delivered in the ERG open cell foam. The polycrystalline morphology of this material, in conjunction with the rough surface as a result of crystal growth is directly responsible for the mesoporous architecture seen on the resulting SCNR layer. The Pt protection layer was deposited to allow slicing of the sample with the FIB.

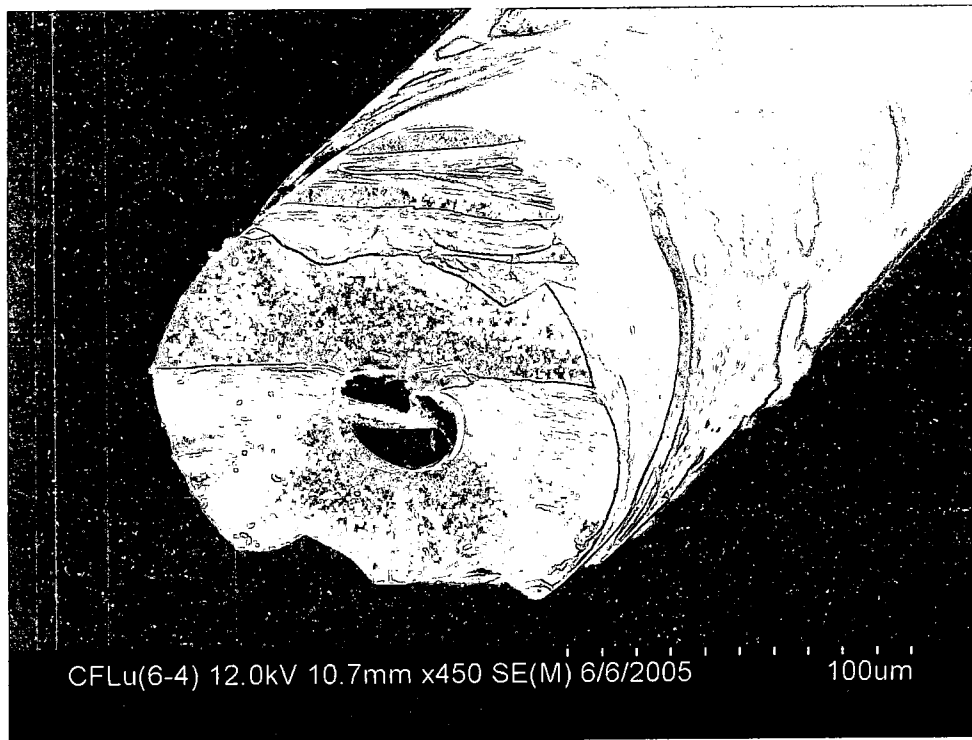
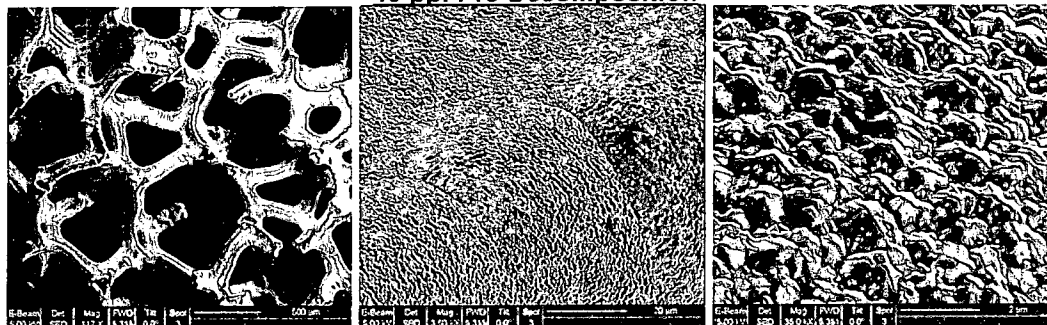


Figure A.3. SEM Image of SCS-6 SiC Coated Carbon Fiber Pre Processing

Figure A.3 shows a fractured cross section of the SCS-6 SiC coated carbon fiber as delivered by Specialty Materials Inc. This material, as delivered, is coated with an amorphous SiC layer, deposited *via* CVD. Prior to use, these materials must be crystallized to produce crystalline carbon products.

SEM SiC Foam material

45 ppi Pre-Decomposition



45 ppi Post-Decomposition



Figure A.4. SEM Images of Foam Pre and Post CTCC Processing
(Courtesy J. Boeckl)

Figure A.4 shows a comparison of the pre and post CTCC processed open cell foam as received from ERG. These images illustrate the believed origins of the blended microelectrode – porous electrode behavior discussed in Chapter 3.

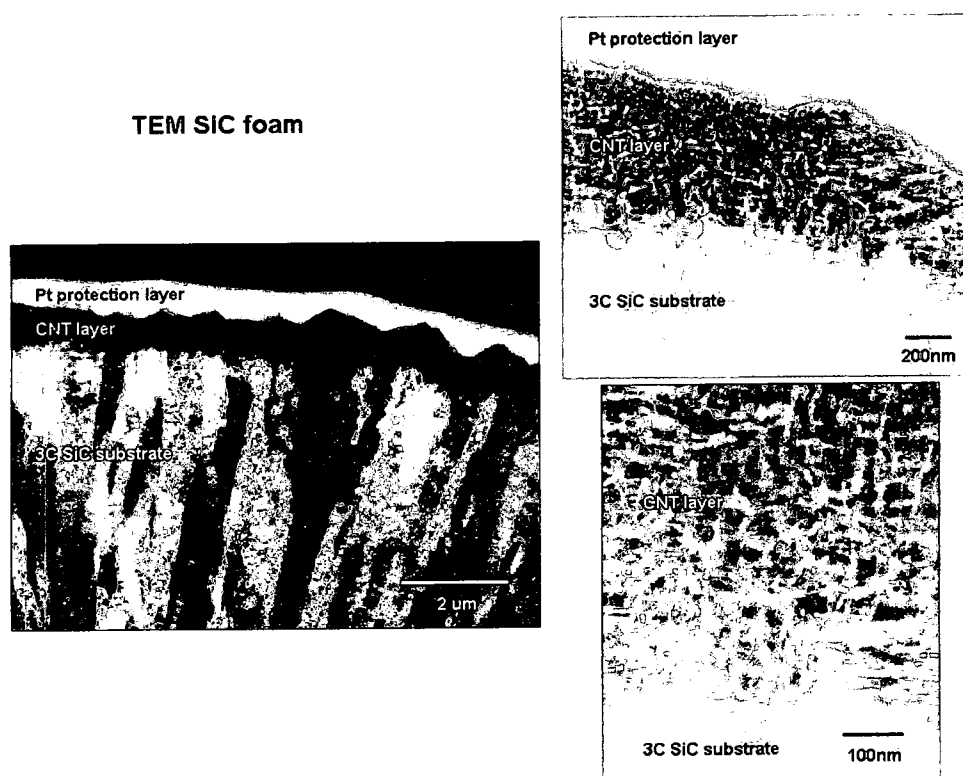


Figure A.5. Increasing Magnification HRTEM Images of SCNR Modified Open Cell Foam (Courtesy J. Boeckl)

Figure A.5 shows cross sectional images obtained *via* FIB milling followed by HRTEM imaging. This image better shows the interface of the SCNR layer and SiC layer. The lower right image provides detail on the mesoporous architecture resulting from polycrystalline starting materials.

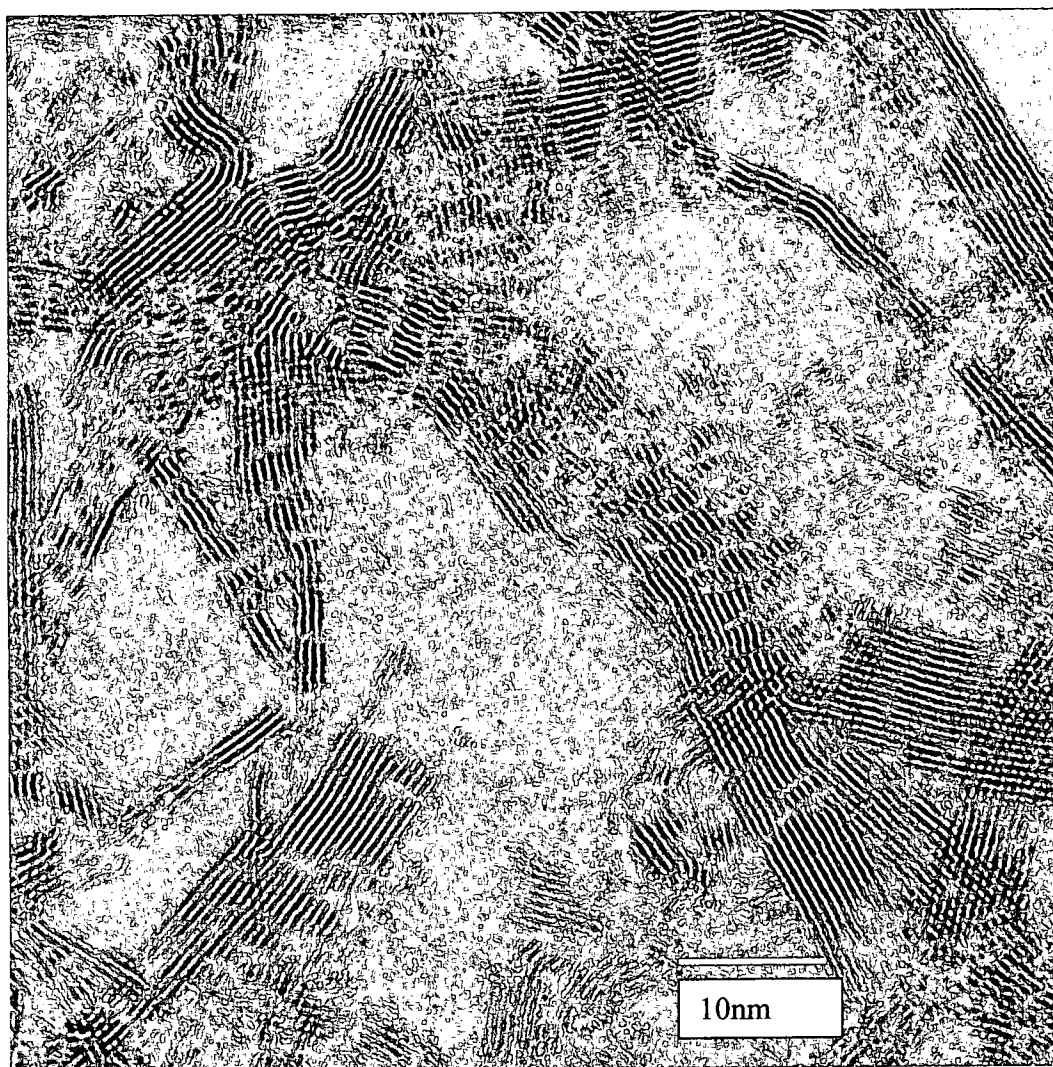


Figure A.6. HRTEM Image of Nanoclusters
(Image Courtesy C. E. Banks)

Figure A.6 is a HRTEM image of a nanocluster sample of a different production run than shown in Figure 2.15, delivered to C. E. Banks for imaging. The image was one of a series taken at Oxford University. Individual and bundles or ropes of SWSCNRs can be seen clearly.

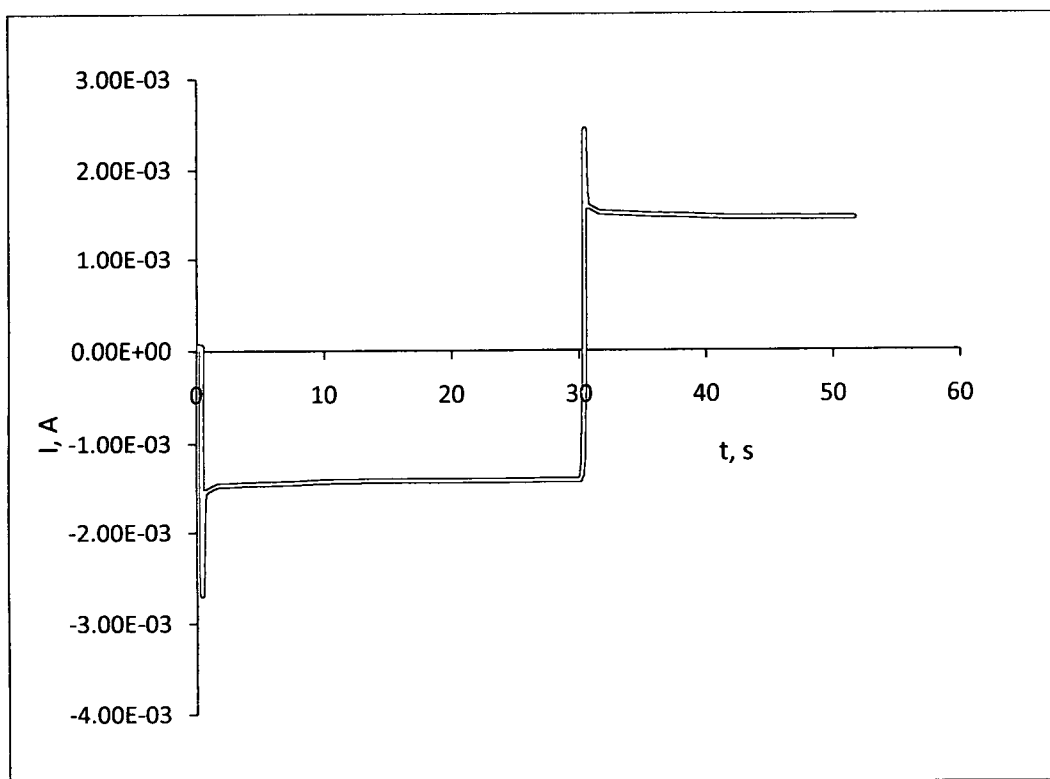


Figure A.7. Chronoamperometry of SCN- Modified Open Cell Foam Electrode, 30s Step

Figure A.7. shows a representative double step chronoamperometry experiment using the open cell foam electrode. The same experimental conditions and set up were used for this experiment as were used for the chronocoulometry experiments. The electrode was stepped to +600mV at time $t=0$ s from 0mV. At time $t=30$ s, the potential was stepped back to 0mV vs. the Gamry reference electrode.

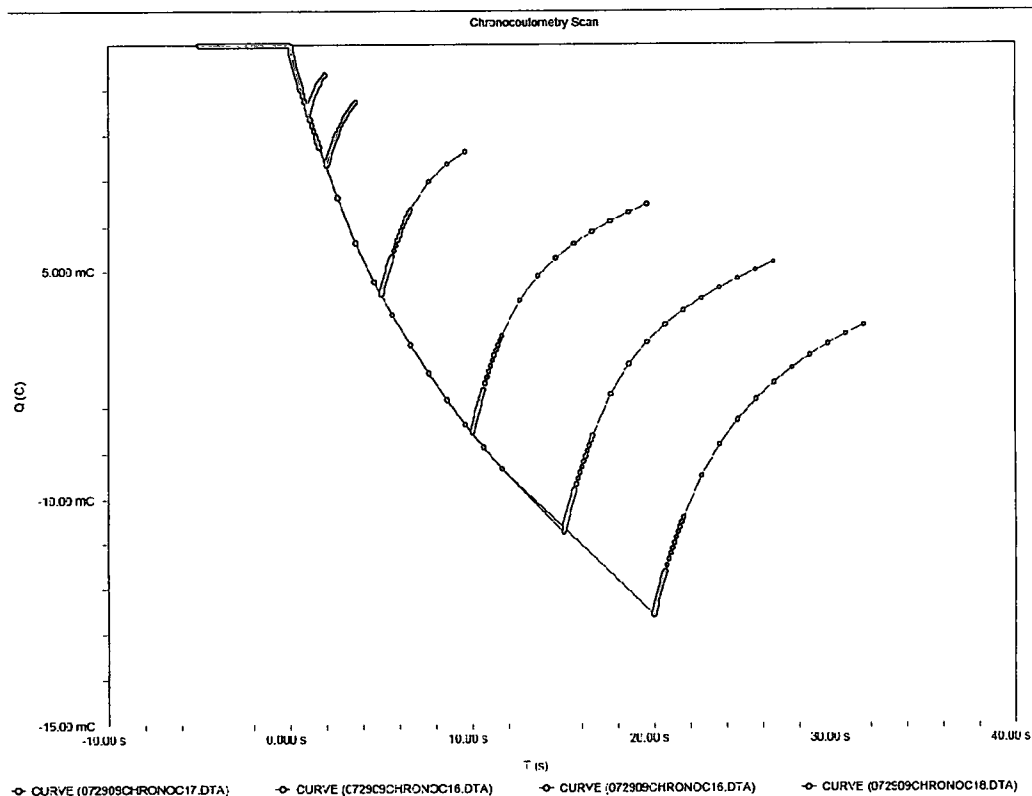


Figure A.8. Charge-Time Plots of SCNR Modified Open Cell Foam Electrode

Figure A.8 was obtained by double step chronocoulometry of the open cell foam modified with a nanocarbon coating. The same experimental setup and procedure were used for this series of experiments as used in Figure 3.23. In this experiment, the potential steps were reversed, stepping from 0.6V to 0V and back to 0.6V vs. the Ag/AgCl reference electrode.

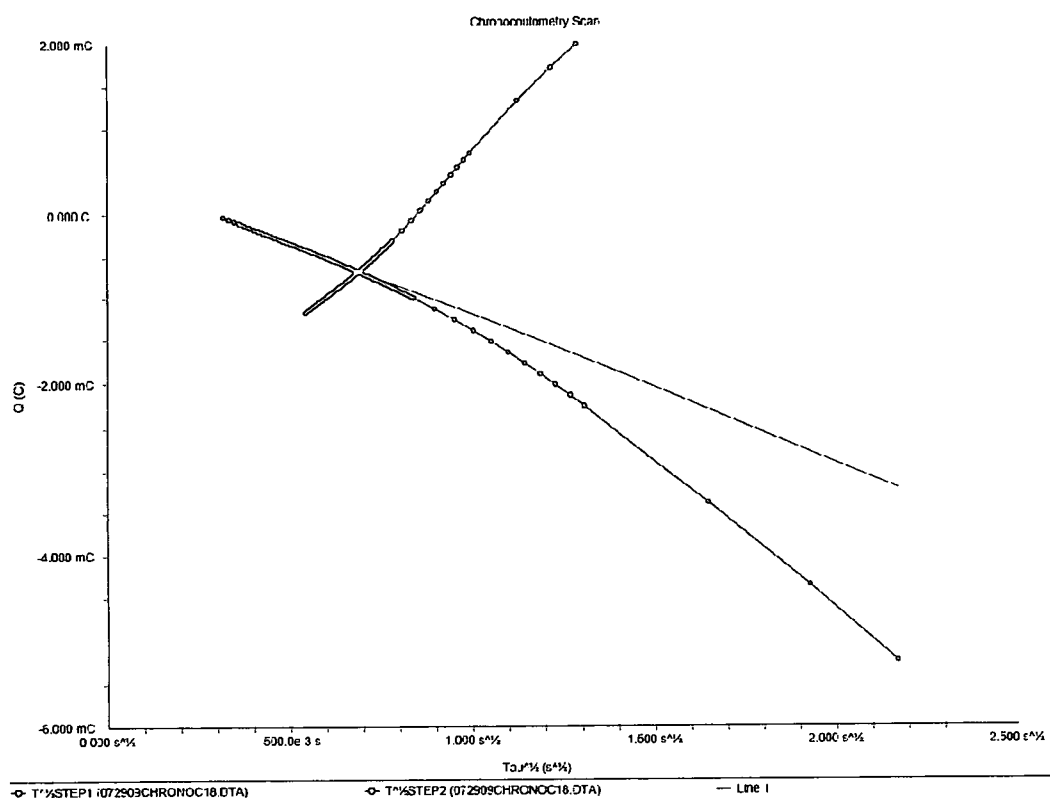


Figure A.9. Anson Plot of 5s Step from Figure A.8

Figure A.9 shows the Anson Plot of the 5s step for the 0V to 0.6V CC experiments. Analysis of the plot for area, assuming 4mM concentration, $7.7\text{E-}6$ cm/s diffusion coefficient, and a single electron process, yields an area of approximately 14.3cm^2 . This value was arrived at using the Cottrell Equation, as before.

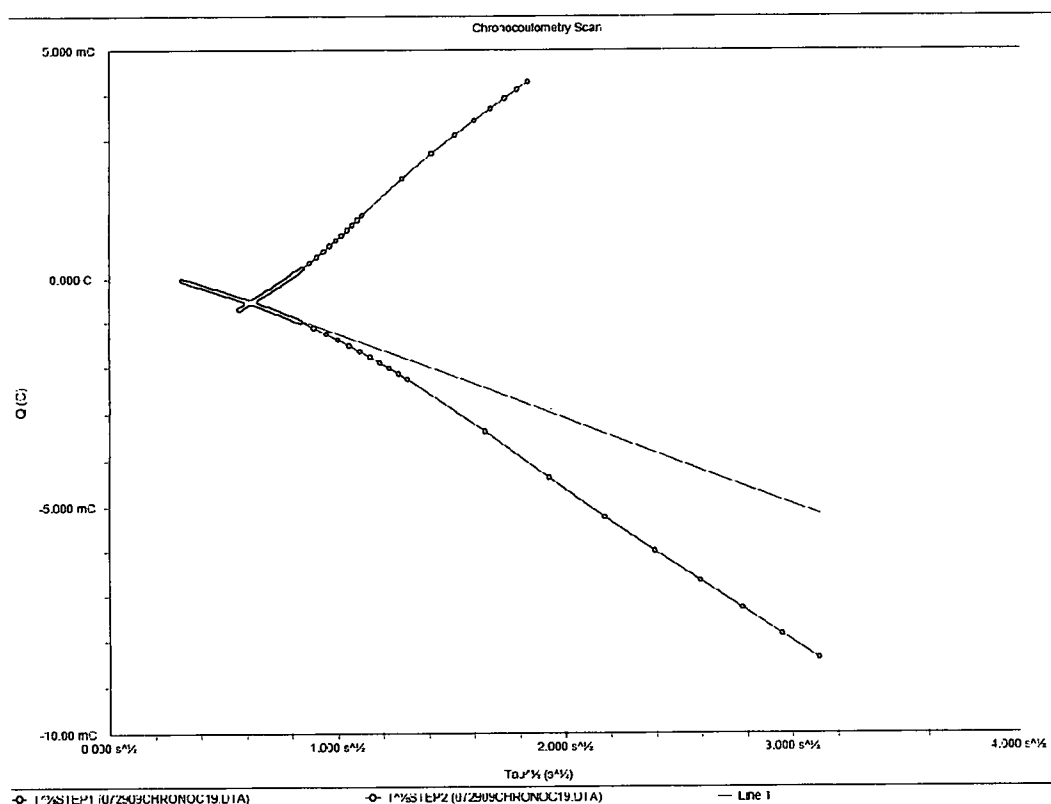


Figure A.10. Anson Plot of 10s Step from Figure A.8

Figure A.10 was obtained analogously as Figure A.9. Using the same parameters in the Cottrell Equation as before, the slope of this plot gives an area of approximately 15.3cm^2 .

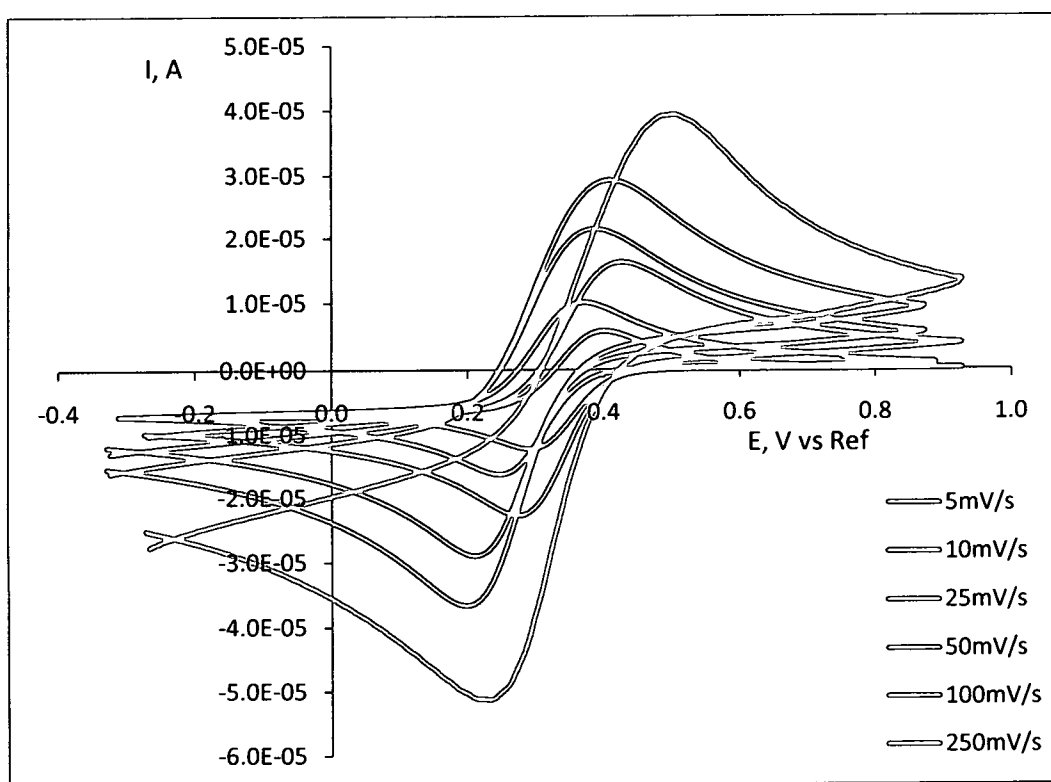


Figure A.11. Cyclic Voltammograms of 4mM Ferricyanide in 1M KNO_3 at SCNR Paste Electrode

Figure A.11 shows cyclic voltammograms of ferricyanide at a SCNR paste electrode material. SCNRs were produced from Sigma SiC nanopowder as described in Chapter 1. The material was produced on 06/22/08, and fabricated into a paste electrode on 08/17/09.

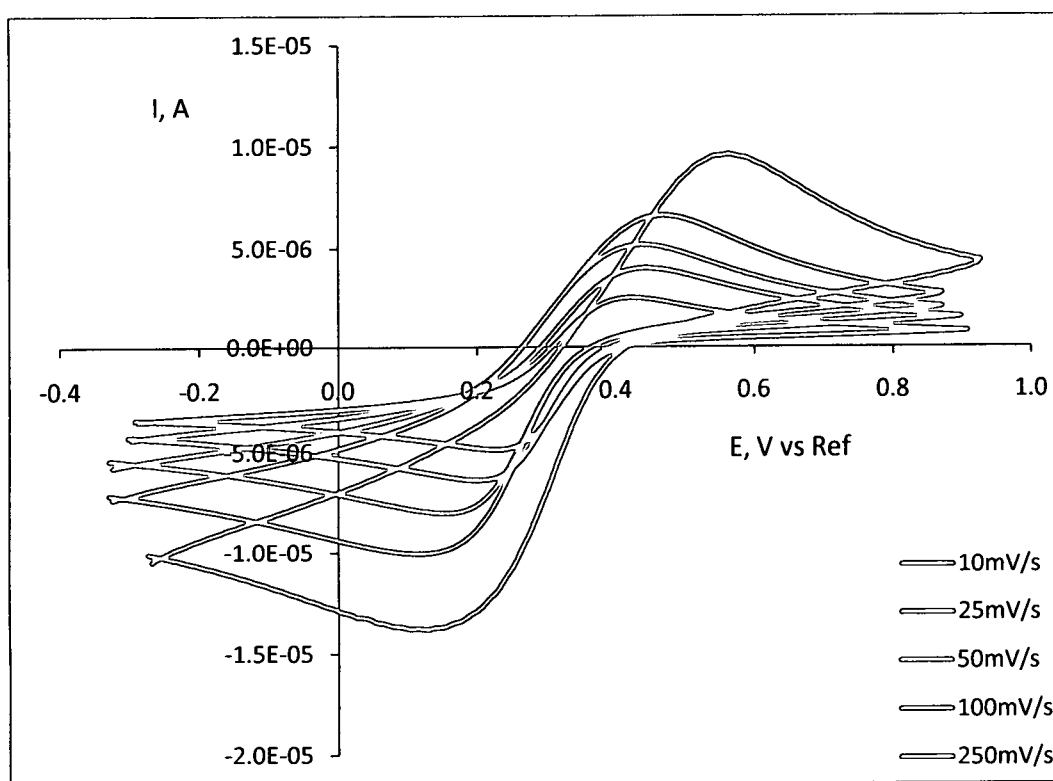


Figure A.12. Cyclic Voltammograms of 4mM Ferricyanide in 1M KNO_3 at SCNR Paste Electrode

Figure A.12 shows a replicate experiment of that shown in Figure A.11, using SCNRs produced on 09/04/07, and fabricated into a paste electrode on 08/17/09 using identical process parameters as described previously. The material was then made into a paste electrode and used as described in Chapter 3.

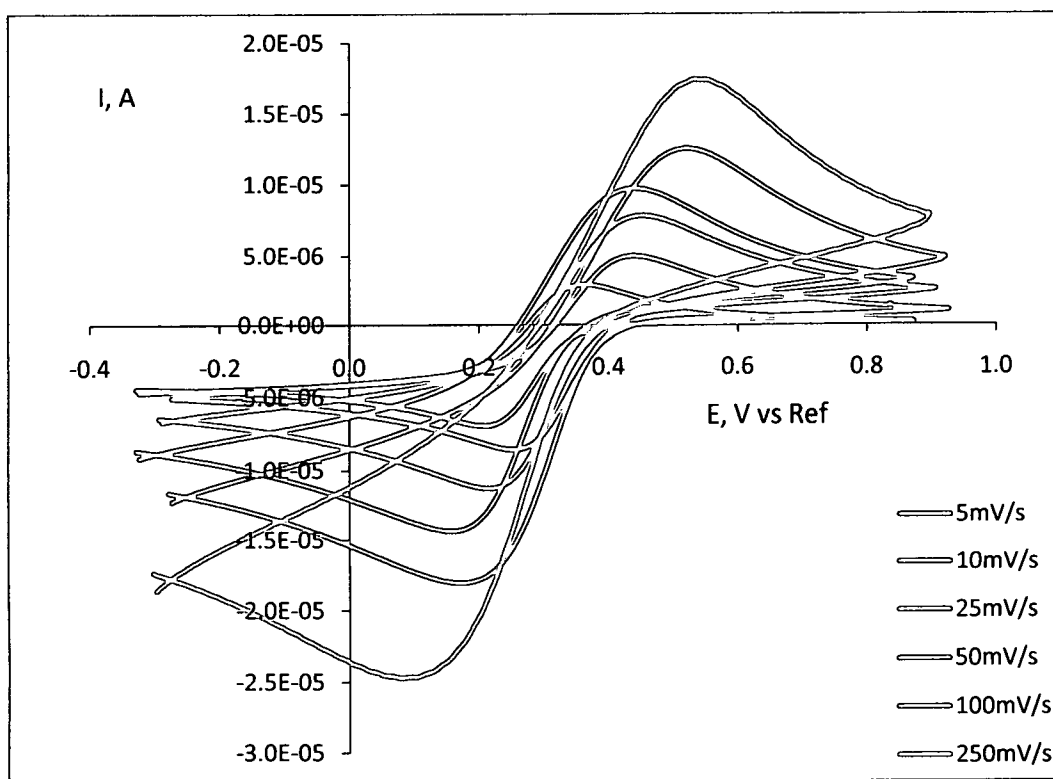


Figure A.13. Cyclic Voltammograms of 4mM Ferricyanide in 1M KNO_3 at SCNR Paste Electrode

Figure A.13 shows a replicate experiment of that shown in Figure A.11, using SCNRs produced on 12/14/07, and fabricated into a paste electrode on 08/17/09 using identical process parameters as described. The material was then made into a paste electrode and used as described in Chapter 3.

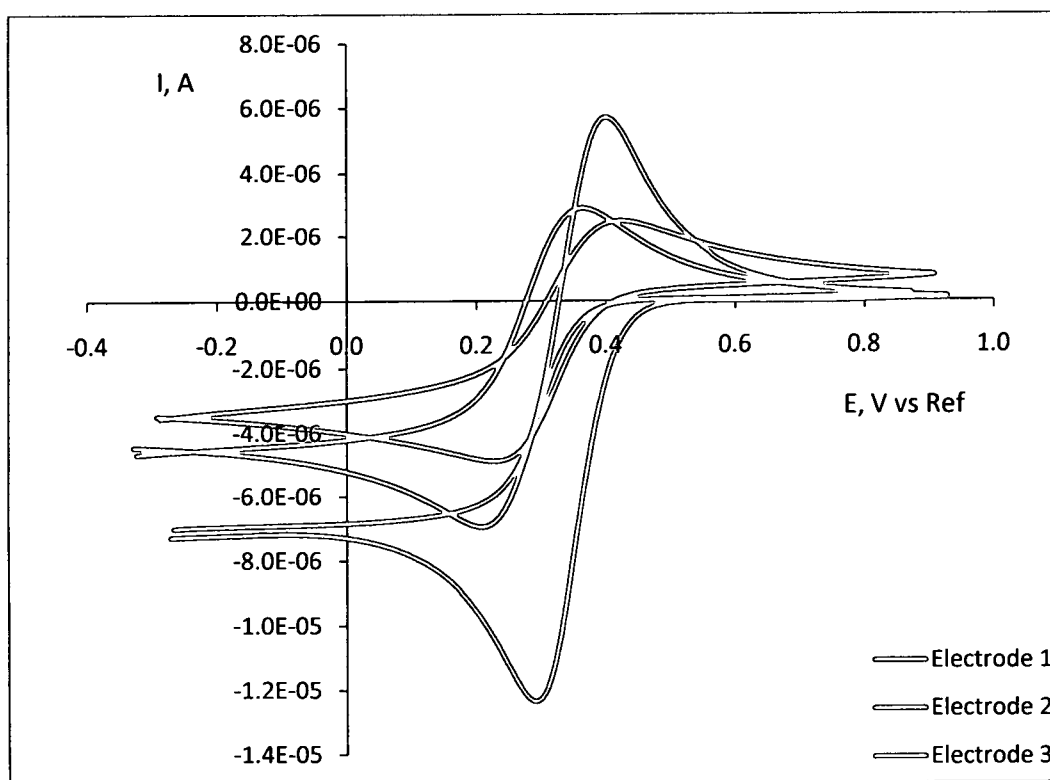


Figure A.14. Electrochemical Performance Comparison of SCNR Paste Electrodes Fabricated from Different Lots of SCNRs Using Cyclic Voltammetry in 4mM Ferricyanide

Figure A.14 shows the 5mV/s cyclic voltamograms of three separate SCNR paste electrodes, each fabricated from a different lot of SCNRs. The data compared is from the preceding figures, Figure A.11 through A.13. Variability in peak separation and peak current are easily discernable. Such variation is inherent in paste electrodes due to sensitivity to variations in production.

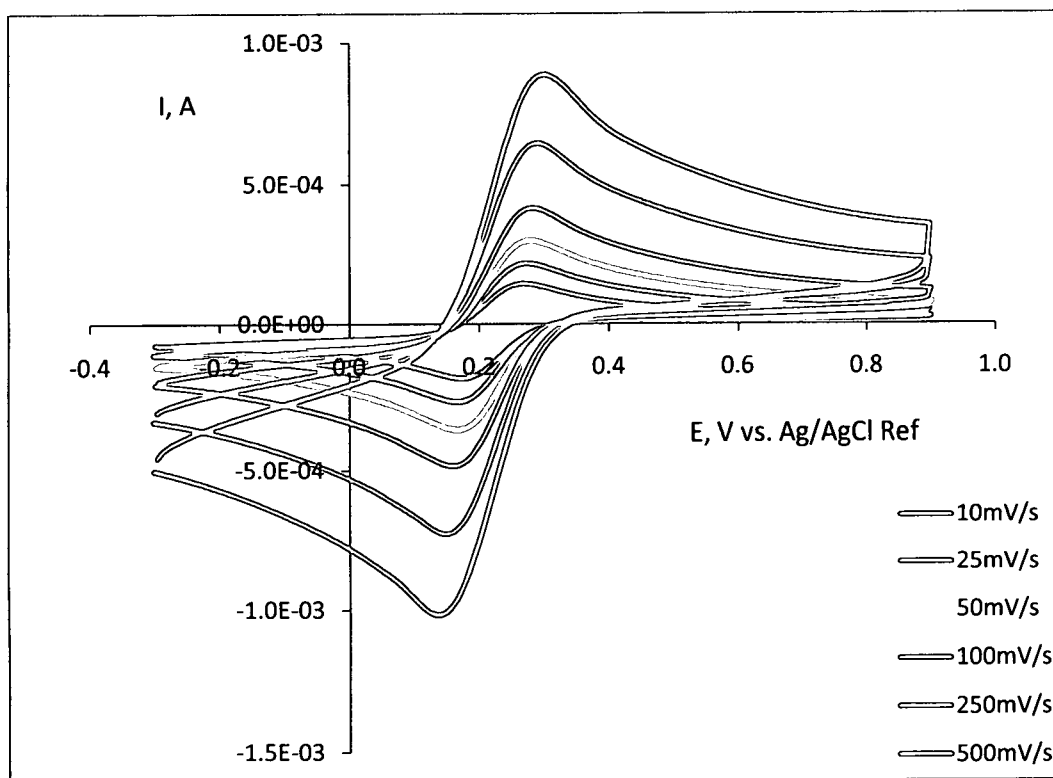


Figure A.15. SCNR Modified HOPG Electrode Cyclic Voltamograms in 4mM Ferricyanide

Figure A.15 shows a series of CVs of a SCNR modified HOPG electrode in 4mM ferricyanide and 1M KNO_3 . The electrode is identical to the HOPG electrodes shown in Figures A.16 and 17. Electrodes shown in Figure A.15 through A.17 were fabricated using the same type of nanomaterial, but from different lots. Figure A.15 used nanomaterial from material produced on 07/14/07 from Sigma Aldrich SiC nanopowder.

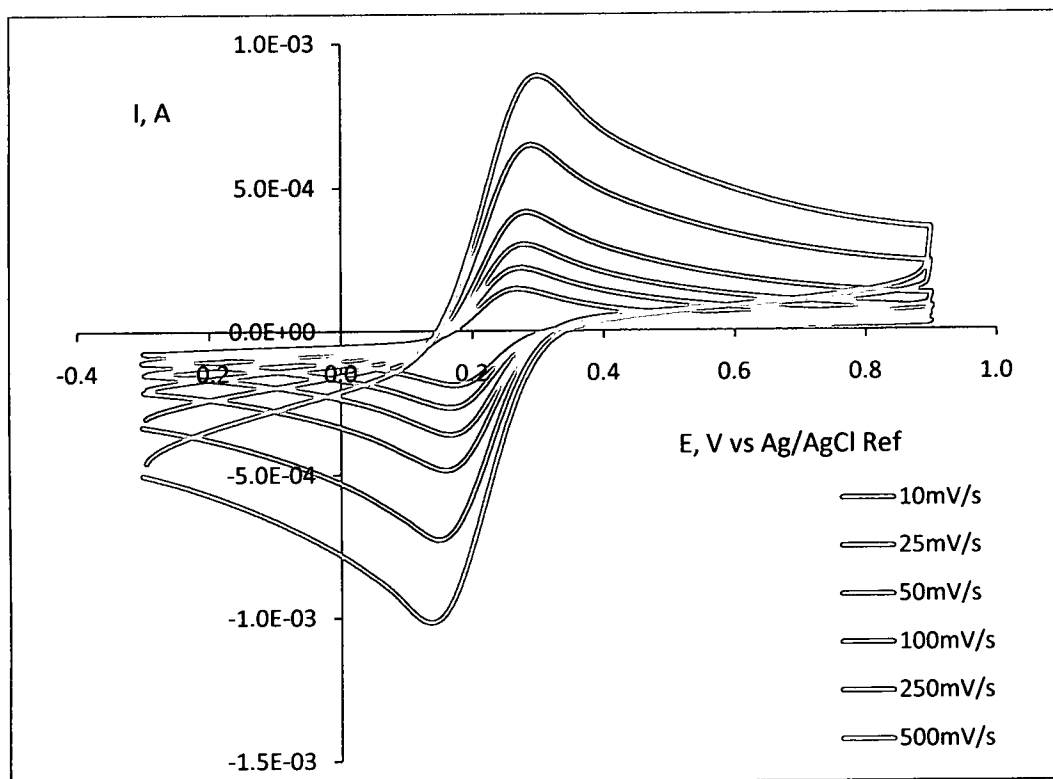


Figure A.16. SCNR Modified HOPG Electrode Cyclic Voltammograms in 4mM Ferricyanide

Figure A.16 shows the response of a SCNR modified HOPG electrode to 4mM ferricyanide in 1M KNO_3 with various scan rates. The electrode used in Figure A.16 is identical to that shown in Figure A.15 and A.17, except A.16 used nanomaterials produced on 02/15/08.

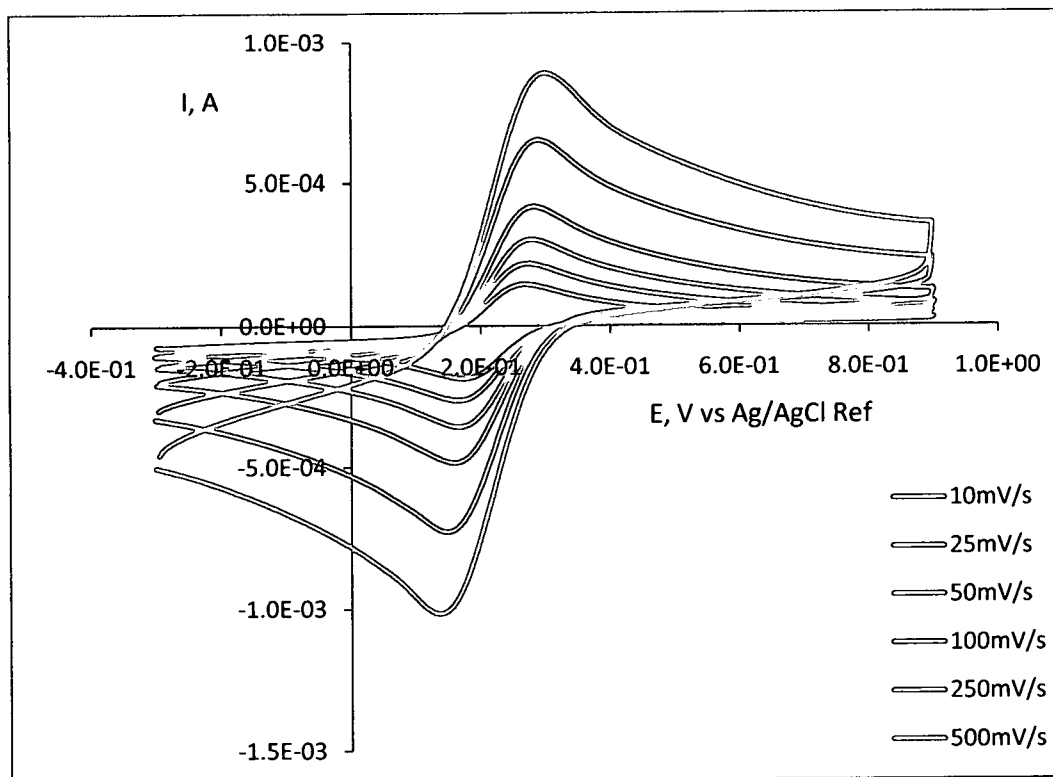


Figure A.17. SCN-Modified HOPG Electrode Cyclic Voltammograms in 4mM Ferricyanide

Figure A.17 is a replicate of the experiments done in Figure A.15 and Figure A.16, using material produced on 09/22/08.

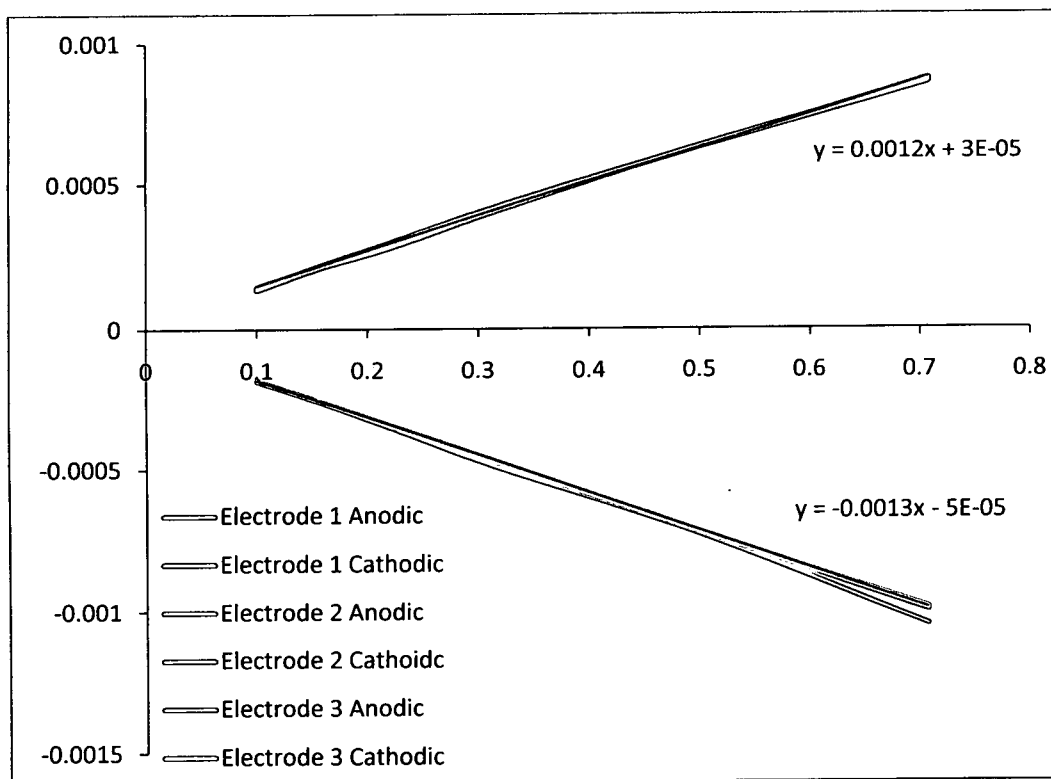


Figure A.18. Plot of Peak Currents of Modified HOPG Electrodes vs. Square Root of Scan Rate

Figure A.18 shows a plot of peak currents for the three replicate modified HOPG electrodes vs. the square root of scan rate. Solution of the Randles-Sevcik Equation yields an electrode area of approximately 0.15cm^2 for each electrode, with a less than 3% variation between electrodes.

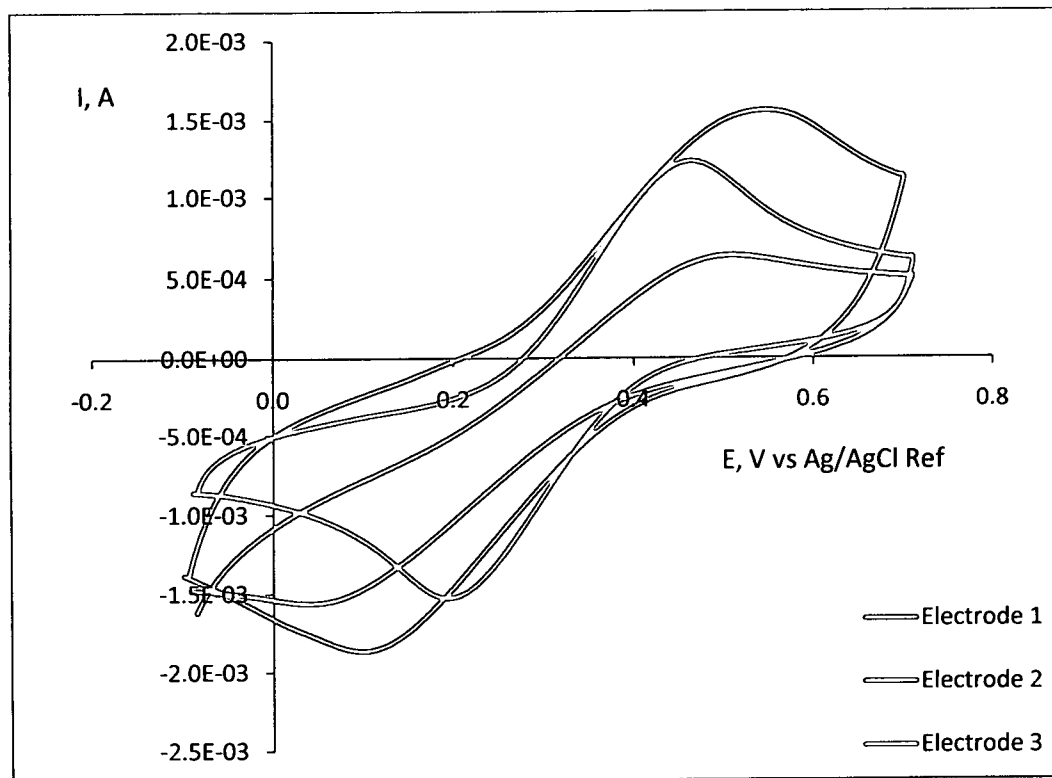


Figure A.19. Cyclic Voltamograms of Multiple Open Cell Foam Electrodes in 4mM Ferricyanide at 100mV/s Scan Rate

Figure A.19 illustrates the variability of the foam electrodes due to fabrication and manufacturing. The individual electrodes are shown in Figures A.20 through A.22. Two variables are dominant in the cyclic: internal resistance and surface area. Internal resistance of the electrodes varies from 65Ω for Electrode 3 to 147Ω for Electrode 1. Electrode 2 has an internal resistance of 134Ω . Variable electrode area is also responsible for differences in both peak currents as well as peak separations.

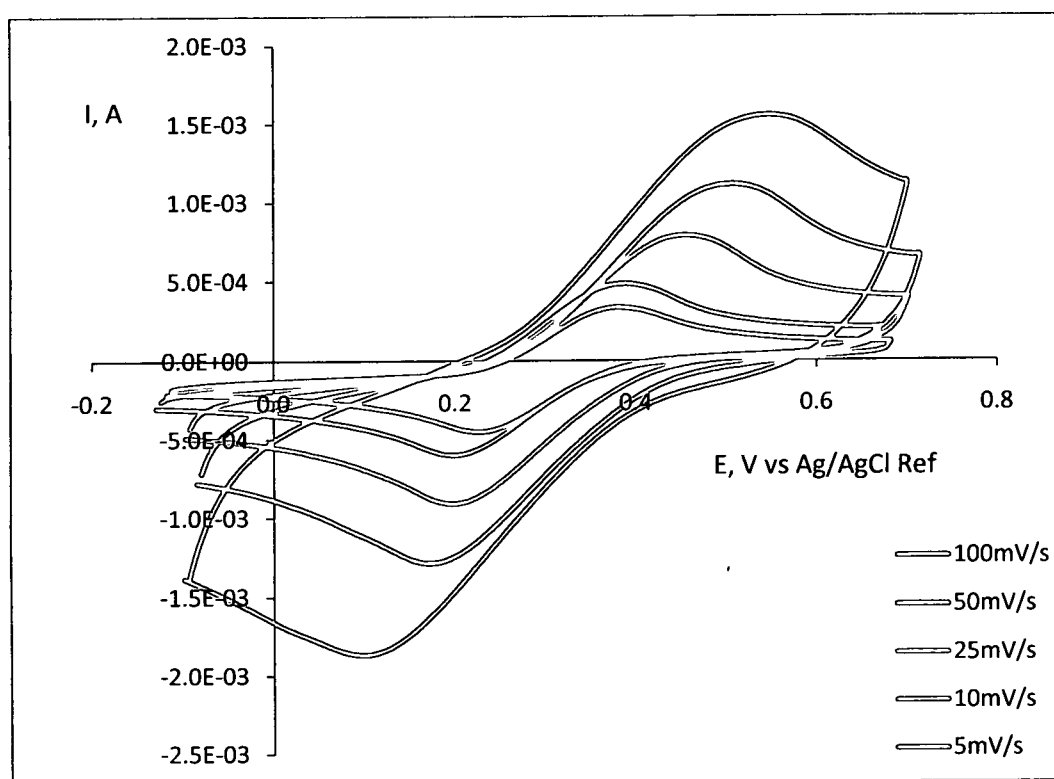


Figure A.20. Cyclic Voltammograms of Open Cell Foam Electrode in 4mM Ferricyanide/1M KNO₃ at Various Scan Rates

Figure A.20 shows the CV response of an open cell foam electrode in 4mM Ferricyanide and 1M KNO₃. The electrode was fabricated identically as the one used in Figure 3.15, but using SCNR coated foam produced on 01/13/09.

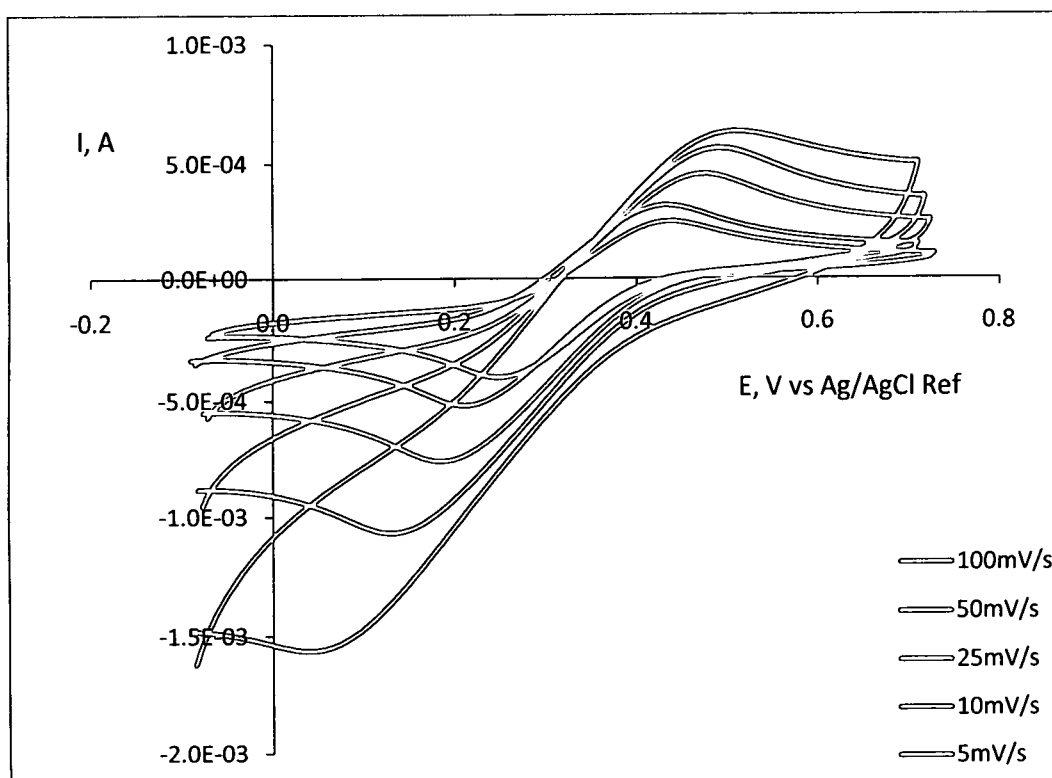


Figure A.21. Cyclic Voltammograms of Open Cell Foam Electrode in 4mM Ferricyanide/1M KNO_3 at Various Scan Rates

Figure A.21 shows cyclic voltammograms of an open cell foam electrode in 4mM ferricyanide/1M KNO_3 at various scan rates. The electrode used in Figure A.21 is identical to that used in Figure A.20 except for being produced on 07/03/06.

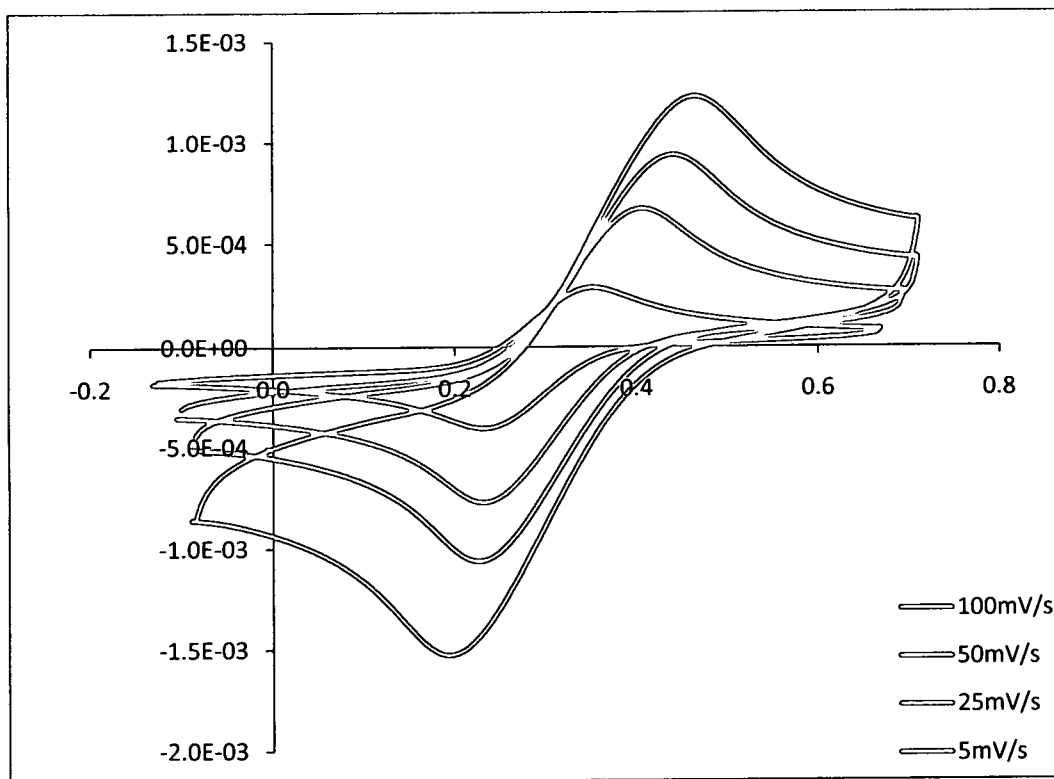


Figure A.22. Cyclic Voltammograms of Open Cell Foam Electrode in 4mM Ferricyanide/1M KNO₃ at Various Scan Rates

Figure A.22 shows cyclic voltammograms of an open cell foam electrode in 4mM ferricyanide/1M KNO₃ at various scan rates. The electrode used in Figure A.22 is identical to that used in Figure A.20 except for being produced on 04/06/08.

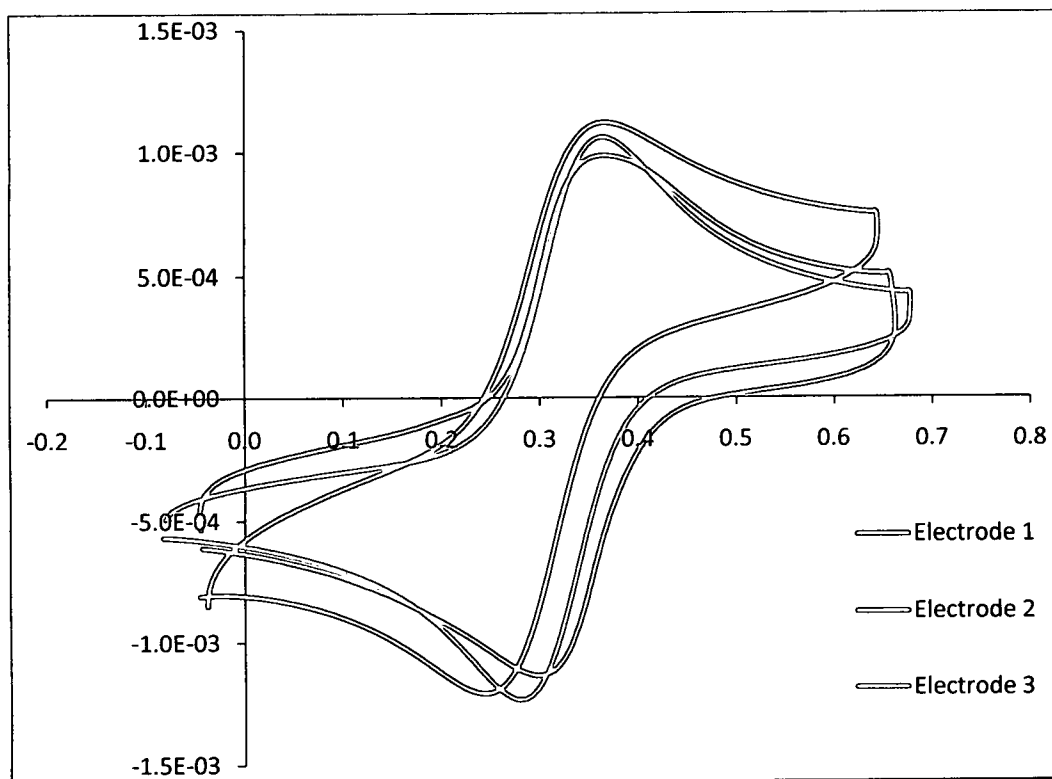


Figure A.23. IR Corrected and Normalized CVs of Open Cell Foam Electrodes in 4mM Ferricyanide and 1M KNO_3

Figure A.23 shows the 100mV/s CV of the SCNR coated foam electrodes shown in Figure A.20 through A.22, corrected for internal resistance and normalized for area.

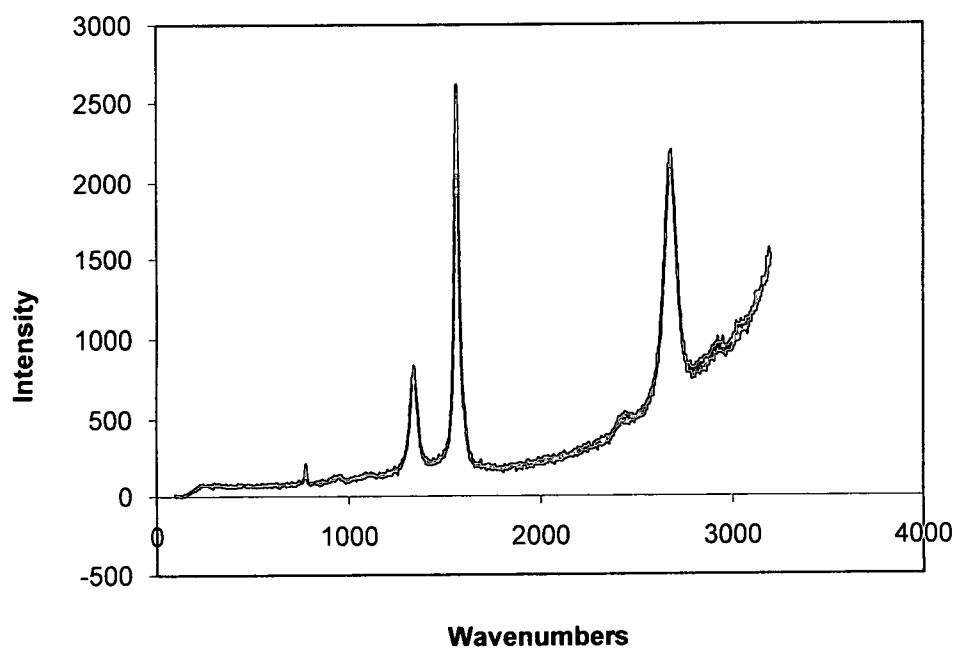


Figure A.24. Raman Spectrum of SCNRs from Aluminum Carbide Powder Using a 785nm Excitation Source

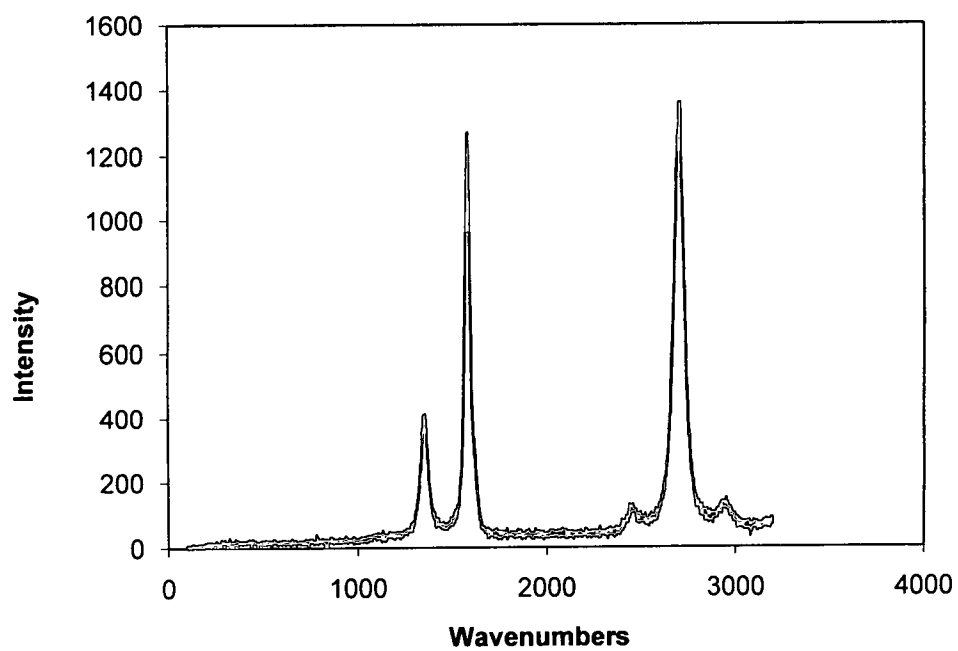


Figure A.25. Raman Spectrum of SCNRs from Boron Carbide Powder Using a 785nm Excitation Source

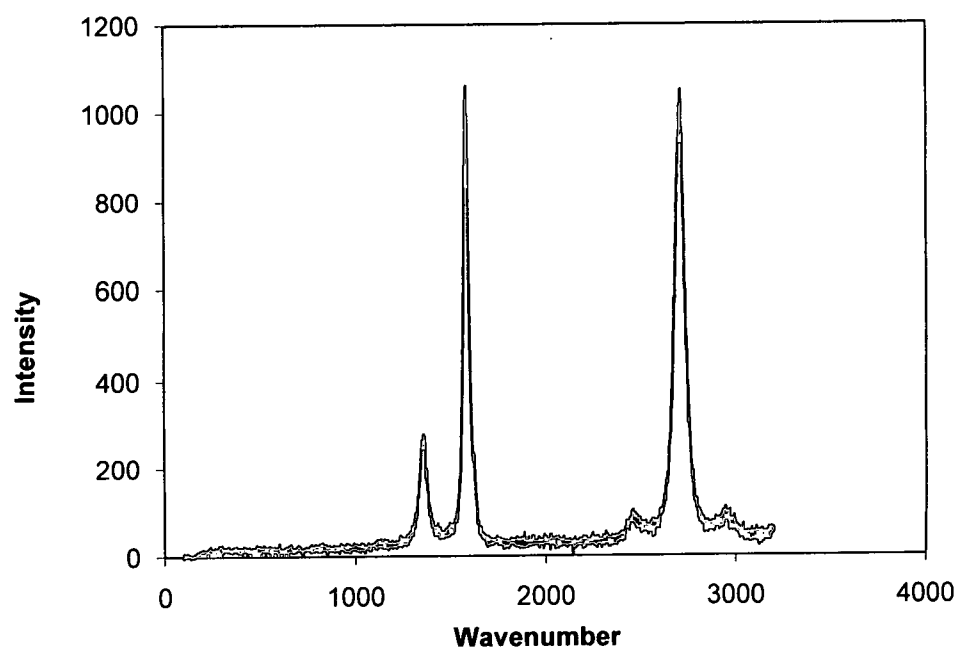


Figure A.26. Raman Spectrum of SCNRs from Zirconium Carbide Powder Using a 785nm Excitation Source

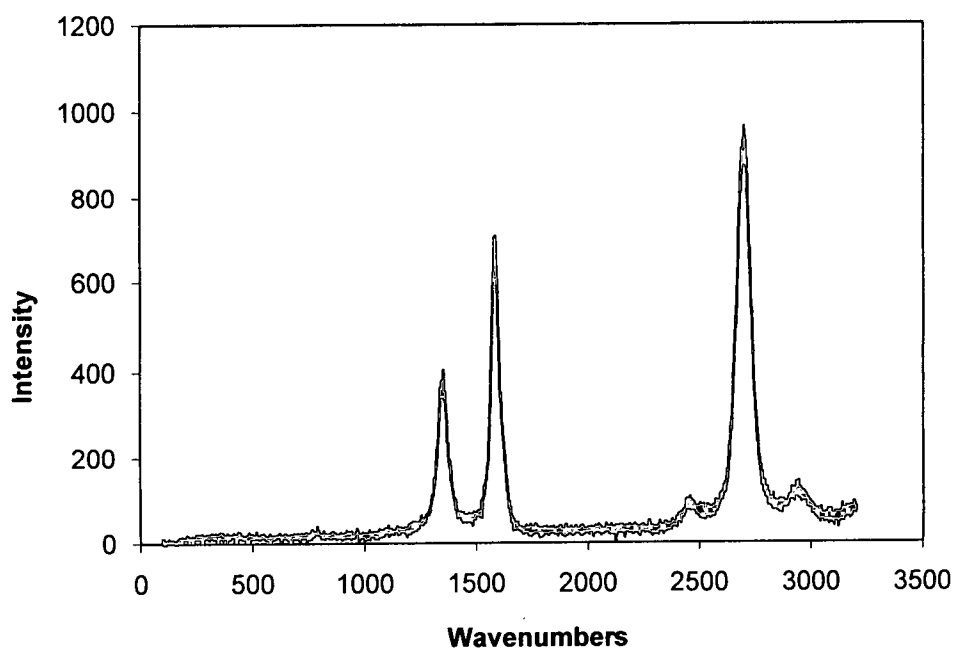


Figure A.27. Raman Spectrum of SCNRs from Titanium Carbide Using a 785nm Excitation Source

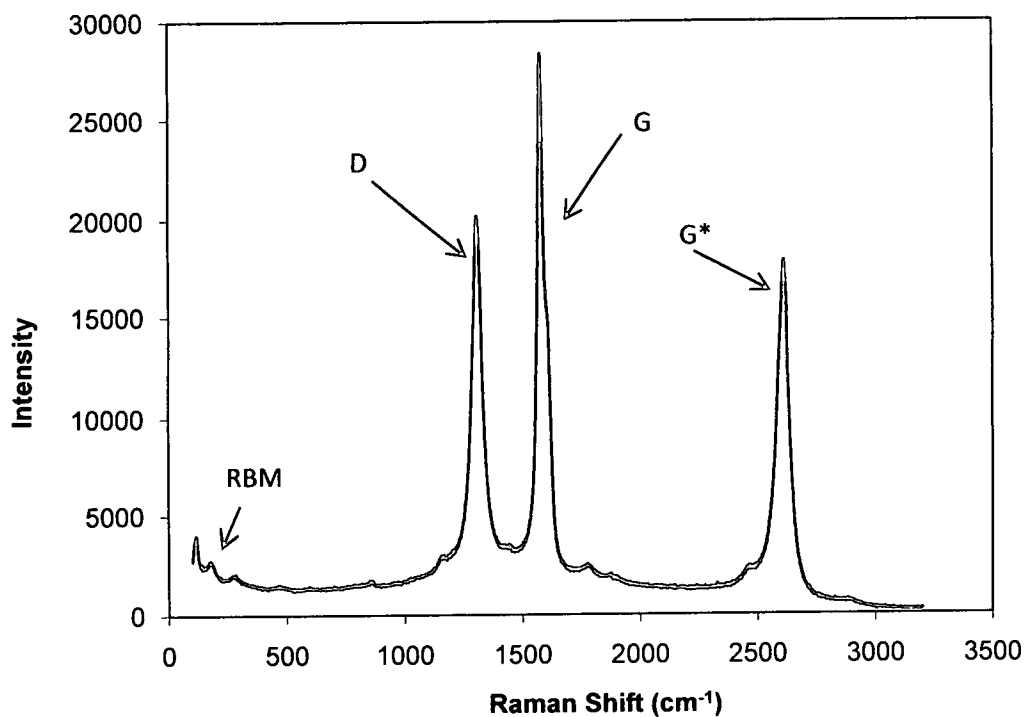


Figure A.28. Raman Spectrum of SCNR Whiskers Using a 785nm Excitation Source

Figure A.28 shows the Raman spectrum of a SCNR whisker material under good resonance. Clearly discernable are the RBM peaks below 500cm⁻¹. The characteristically high D:G ratio of SCNRs is present, as well as the splitting of the G band into G⁺/G⁻ peaks. Figure A.28 is representative of Raman spectrum of SCNRs with good resonance conditions.

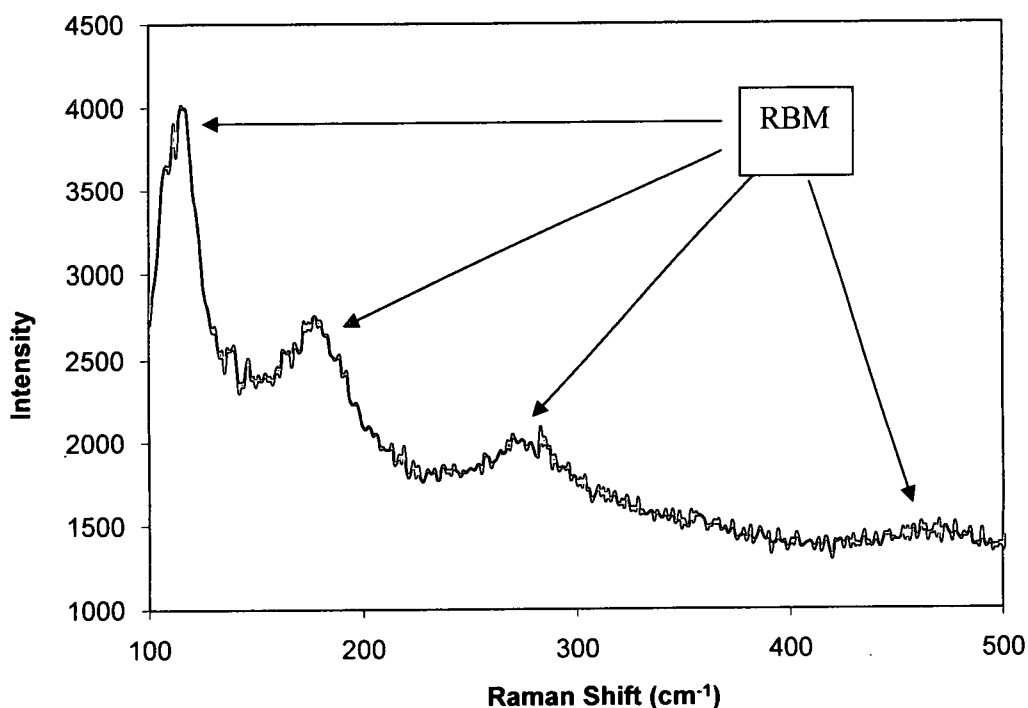


Figure A.29. RBM Spectrum of SCNR Whisker Material Using a 785nm Excitation Source

Figure A.29 shows the RBM peaks from the whisker material shown in Figure A.28. Peaks are distinctly present at 117cm^{-1} , 180cm^{-1} , 282cm^{-1} and 470cm^{-1} . These peaks correspond to tube diameters of 2nm, 1.3nm, 0.8nm, and 0.5nm, respectively. The RBM peaks seen here give direct evidence of a cylindrical fullerene, and when combined with the perspective gained from the G:D ratio, imply a finite length cylindrical fullerene.

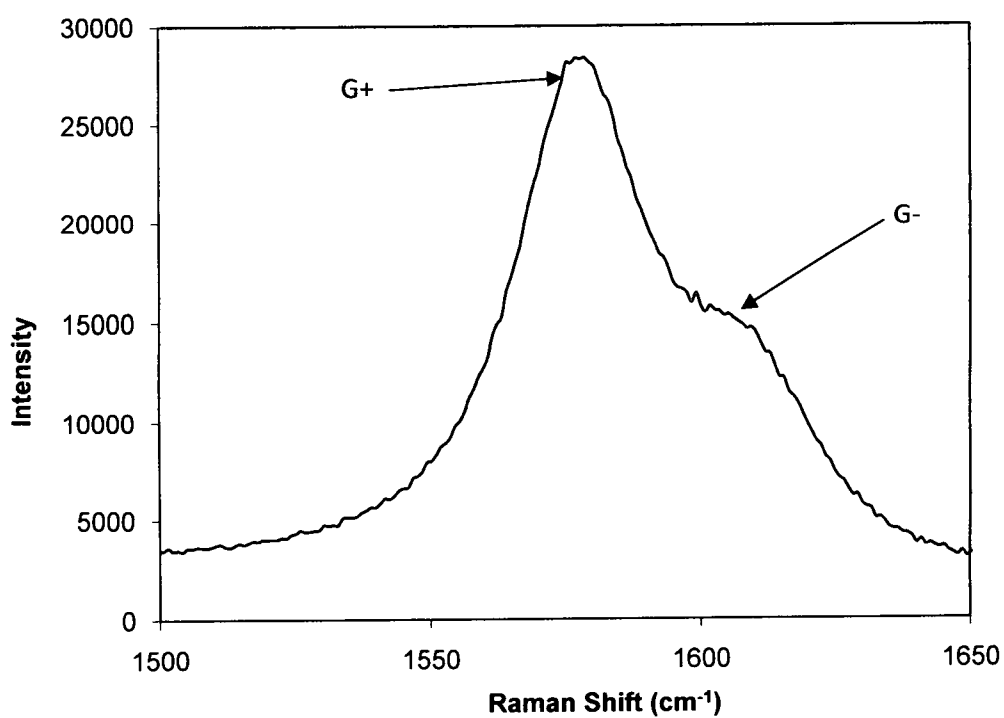


Figure A.30. Raman Spectrum of SCNR Whisker Material Showing G Band Splitting.

Figure A.30 shows the spectrum shown in Figure A.28 with the scale changed to allow better resolution of the G band splitting into the G⁺/G⁻ peaks.

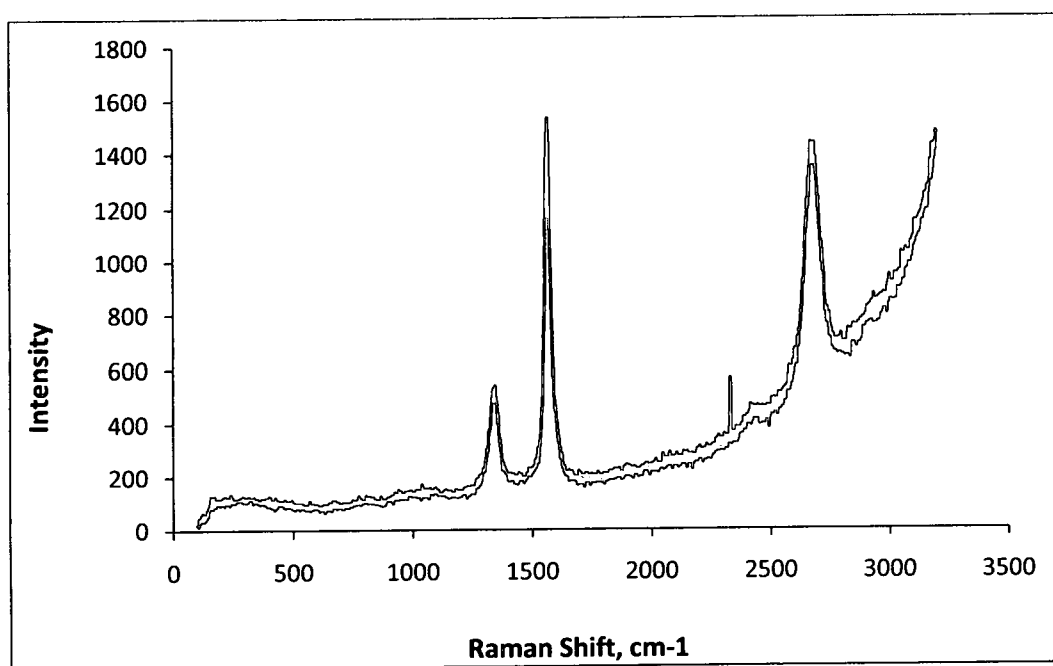


Figure A.31. Raman Spectrum of SCNR Coated Open Cell Foam Using a 514nm Excitation Source

Carbide Used	Geometry	Conversion (%Metal via ICP-MS; or height of CNT film)	Temperature (°C)	Reactive Gas(es)	Pressure (Torr)	Process Time (hrs)	Reactor Material
SiC	Nanopowder	<0.1	1400	C _x O _y /H ₂ O	0.001	2	Graphite
SiC	Nanopowder	<0.1	1500	C _x O _y /H ₂ O	0.001	2	Graphite
SiC	Nanopowder	<0.1	1600	C _x O _y /H ₂ O	0.001	2	Graphite
SiC	Nanopowder	<0.1	1700	C _x O _y /H ₂ O	0.001	2	Graphite
SiC	Nanopowder	<0.1	1800	C _x O _y /H ₂ O	0.001	2	Graphite
SiC	0.7µm abrasive powder	42.3	1400	C _x O _y /H ₂ O	0.001	2	Graphite
SiC	0.7µm abrasive powder	36.2	1500	C _x O _y /H ₂ O	0.001	2	Graphite
SiC	0.7µm abrasive powder	28.0	1600	C _x O _y /H ₂ O	0.001	2	Graphite
SiC	0.7µm abrasive powder	18.4	1700	C _x O _y /H ₂ O	0.001	2	Graphite
SiC	0.7µm abrasive powder	12.1	1800	C _x O _y /H ₂ O	0.001	2	Graphite
SiC	Nanopowder	No Conversion	1600	Argon	0.1	8	Alumina
SiC	Nanopowder	1.8	1600	CO	0.01	12	Alumina
	0.7µm abrasive powder	No Conversion	1600	45% RH Air	0.1	48	Alumina
SiC	Single Crystal Wafer	No Conversion	1600	O ₂	0.01	2	Alumina
SiC	Single Crystal Wafer	No Conversion	1600	CO ₂	0.01	24	Alumina
SiC	Single Crystal Wafer	No Conversion	1600	45% RH Air	0.00001	24	Alumina
SiC	Whisker	<0.1	1700	C _x O _y /H ₂ O	1	72	Graphite
SiC	Whisker	<0.1	1500	C _x O _y /H ₂ O	1	72	Graphite
SiC	Whisker	8.9	1400	C _x O _y /H ₂ O	1	72	Graphite
SiC	Filament	600nm	1700	C _x O _y /H ₂ O	1	24	Graphite
SiC	Filament	600nm	1700	C _x O _y /H ₂ O	.01	24	Graphite
SiC	Single Crystal Wafer	120nm	1700	C _x O _y /H ₂ O	.01	2	Graphite
SiC	Single Crystal Wafer	540nm	1700	C _x O _y /H ₂ O	.01	8	Graphite
SiC	Single Crystal Wafer	1.1µm	1700	C _x O _y /H ₂ O	.01	24	Graphite
SiC	Single Crystal Wafer	1.8µm	1700	C _x O _y /H ₂ O	.01	48	Graphite
SiC	Foam	300nm	1700	C _x O _y /H ₂ O	1.0	12	Graphite
SiC	Foam	500nm	1700	C _x O _y /H ₂ O	1.0	24	Graphite
SiC	Foam	600	1700	C _x O _y /H ₂ O	1.0	48	Graphite
B ₄ C	Powder	5.6	1700	C _x O _y /H ₂ O	1.0	48	Graphite
Fe ₃ C	Powder	7.0	1700	C _x O _y /H ₂ O	1.0	48	Graphite
TiC	2.0µm powder	7.6	1400	C _x O _y /H ₂ O	1.0	24	Graphite
TiC	2.0µm powder	6.4	1500	C _x O _y /H ₂ O	1.0	24	Graphite
TiC	2.0µm powder	6.8	1600	C _x O _y /H ₂ O	1.0	24	Graphite
TiC	2.0µm powder	2.7	1700	C _x O _y /H ₂ O	1.0	24	Graphite
Al ₄ C ₃	Powder	17.9	1700	C _x O _y /H ₂ O	1.0	24	Graphite
Cr ₃ C ₂	Powder	No Conversion	1700	C _x O _y /H ₂ O	1	48	Graphite
ZrC	Powder	9.7	1700	C _x O _y /H ₂ O	1.0	24	Graphite

Table A.1. Review of Process Variations Investigated

Bibliography

1. *New Electrodes for Old: from Carbon Nanotubes to Edge Plane Pyrolytic Graphite*. **Banks, C and Compton, R.** 2006, *The Analyst*, Vol. 131, pp. 15-21.
2. *Carbon nanotubes contain metal impurities which are responsible for the "electrocatalysis" seen at some nanotube-modified electrodes*. **Banks, C., et al.** 16, 2006, *Angewandte Chemie*, Vol. 45, pp. 2533-2537.
3. *Helical microtubules of graphitic carbon*. **Iijima, Sumio.** 1991, *Nature*, Vol. 354, pp. 56-58.
4. *Cobalt Catalysed Growth of Carbon Nanotubes with Single Atomic Layer Walls*. **Bethune, D, et al.** 1993, *Nature*, pp. 605-607.
5. **Tennant, Howard.** 4,663,230 United States of America, 1987.
6. *The Structure of Graphite Filaments*. **Hillert M, Lange N.** 1958, *Z Kristallogr*, Vol. 111, pp. 24-34.
7. *Investigation of modified basal plane pyrolytic graphite electrodes: definitive evidence for the electrocatalytic properties of the ends of carbon nanotubes*. **Banks, C., et al.** 2004, *ChemComm*, pp. 1804-1805.
8. *Chemistry of Single-Walled Carbon Nanotubes*. **Niyogi, S, et al.** 12, 2002, *Accounts of Chemical Research*, Vol. 35, pp. 1105-1113.
9. *Chemical Attachment of Organic Functional Groups*. **Chen, Y, et al.** 1988, *Journal of Materials Research*, Vol. 13, pp. 2423-2431.
10. *Diffusion Flame Synthesis of Single-Walled Carbon Nanotubes*. **Vander Wala, R, Tichib, T and Curtis, V.** 3, 2000, *Chemical Physics Letters*, Vol. 323, pp. 217-223.

11. *Graphitization Mechanism during the Carbon-Nanotube Formation Based on the In-Situ HRTEM Observation.* **Yasuda, Ayumu, et al.** 8, 2002, The Journal of Physical Chemistry B, Vol. 106, pp. 1849-1852.
12. *Large-scale Synthesis of Carbon Nanotubes.* **Ebbesen, T and Ajayan, P.** 1992, Letters to Nature, Vol. 358, pp. 220-222.
13. *Catalytic Growth of Single-Walled Nanotubes by Laser Vaporization .* **Guo, T, et al.** 1-2, 1995, Chemical Physics Letters, Vol. 243, pp. 49-54.
14. *Epitaxial Carbon Nanotube Film Self-Organized by Sublimation Decomposition.* **Kusunoki, M, Rokkaku, M and Suzuki, T.** 18, 1997, Applied Physics Letters, Vol. 71, pp. 2620-2622.
15. *X-ray studies of graphite formed by decomposing silicon carbide.* **Badami, D.** 1, 1965, Carbon, Vol. 3, pp. 55-57.
16. *Correlation Between Metal Catalyst Particle Size and Carbon Nanotube Growth.* **Kukovitsky, E, et al.** 2002, Chemical Physics Letters, Vol. 355, pp. 497-503.
17. *Ultra-small Single Walled Carbon Nanotubes and their Superconductivity Properites.* **Tang, Z, et al.** 2003, Synthetic Metals, Vol. 133, pp. 689-693.
18. **Dresselhaus, M, et al.** *Raman Spectroscopy of Carbon Nanotubes.* Physics Reports. New York : Elesvier, 2004.
19. *Growth Process of Close Packed Aligned Carbon Nanotubes on SiC.* **Kusunoki, M, et al.** 10, 2005, Applied Physics Letters, Vol. 87, p. 103105.
20. *Oxidation Behaviour of SiC Fibre Reinforced SiC.* **Kleykamp, H, Schauer, V and Skokan, A.** 1995, Journal of Nuclear Materials , Vol. 227, pp. 130-137.

21. *The Heats of Formation and Polymerization of Carbon Suboxide*. **Kybett, B, et al.** 10, 1965, The Journal of Physical Chemistry, Vol. 69, pp. 3603-3606.
22. *Kinetics of Carbon Cluster Formation in the Course of C₃O₂ Pyrolysis*. **Wagner, H, et al.** 5, 2001, Kinetics and Catalysis, Vol. 42, pp. 645-656.
23. **Cotton, et al.** *Advanced Inorganic Chemistry*. 6th. New York : Wiley Interscience, 1988.
24. **Pierson, H.** *Handbook of Chemical Vapor Deposition*. Norwich : Noyes Publishing, 1999.
25. **Wang, Z and Hui, C.** *Electron Microscopy of Nanotubes*. New York : Springer, 2003.
26. *A Carbon Nanotube Sensor Array for Sensitive Gas Discrimination Using Principal Component Analysis* . **Lu, Y, et al.** 1, 2006, Journal of Electroanalytical Chemistry, Vol. 593, pp. 105-110.
27. **Amatore, Christian.** *Electrochemistry at Ultramicroelectrodes*. [book auth.] Israel Rubinstein. *Physical Electrochemistry*. New York : Marcel Dekker, Inc, 1995, pp. 131-157.
28. *Production of Graphite Single Crystals by the Thermal Decomposition of Aluminum Carbide*. **Foster, L, Long, G and Stumpf, H.** 7, 1958, American Minerals, Vol. 23, pp. 128-136.
29. *Native Oxide Decomposition and Local Oxidation of 6H-SiC (0001) Surface by Atomic Force Microscopy* . **Xie, X. N., et al.** 24, 2004, Applied Physics Letters, Vol. 84, pp. 4914-4916.

30. *Carbon Nanotubes Grow on the C Face of SiC (000) during Sublimation Decomposition: Quantum Chemical Molecular Dynamics Simulations.* **Zhi Wang, Z, et al.** 35, 2007, Journal of Chemical Physics, Vol. 111, pp. 12960–12972.
31. *Super Washing does not Leave Single Walled Carbon Nanotubes Iron Free.* **Jurkschat, K, et al.** 2007, Analyst, Vol. 132, pp. 21-23.
32. *Carbon Nanotubes Contain Residual Metal Catalyst Nanoparticles Even After Washing with Nitric Acid at Elevated Temperature Because These Metal Nanoparticles are Sheathed by Several Graphene Sheets.* **Pumera, Martin.** 2007, Langmuir, Vol. 23, pp. 6453-6458.
33. *Raman Spectroscopy on Isolated Single Wall Carbon Nanotubes.* **Dresselhaus, M.S., et al.** 2002, Carbon, Vol. 40, pp. 2043-2061.
34. *Elimination of D-band in Raman Spectra of Double-Wall Carbon Nanotubes by Oxidation.* **Osswald, S, et al.** 4, 2005, Chemical Physics Letters, , Vol. 402, pp. 422-427.
35. *Systematic inclusion of defects in pure carbon single-wall nanotubes and their effect on the Raman D-band.* **Dillon, A.C.1, et al.** 4, 2005, Chemical Physics Letters, Vol. 401, pp. 522-528.
36. *Strength of Radial Breathing Mode in Single-walled Carbon Nanotubes.* **Machón, M, et al.** 3, 2005, Physics Review B, Vol. 71, pp. 178-183.
37. *Radial Breathing Mode of Single-walled Carbon Nanotubes: Optical Transition Energies and Chiral-index Assignment.* **Maultzsch, J, et al.** 20, 2005, Physics Review Letters B, Vol. 72.

38. *Raman Spectroscopy of Carbon Nanotubes*. **Dresselhaus, M, et al.** 2005, Vol. 409, pp. 1-53.
39. *Characteristics of the Raman spectra of Single-walled Carbon Nanotube Bundles Under Electrochemical Potential Control*. **Takeda, N and Murakoshi, K.** 1, 2007, Vol. 388, pp. 103-108.
40. *Radius and chirality dependence of the radial breathing mode and the G-band phonon modes of single-walled carbon nanotubes*. **Popov, V and Lambin, P.** 8, 2006, Physical Review B, Vol. 73, pp. 269-278.
41. *Who should be given the credit for the discovery of carbon nanotubes?* **Monthieux, Marc and Kuznetsov, Vladimir L.** 2006, Carbon, Vol. 44, pp. 1621-1625.
42. *Use of High Purity Metal-Catalyst Free Multiwalled Carbon Nanotubes To Avoid Potential Experimental Misinterpretations*. **Jones, C, et al.** 18, 2007, Langmuir, Vol. 23, pp. 9501-9504.
43. **Fiedler, D and Scholz, F.** Electrochemical Studies of Solid Compounds and Materials. [book auth.] F Scholz. *Electroanalytical Methods*. Oxford : Springer, 2005.
44. *Iron Oxide Particles are the Active Sites for Hydrogen Peroxide Sensing at Multiwalled Carbon Nanotube Modified Electrodes*. **Sljukic, B, Banks, C and Compton, R.** 7, 2006, Nano Letters, Vol. 6, pp. 1556-1558.
45. *Nanotube Electronics: A flexible approach to mobility*. **Hong, S and Myung, S.** 2007, Nature Technology, Vol. 2, pp. 207-208.

46. *Electrical Conductivity of Individual Carbon Nanotubes*. **Ebbesen, T, et al.** 1996, *Nature*, Vol. 382, pp. 54-56.
47. *Edge Plane Pyrolytic Graphite Electrodes for Stripping Voltammetry: a Comparision with Other Carbon Based Electrodes*. **Wantz, F, Banks, C and Compton, R.** 8, s.l. : Wiley-VCH, 2005, *Electroanalysis*, Vol. 17, pp. 655-661.
48. *Electrocatalytic Properties and Sensor Applications of Fullerenes and Carbon Nanotubes*. **Sherigara, B, Kutner, W and D'Souza, F.** 2003, *Electroanalysis*, Vol. 15, pp. 753-772.
49. *Fast Electron Transfer Kinetics on Multiwalled Carbon Nanotube Microbundle Electrodes*. **Nugent, J, Santhanam, R and Ajayan, P.** 2, 2001, *Nano Letters*, Vol. 1, pp. 87-91.
50. *Hydrogen Storage in Sonicated Carbon Materials*. **Hirschel, M., et al.** 2001, *Journal of Applied Physics*, Vol. 72, pp. 129-132.
51. *Detection of Homocysteine at Carbon Nanotube Paste Electrodes*. **Lawrence, N, Deo, R and Wang, J.** 2004, *Talanta*, Vol. 63, pp. 443-449.
52. *Purification Process for Single-Wall Carbon Nanotubes*. **Stronga, K, et al.** 2003, *Carbon*, Vol. 41, pp. 1477-1488.
53. *Single walled carbon nanotubes contain residual iron oxide impurities which can dominate their electrochemical activity*. **Kruusmaa, J, et al.** 9, 2007, *Electrochemistry Communications*, Vol. 9, pp. 2330-2333.
54. *Abrasive Immobilization of Carbon Nanotubes on a Basal Plane Pyrolytic Graphite Electrode: Application to the Detection of Epinephrine*. **Salimi, A, Banks, C and Compton, R.** 2004, *Analyst*, Vol. 129, pp. 225-228.

55. *Electrode, Electrochemical Biosensing Platform Using Carbon Nanotube Activated Glassy Carbon*. **Zhang, R, Wang, X and Chen, C**. 15, 2007, *Electroanalysis*, Vol. 19, pp. 1623-1627.
56. *Basal Plane Pyrolytic Graphite Modified Electrodes: Comparison of Carbon Nanotubes and Graphite Powder as Electrocatalysts*. **Moore, R, Banks, C and Compton, R**. 10, 2004, *Analytical Chemistry*, Vol. 76, pp. 2677-2682.
57. **Kinoshita, Kim**. *Carbon: Electrochemical and Physicochemical Properties*. New York : Wiley, 1988.
58. **Heineman, W and Kissinger, P**. Large-Amplitude Controlled-Potential Techniques. [book auth.] P Kissinger and W Heineman. *Laboratory Techniques in Electroanalytical Chemistry*. 2nd Edition. New York : Marcel Dekker, 1996, pp. 61-69.
59. *Investigation of Electrochemical Behavior of Hydrazine with Alizarin as a Mediator on Glassy Carbon Electrode*. **Ardakani, M, Al Karimi, M and Zare, M**. 2008, *International Journal of Electrochemical Science*, Vol. 3, pp. 246-258.
60. **Compton, Richard and Banks, Craig**. *Understanding Voltammetry*. New York : World Scientific Publishing, 2007.
61. **Sholtz, Fritz**. *Electroanalytical Methods*. New York : Springer, 2002.
62. **Adams, Ralph**. *Electrochemistry at Solid Electrodes*. New York : Marcel Dekker, 1969.
63. **Inzelt, G**. Chronocoulometry. [book auth.] F Sholtz. *Electroanalytical Methods*. London : Springer, 2005, 11.4, pp. 137-148.

64. *Raman spectra of MWCNTs and MWCNT-based H₂-adsorbing system*. **Zang, H., et al.** 13, 2002, Carbon, Vol. 40, pp. 2429-2436.
65. *Temperature Dependence of Iron-Catalyzed Continued Single Walled Carbon Nanotube Growth Rates: Density Functional Tight Binding Molecular Dynamics Simulations*. **Yasuhito, O, et al.** 1, 2009, Journal of Physical Chemistry C, Vol. 113, pp. 159-169.
66. *Double Resonant Raman Scattering in Graphite*. **Thomsen, C and Reich, S.** 24, 2000, Physical Review Letters, Vol. 85, pp. 5214-5217.

R702035700